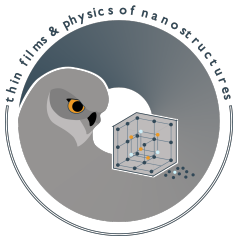

Bielefeld University
Faculty of Physics

Irradiation, intercalations and proximity: Exciting ways to tailor martensitic transformation in Ni-Co-Mn-Al magnetic shape memory Heusler compound thin films

Doctoral Dissertation in Physics
Andreas Becker

Advisor:
Prof. Dr. Andreas Hütten

2nd referee:
Prof. Dr. Christian Schröder

May 13, 2021

Universität Bielefeld
Fakultät für Physik

Hiermit erkläre ich, dass die vorliegende Dissertation von mir persönlich verfasst wurde. Einige Textpassagen und Abbildungen sind in abgewandelter Form aus von mir erstellten Publikationen übernommen. Ich habe keine anderen Quellen als die angegebenen benutzt und habe die Stellen der Arbeit, die anderen Werken entnommen sind – einschließlich verwendeter Tabellen und Abbildungen – unter Angabe der Quelle als Entlehnung kenntlich gemacht.

Bielefeld, 13. Mai 2021

(Andreas Becker)

„Physics is really nothing more than a search for ultimate simplicity, but so far all we have is a kind of elegant messiness."
—Bill Bryson

Danksagung

Bei der Erstellung dieser Doktorarbeit und während des gesamten Studiums haben mich viele Menschen unterstützt und dadurch maßgeblich zum Erfolg dieser Doktorarbeit beigetragen. An dieser Stelle möchte ich mich deshalb bei einigen dieser Personen bedanken.

Mein erster Dank gebührt meinem Betreuer Prof. Dr. Andreas Hütten, der mir die Chance gab auf dem interessanten Bereich der magnetischen Formgedächtnislegierungen zu promovieren. Ich bedanke mich sehr für die fortlaufende Unterstützung, den Zuspruch und den unerschütterlichen Optimismus, den ich selbst an einigen Stellen nicht mehr hatte. Auch die ein oder anderen Diskussionsrunden im Univarzar, Bültmannshof oder den Zugfahrten werden mir in guter Erinnerung bleiben.

Auch bedanke ich mich bei Prof. Dr. Christian Schröder, der so freundlich war als Zweitgutachter für diese Arbeit zu dienen.

Ein besonderer Dank gehört meiner Kollegin Daniela Ramermann, mit der ich viel zusammengearbeitet habe. Ohne ihr Engagement bei den TEM-Messungen wären das Schachbrett-Kapitel nicht möglich gewesen. In diesem Zusammenhang möchte ich mich auch bei Dr. Inga Ennen für weitere TEM-Untersuchungen und Beratungen danken und auch Björn Büker und Martin Gottschalk danke ich für die vielen Lamellen, die sie deswegen schneiden mussten.

Für die Bewältigung des Alltages auf D2, sowohl in organisatorischer als auch technischer Natur, danke ich Aggi Windmann und Dr. Karsten Rott. Ich möchte auch gerne meinen Betreuern Lars Helmich und Niclas Teichert während der Bachelor- und Masterarbeit danken, die mich großartig in die Geräte und Thematik eingearbeitet haben.

Für die inhaltliche und grammatikalische Korrekturen dieser Arbeit bedanke ich mich sehr bei Daniel Kappe, Lennart Schwan, Inga Ennen, Martin Gottschalk, Denis Dyck und Jan Krieft. Bei meiner Segelcrew möchte ich mich für zwei großartige Törns auf der Ostsee bedanken, die bei mir während des Schreibprozesses für nötige Ablenkung gesorgt haben.

Ich möchte auch gerne alle aktuellen und ehemaligen Kollegen auf D2 danken für die angenehme Arbeitsatmosphäre während all der Jahre. Für

die vielen lustigen und häufigen Kaffeeraumbesprechungen, sowie außeruniversitäre Aktivitäten danke ich besonders Denis Dyck, Katharina Fritz, Mareike Dunz, Phillip Zilske, Luca Marnitz, Tristan Matalla-Wagner, Jan Krieft und Dominik Graulich. Auch meinen ehemaligen Bürokollegen Daniel Kappe, Thomas Rempel, Fabian Schmidt-Michels und Martin Gottschalk bin ich besonderem Dank verpflichtet für die vielen Ratschläge und die super Zeit die ich mit euch im Labor und außerhalb der Uni verbringen durfte. Torsten Hübner, Oliver Reimer und Robin Klett danke ich auch für die tollen Momente und eine super Kanadareise.

Auch bei meinen Kooperationspartnern Dr. Tino Gottschall, Dr. Rantej Bali und Dr. Rene Hübner möchte ich mich bedanken deren Messungen mir das Bestrahlungskaptiel ermöglicht haben. Des Weiteren danke ich Dr. Biswanath Dutta für die tollen Ratschläge während der Konferenzen und Projektmeetings.

Zuletzt möchte ich mich auch ganz herzlich bei meiner Familie, meinen Eltern Reinhard und Anita, meinem Bruder Thomas Becker, sowie meinen Großeltern Inge Becker, Richard und Emmi Fassunge bedanken, die mich fortlaufend in allen Belangen immer unterstützt haben während all der Jahre. Ohne sie wäre diese Studienzeit und auch der reibungslose Umzug nach Bielefeld nicht möglich gewesen.

Dem Forschungsschwerpunkt der DFG SPP 1599 *Ferroic Cooling* danke ich für die Finanzierung meiner Arbeit.

Contents

Introduction 1

Functional materials are essential in modern technology. One class of such materials are the shape memory alloys (SMA's), which are increasingly finding their way into areas of applications. The most intriguing part of them is their ability to recover their initial shape after large deformations upon heating, hence the name shape memory. As a consequence their properties such as electrical and thermal conductivity are strongly dependent on the temperature and mechanical stress. This adds a number of functional abilities to them and are therefore also referred to as *smart materials*. One of the earliest found and most frequently employed SMA in technology is Ni-Ti, also known under its trade mark name Nitinol, which was discovered in 1963 [1]. It is biocompatible and thus has found its way into minimal invasive surgery as stents [2] but is also incorporated in braces to apply constant pressure on teeth [3]. In mechanical systems they are used as reliable actuators with little moving parts in very harsh environments such as turbojet engines of modern aircrafts [4] and even proved to be critical in aerospace for the wheels of the mars rover [5].

The SMA's owe their properties to a temperature induced phase transition between two crystal structures known as martensitic transformation (MT). The crystal structures in the MT are divided into a high-temperature phase called austenite and a low-temperature phase called martensite. Remarkably, the transition between these two structures is completely reversible. The two phases are named after their discoverers William Chandler Roberts-Austen and Adolf Martens, who investigated them in carbon steel alloys. In fact, they play a major role in the ductility and hardness of steels.

A major breakthrough was the discovery of the shape memory effect (SME) in stoichiometric ferromagnetic Ni_2MnGa by Ullakko et al. in 1996 [6]. In this material a considerable difference in the magnetization between the austenite and martensite is found. Thus MT cannot only be triggered by temperature, mechanical strain or hydrostatic pressure but also by external magnetic fields, which is therefore known as the magnetic shape memory effect (MSME) [7]. This offers new advantages such as a much higher cycling frequency of the MT compared to conventional SMA's, whose cycling frequencies are limited by thermal transport [8, 9]. Furthermore, in Ni_2MnGa

Table 1.1: Typical maximal actuation strain ranges measured in piezoelectric materials, magnetostrictive materials, conventional SMA's and Ni_2MnGa single crystals.

Material	Actuation strain [%]
Piezoelectricitiy [9]	0.07 - 0.15
Magnetostriction [9]	0.06 - 0.1
Shape memory alloys [9]	1.5 - 7
Ni_2MnGa [10, 11]	10

crystals reversible magnetic induced strains up to 10 % were achieved [10, 11], which is several times higher than for other common materials used for actuation purposes. Typical ranges for maximum strain values in piezoelectric materials, magnetostrictive materials and conventional SMA's are listed in Table 1.1.

Ni_2MnGa belongs to a special material class of intermetallic compounds, which are called Heusler compounds [12]. Since its discovery more Ni_2MnX (X = Al, In, Sb, Sn) Heusler compounds were found to exhibit the MSME [13–16]. However, unlike Ni_2MnGa these materials only become magnetic shape memory alloys (MSMA's) if some of the atomic species X is substituted by excess Mn atoms. They all have in common that the austenite phase has a considerable larger magnetization than the martensite phase. Thus, the reverse MT is triggered by an external magnetic field. But also material combinations outside the Heusler class were found with a strong magnetoelastic coupling, such as Fe-Rh, La-Fe-Si-H, Mn-Fe, Mn-As or Gd-Si-Ge [17, 18].

In the past decades several efforts have been made to incorporate MSMA's into technologies. Prototypes for microfluidic pumps [19], actuators [20], energy harvesting [21, 22] and artificial multiferroics [23] have been demonstrated. In particular, endeavors have been made to incorporate them into magnetocaloric refrigeration technology in order to substitute the expensive rare-earth benchmark material Gd [17, 18]. By cycling through the MT very large quantities of latent heat is stored and released in MSMA's, which is essential for the construction of heat pumps. The demand for efficient refrigeration technology is constantly rising. Thus, this field is a major driving force for research into MSMA's as magnetocaloric solid-state refrigeration technology can outperform conventional gas-compressed refrigeration in terms of sustainability and efficiency [17].

Despite all the efforts been made, final products available to customers are still rare until now. Many challenges still remain in these materials such

as their brittleness [24] and a large thermal hysteresis [25] accompanying the lattice transformation. The latter is the limiting factor for actuators and energy efficiency in magnetocaloric cooling systems to be realized with MSMA's. Therefore, the thermal hysteresis needs to be as small as possible. One obvious approach to overcome this issue is developing new material systems. However, this can prove to be very tedious and time consuming. If a material combination with desired properties or effect amplitudes for a specific application was already found, concepts, which do not change the chemical composition, for further tailoring the MT can be of the same value as well. Such methods could involve changing the parameters of material synthesis, post-processing or exploiting interactions with other materials. Throughout this thesis one example of each of the three classes is investigated and discussed if they are able to improve the thermal hysteresis or the response to external magnetic fields of the MT.

All of the investigated samples are thin film systems prepared by sputtering deposition. Although thin film MSMA's are not particularly useful in any application they prove to be ideal systems for research purposes. Several samples series can be fabricated much faster compared to bulk synthesis methods with a high quality, second only to single crystals. Furthermore, many concepts which rely on precise microstructural control can be readily tested on thin film systems, while suitable processing methods for bulk samples have yet to be developed. As a material of choice the Ni-Mn-Al Heusler compound system is chosen. This material was shown to be quite promising for magnetocaloric applications [16]. Still, large thermal hysteresis curves are often measured for this system. Much characterization for it has also been carried out in our group prior to this work.

After this introduction the reader is first introduced to the most important theoretical aspects of the martensitic transformation in chapter 2. This includes the definitions of the terminology and the thermodynamics of the MT. Special emphasis in this chapter is given to the description of the martensitic microstructures, their orientation relative to the austenite cells and the nucleation and growth of the martensite nuclei. The chapter concludes with an introduction to Ni-Mn-based MSMA Heusler compounds. In chapter 3 the most important aspects in sputtering deposition and x-ray diffraction are explained to the reader for both are essential in preparation and analysis of all samples in this thesis. Descriptions of other investigation methods are not further mentioned for the sake of brevity as for all of them literature is readily available.

In the first experimental section in chapter 4 a proof-of-principle study for enhancing the magnetization in the austenite state by exploiting the interaction of the MSMA with a ferromagnetic thin layer in close proximity is presented. The investigations are mainly carried out by x-ray magnetic circu-

lar dichroism (XMCD) and x-ray resonant magnetic reflectivity (XRMR). Since both techniques may not be known well to a large audience, an introduction to both of them is given first followed by the experimental results. As an example of post-processing methods following MSMA thin film preparation ion beam irradiation to create point like defects in the crystal structure is studied in chapter 5. The effects of including martensite nuclei in the shape of intercalation layers during the fabrication process is presented in chapter 6. As the number of intercalation layers increases, the integrity of the system is lost to form a 3D chessboard-like microstructure. This unique microstructure can be beautifully imaged in high-resolution transmission electron microscopy. Because this structure is rather complex the entire chapter 7 is devoted to it. Finally, the experimental findings are briefly summarized and an outlook on the preparation of MSMA nanoparticles is presented in the last two chapters 8 and 9, respectively.

Fundamentals about the martensitic transformation 2

In this chapter the fundamental theoretical aspects of MSMA's are presented. The main focus is hereby on the MT and the origin of its thermal hysteresis. In the last subsection a brief overview of the NiMn-based Heusler alloys, which are investigated in this thesis, is presented.

2.1 The martensitic transformation

The origin of the shape memory effect is the MT, which was first discovered in Cu-Zn and Cu-Al alloys. If a shape memory alloy is cooled down from a high temperature state it changes its crystal structure in a first-order, diffusionless, solid-to-solid phase transition. The high temperature phase is called austenite in these alloys and the low temperature state martensite. Martensite unit cells have at least the same or a lower symmetry than the austenite unit cells. The temperature, at which the phase transformation starts, is the martensite start temperature M_s and the one at which it ends is the martensite finish temperature M_f. This phase transformation is completely reversible upon heating material. The reverse transformation is correspondingly characterized by the austenite start and finish temperatures A_s and A_f. MT and reverse transformation usually do not occur at the same temperature, thus a thermal hysteresis is observed for the full cycle, which tends to broaden if the sample size is reduced [26]. An illustration of the austenite fraction in dependence of the temperature, along with the transformation temperatures is given in Figure 2.1.

Determination of M_s, M_f, A_s and A_f is achieved by fitting the data below the transformation, above the transformation and the slope of the transformation with linear functions. The temperatures of the points of intersection are defined as the aforementioned variables. Another way of describing the MT is by the martensitic transformation temperature T_M and austenitic transformation temperature T_A, which are defined as the turning points of the cooling and heating branch respectively. The hysteresis width

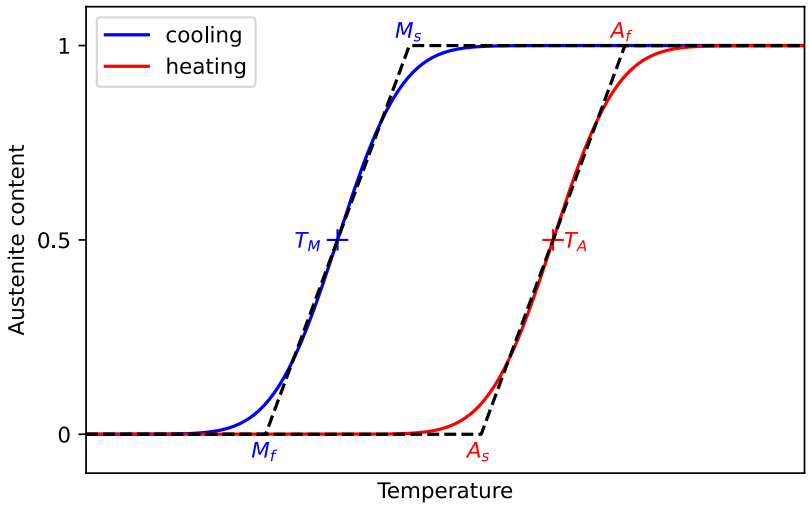

Figure 2.1: Illustration of the martensitic and reverse transformation. Marked are the transformation temperatures used in this thesis.

ΔT in this work is defined by the difference of those two temperatures:

$$\Delta T = T_A - T_M. \tag{2.1}$$

In MSMA's the magnetic properties are strongly linked to the crystal structure. Thus, in these alloys it is possible to drive the martensitic or reverse transformation not only by temperature, hydrostatic pressure or mechanical strain but also by an external magnetic field.

2.2 Thermodynamics of the martensitic transformation

The driving force for the MT is the difference in the Gibbs free energy ΔG between the martensite G_M and austenite state G_A,

$$\Delta G = G_A - G_M. \tag{2.2}$$

The Gibbs free energy in a MSMA is defined as:

$$G = U + pV - TS - \mu_0 HM - \sigma\epsilon V, \tag{2.3}$$

with U the inner energy, p the pressure, V the volume, T the temperature, S the entropy, μ_0 the magnetic susceptibility, H the magnetic field, M the

magnetization, σ the mechanical stress and ϵ the applied mechanical strain. An illustration of the temperature dependence of G_A and G_M is shown in Figure 2.2. At higher temperatures the G_A becomes smaller than G_M thus this phase is stable at higher temperatures. From a pure thermodynamic view the transformation should be happening at the temperature corresponding to the point of intersection T_{MT} of the two Gibbs free energies. At this point both Gibbs free energies are equal

$$G_M(H, T_{MT}(H)) = G_A(H, T_{MT}(H)) \tag{2.4}$$

A solution to this equation is given by the Clausius-Clapeyron relation [27]:

$$\frac{\partial T_{MT}(H)}{\partial H} = -\mu_0 \frac{M_A(H, T_{MT}) - M_M(H, T_{MT})}{S_A(H, T_{MT}) - S_M(H, T_{MT})}. \tag{2.5}$$

Thus, the martensitic transformation temperature can be shifted by an external magnetic field. It follows from this equation that the martensitic or reverse transformation can be induced by an external magnetic field if there is a difference in magnetization between the austenite and martensite phase. The Zeeman energy will prefer the phase with higher magnetization.

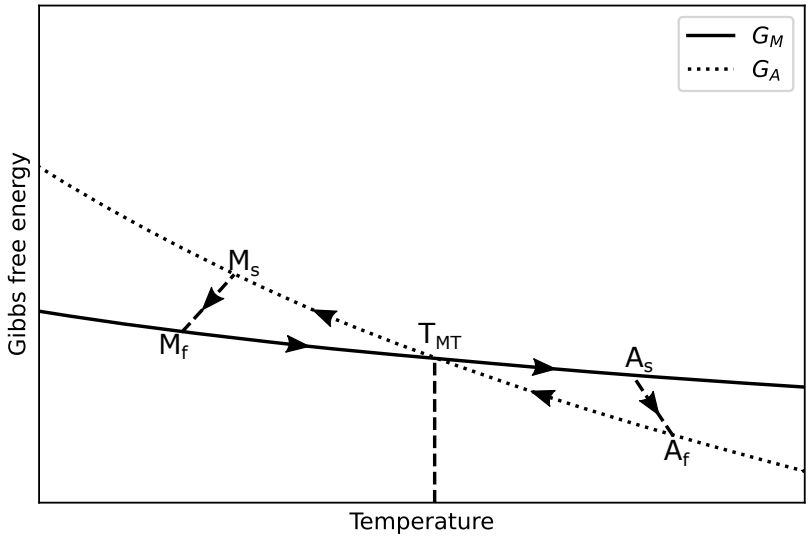

Figure 2.2: Illustration of the Gibbs free energy of the martensite (solid line) and austenite (dotted line) in dependence of temperature. Marked are the transformation temperatures.

2.3 Martensite microstructure

A general model for the martensitic transformation can be derived using infinitesimal strain theory [28]. The transformation between the martensite unit cell and austenite unit cell is described by a transformation matrix $\boldsymbol{U}$, which is also called Bain matrix. There are many MT types, which are classified by their crystal distortion, e.g. cubic-to-tetragonal, cubic-to-orthorhombic, cubic-to-monoclinic or tetragonal-to-orthorhombic [29–32]. Only the cubic-to-tetragonal transformation will be covered in this work, which is shown in Figure 2.3. In this process one of the cubic axes with lattice constant a_0 is stretched, while the other two are compressed to get a tetragonal cell with lengths a and c. There are three different orientations of the c-axis possible relative to the cubic austenite cell, which are all energetically equivalent. The different orientations are called martensite variants. The corresponding transformation matrices for the three variants are:

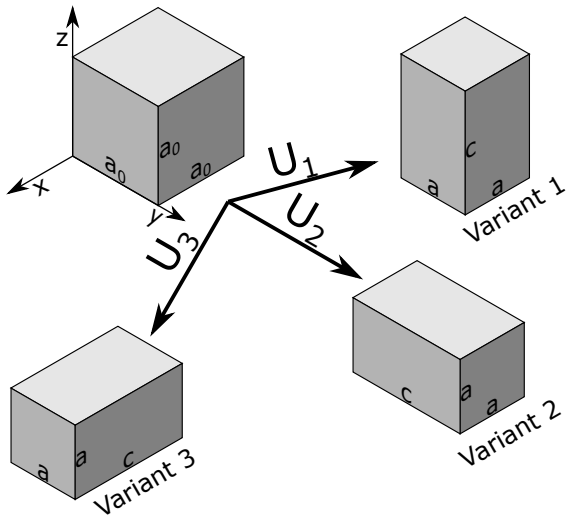

Figure 2.3: Illustration of the three different martensitic variants in a cubic-to-tetragonal transformation.

$$U_1 = \begin{pmatrix} \alpha & 0 & 0 \\ 0 & \alpha & 0 \\ 0 & 0 & \beta \end{pmatrix} \; U_2 = \begin{pmatrix} \alpha & 0 & 0 \\ 0 & \beta & 0 \\ 0 & 0 & \alpha \end{pmatrix} \; U_3 = \begin{pmatrix} \beta & 0 & 0 \\ 0 & \alpha & 0 \\ 0 & 0 & \alpha \end{pmatrix}, \tag{2.6}$$

with $\alpha = a/a_0$ and $\beta = c/a_0$.

The number of martensite variants N_V can be calculated for any martensitic transformation from the properties of the point groups from the austenite $\mathcal{P}_A$ and martensite $\mathcal{P}_M$ by [32]:

$$N_V = \frac{\text{the number of rotations in } \mathcal{P}_A}{\text{the number of rotations in } \mathcal{P}_M}. \tag{2.7}$$

It is evident that a single austenite unit cell cannot transform into the martensite phase within the austenite matrix. This would lead to a large amount of elastic energy stored in the boundaries, due to their different crystal lattices. Thus, instead a very complicated and metastable martensite structure, consisting of fine twins, can often be observed upon cooling.

A configuration with minimal energy is obtained when the martensite variants and austenite cells arrange themselves such that coherent interfaces are obtained. This ensures that only minimal elastic energy is stored in the phase boundaries. The situation can be described in the infinitesimal strain theory and is accomplished when the kinematic compatibility condition:

$$\boldsymbol{F} - \boldsymbol{G} = \vec{a} \otimes \hat{n} \tag{2.8}$$

is fulfilled. $\boldsymbol{F}$ and $\boldsymbol{G}$ are the deformation matrices for the two regions, $\hat{n}$ is the normal vector of the boundary plane and $\vec{a}$ some vector. Boundaries, which fulfill this equation, are called invariant planes, as it can be shown that any vector lying in the plane is transformed equally by $\boldsymbol{F}$ and $\boldsymbol{G}$. Thus, atoms lying in this plane are not distorted, minimizing the amount of elastic energy needed to form an interface.

Two types of different interfaces can arise in materials with a martensitic transformation. Both of them lead to the observed, complex martensite structure. The first type of boundaries are the interfaces between different martensite variants. Considering the martensite variants I and J, which are transformed by the their respective transformation matrices $\boldsymbol{U_I}$ and $\boldsymbol{U_J}$, it is always possible to form a coherent interface if one of the transformations is additionally rotated by a rotation matrix $\boldsymbol{Q}$. Thus, equation 2.8 becomes:

$$\boldsymbol{U_I} - \boldsymbol{Q} \cdot \boldsymbol{U_J} = \vec{a} \otimes \hat{n}. \tag{2.9}$$

The situation is illustrated for the 2D case in Figure 2.4. Because both phases are energetically equivalent, this process is known as twinning. The planes $\hat{n}$ that separate the martensite variants are therefore accordingly named twin boundaries.

The second type of boundary conditions occurs at the interface between the martensite and austenite phases. The behavior at the interface is governed by the geometric compatibility between the two different unit cells.

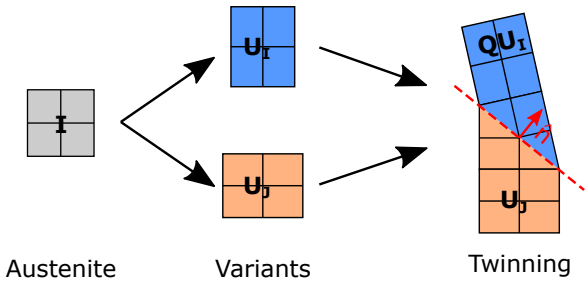

Figure 2.4: Illustration of the twinning mechanism in 2D. The red dashed line represents the twin boundary.

It can be shown that a perfect match between a single martensite variant $\boldsymbol{U_I}$ can only be achieved on the condition that the eigenvalue λ_2 of the Bain transformation matrix equals 1. However, this condition is generally not met for most martensite unit cells in SMA's. Despite this, low energy interfaces, which are called habit planes, are still possible by a mixture of martensite variants utilizing the twinning mechanism. The kinematic compatibility equation 2.8 becomes in this case:

$$\boldsymbol{Q'} \cdot [\eta \cdot \boldsymbol{U_I} + (1-\eta) \cdot \boldsymbol{Q} \cdot \boldsymbol{U_J}] - \boldsymbol{I} = \vec{a} \otimes \hat{m} \tag{2.10}$$

with η being the fraction of variant I, $\boldsymbol{Q'}$ a rotation matrix and $\hat{m}$ the normal vector of the invariant plane . The Bain matrix for the austenite is in this case the identity matrix $\boldsymbol{I}$. The matrix $\boldsymbol{Q}$ is obtained by first solving the twinning equation Equation 2.9 independently. In contrast to the twin boundaries the habit planes are not infinitely sharp but extend over a certain width. Solutions to this equation result in a periodic arrangement of fine parallel twins in martensite regions. Due to this arrangement of the martensite variants this is often referred to as adaptive martensite in the literature. Only for certain habit planes orientations a solution to Equation 2.10 exists. Ball and James [28] developed a procedure of finding a solution for a martensite nucleus in the bulk, if $\boldsymbol{Q}$, $\vec{a}$ and $\hat{n}$ are known. The procedure is followed by Bhattacharya [32] to find a formula for $\hat{m}$ in dependence of the α and β values from the Bain matrices for cubic-to-tetragonal transformations:

$$\hat{m}^{\pm} = \frac{1}{\rho} \begin{pmatrix} \pm\frac{\delta+\tau}{2} \\ \pm\frac{\delta-\tau}{2} \\ 1 \end{pmatrix}. \tag{2.11}$$

ρ is the normalization constant. δ and τ are given by:

$$\delta = \sqrt{\frac{\alpha^2 + \beta^2 - 2}{1 - \alpha^2}}, \quad \tau = \sqrt{\frac{2\alpha^2\beta^2 - \alpha^2 - \beta^2}{1 - \alpha^2}}. \tag{2.12}$$

Two more solutions are found by reversing the sign of the first component of $\hat{m}$. The final four solutions are found by interchanging the first two entries of the previously obtained vectors, bringing the total number up to eight possible habit plane orientations for a given pair of martensite variants. Since there are three different variants in a cubic to tetragonal martensitic transformation and therefore three pairs, the total number of solutions is $3 \cdot 8 = 24$. In many cases, $\hat{m}$ is slightly tilted from the {110} planes of the austenite reference system.

A typical situation at the habit plane involving the twinning mechanism is illustrated in Figure 2.5. According the compatibility equations (Equations 2.9 and 2.10) a close match between the austenite (red cells) and martensite (blue unit cells) at the habit plane can be achieved by a fine mixture of two variants joined by parallel twin boundaries. Exemplary shown is here the 14M ('M' stands here for monoclinic) modulation for the martensite, which is often observed in NiMn-based MSMA Heusler compounds. To describe the adaptive martensite new superstructure unit cells are usually defined, shown as the lilac shaded area. The modulated structures are discussed further below in chapter 2.5.

In observations of SMA's a larger variety of complex martensite structures are observed than the simple twinning mechanism at the nanoscale suggests. Kaufmann, Niemann and Schwabe [33–35] classified the encountered structures in Ni-Mn-Ga thin films in a hierarchical model according to their length scales. The discussed twinning, as the smallest martensite structure represents therefore the first level of the hierarchy.

On closer inspection of the modulated structure a region in the shape of a triangle between the martensite and austenite is formed, as depicted in the magnification in Figure 2.5. From geometrical considerations the sides of the triangle are given by $x = \beta$ and $y = 2.5 \cdot \alpha$. The angle between them is given by $180° - \alpha_{TW}$, where α_{TW} is the twinning angle calculated by:

$$\alpha_{TW} = \arctan\left(\frac{\beta}{\alpha}\right) - \arctan\left(\frac{\alpha}{\beta}\right). \tag{2.13}$$

With $\alpha = 0.96059$ and $\beta = 1.15466$, which was measured in the checkerboard sample discussed later in Chapter 7, the length of w in the triangle is calculated by al-Kashi's law of cosines to be $w = 3.543$. If a perfect match with the austenite would be achieved w would be equal to $n \cdot 0.5$, where n is a positive integer. Thus, there is a slight difference in length between the

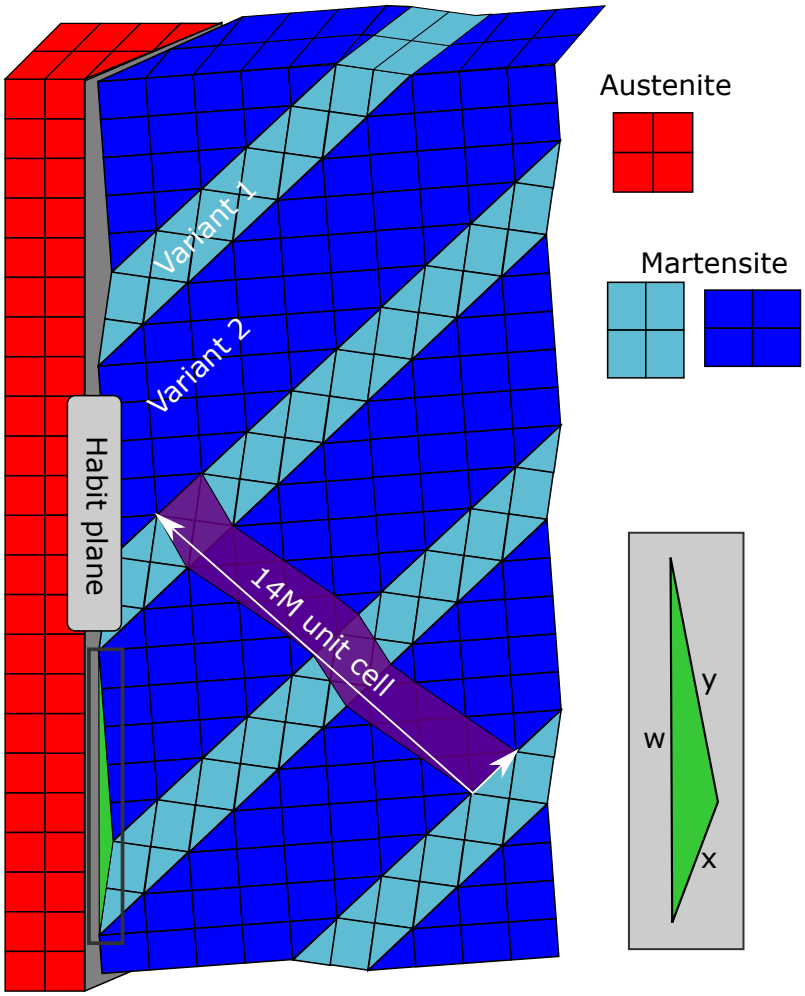

Figure 2.5: Illustration of the martensite (blue cells) austenite (red cells) interface at the habit plane. Shown here is the 14M modulation of the martensite. The bct-unit cell for this modulated structure is marked by the violet shaded area. The habit plane is not infinitely sharp but small triangular gaps are present between the austenite and martensite cells, which is marked as the green triangle (adapted and modified from [33]).

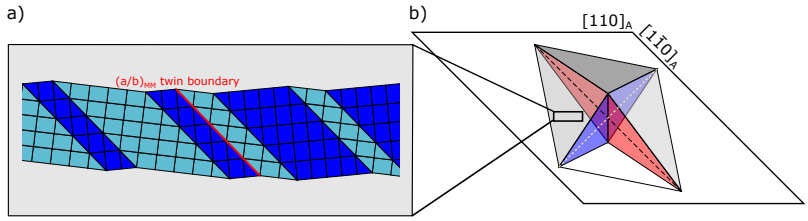

FIGURE 2.6: Illustration of a) $(a/b)_{MM}$ twin boundary, which is marked by the red line, and b) a diamond shape martensite nucleus. The mirror planes are marked in red and blue. The last mirror plane lies in the plane and is sketched as a yellow dashed line.

modulated martensite and austenite, which in turn increases the inelastic energy at the habit plane. The length difference and therefore the elastic energy is proportional to the size of the habit plane. In order to minimize the elastic energy again the martensite develops a new type of ordering by simply reversing the order of the martensite variants in the modulated structure. At sufficiently large habit planes this process allows the compensation of the mismatch between the modulated martensite and the austenite. The new required twin boundaries for this mechanism, which are called $(a/b)_{MM}$ twin boundaries, are energetically favorable, as they are parallel to the existent ones. This type of twin boundary is illustrated in Figure 2.6 a). They were only recently confirmed from the 7M structure by synchrotron x-ray diffraction measurements [33]. The type of twinning forms the second hierarchical level of the martensite structures.

The transformation into the martensite occurs via a nucleation process in the austenite matrix. The martensite volume needs to be surrounded from all sides by habit planes. Thus, they cannot be arbitrarily shaped and orientated. From the observation of nuclei of some microns size at the surface of a thin film it was determined that they take the general shape of elongated diamonds [6, 35] (Figure 2.6 b)). The three mirror planes of this shape divide it into eight subvolumes, which each consist of the twinned martensite structure of the first two levels. They are joined by one another at the mirror planes, which are itself twin boundaries.

Even larger martensite structures are obtained by a parallel arrangement of martensite nuclei. This is referred to as herringbone structure in the proposed model and evolves during the growth process of the nuclei. At last several of differently orientated herringbone structures can arrange themselves in a way to form a coherent interface, which is the largest observed martensite pattern and therefore the last level of the hierarchy. However,

since this ordering mechanisms on the macroscopic level are not important for this work they will not be discussed any further. Instead, the interested reader is referred for a detailed description of the hierarchical model to the above mentioned publications.

2.4 Nucleation and growth of martensite

The martensitic transformation can be split into two processes: a nucleation step and the growth of these nuclei, which will be addressed in this chapter. Controlling both of them is essential for obtaining a small thermal hysteresis in SMA's.

As discussed in chapter 2.2 the driving force of the martensitic transformation is the energy difference ΔG of their respective states. At T_{MT}, where both Gibbs free energies are equal, spontaneous phase transitions driven by thermal fluctuations should occur from a thermodynamic point of view. However, for first order phase transitions boundary planes between the two phases have to be established, which take the form of habit planes and twin boundaries according to microscopic martensite theory in this case. These contribute to energy difference due to their elastic energy as well. Thus, the energy difference ΔE for a martensite nuclei can be written as:

$$\Delta E = V \cdot (G_A - G_M) + \sum_n A_n \cdot w_n. \tag{2.14}$$

V is the volume of the nucleus while A_n and w_n are the area and the respective energy density of the habit planes and twin boundaries present. In order for a stable martensite nucleus to form the first term has to exceed the energy contribution from the boundaries. Two implications arise from this. First, a gain in energy by nucleation is only achieved if the volume of the nucleus is greater than a critical size. Second, the two states are separated by energy barrier ΔE, which needs to be overcome. Thus, the SMA needs to be undercooled for the MT to start. For the same reason the sample needs to be overheated for the reverse transformation. For a thermal activated nucleation process an Arrhenius-Ansatz for the transition probability $W(T)$ can be made:

$$W(T) = Be^{-\frac{\Delta E}{k_B T}}. \tag{2.15}$$

k_B is the Boltzmann factor and B a proportionality factor. Haasen et al. [37] estimated ΔE to be in the order of about 10^5 eV in Fe-based martensitic alloys for homogeneous nucleation processes. Thus, such a nucleation is accordingly to the Arrhenius equation unlikely to happen at room temperature. Instead the martensitic transformation is governed by inhomogeneous

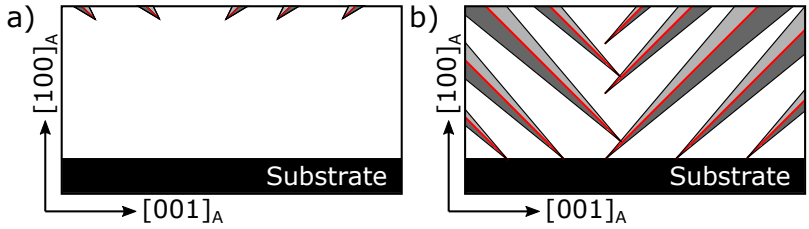

FIGURE 2.7: Illustration of the martensite nucleation at the free surface a) and growth b) in substrate constrained thin films.

nucleation processes at defects and dislocations due to a reduction of the energy barrier by their local strain fields. Often martensite nucleation is first observed at structural defects like grain boundaries, free surfaces and point defects [38]. Malygin found at dislocations [39] and precipitates [40] a local variation of the transition temperatures for the martensitic transformation.

Once martensite nuclei are established the MT proceeds further by the growth of them. This is achieved by moving their habit planes along the surface normal. Note, that during this step the habit planes are not allowed to rotate or split. Thus, energy barriers for this process are considered to be much lower compared to the nucleation of martensite [41, 42], which results in very small transition regions between M_S and M_F in the hysteresis curves. In substrate constrained thin films martensite regions nucleate first at the free surface and grow towards the substrate, mainly in length but not in width. The elongated diamonds change their shape during the growth into a parallelogram. In a slice of the $[001]_A/[100]_A$ plane they appear as needles with their tips pointing towards the substrate, as illustrated in Figure 2.7.

Their growth stops if their tips come into contact with an interface where no compatible boundary can be formed. Such conditions arise at the substrate interface or at interfaces of incompatible martensite nuclei. Therefore, often untransformed regions of austenite remain between the nuclei in a thin film sample. If the residual austenite regions are larger than the critical martensite nucleus size they can be partially transformed. However, this often requires are large undercooling and therefore adds a nonlinear behavior to the transformation and broadens the transitions region. As seen by this example, defects can have a contradictory role for the growth phase. While defects promote the nucleation, they also prove to be obstacles for the growth of martensite and additional energy is needed to overcome them. A formula for the transformation range $\Delta\tau$ in dependence of the defect

concentration C and defect radius r was derived by Malygin [43]:

$$\Delta\tau = \frac{3k_B T_e^2}{\pi q r^3} C, \tag{2.16}$$

where q is the transformation heat and T_e the temperature where the austenite and martensite fractions become equal.

2.5 NiMn-based magnetic shape memory Heusler compounds

Heusler compounds are materials, which consist of three different elements with the chemical formula X_2YZ. The X and Y elements are usually transition metals and Z belongs to the main group. Each element occupies one of four interpenetrating fcc sublattices. Because the X element is present twice, two of those sublattices are equal to each other. The total crystal structure, which is often referred to as $L2_1$, can be described as a cubic $Fm\bar{3}m$ unit cell with X occupying the 8c (1/4,1/4,1/4) sites, Y the 4a (0,0,0) and Z the 4b (1/2,1/2,1/2) sites in the Wyckoff notation. Due to the large number of possible chemical combinations the Heusler class contains more than one thousand different compounds known to this day [12].

MT's in ferromagnetic materials are found in Mn-rich N-Mn-Z compounds (Z=Al, Ga, In, Sb, Sn) [13–16]. All of these NiMn-based Heusler compounds undergo a cubic-to-tetragonal transformation. The austenite phase can be described as a chemically disordered $L2_1$ structure (also known as B2 ordering, which will be described further in chapter 3.2.1) as shown in Figure 2.8 a). Distortion of this unit cell into a tetragonal shape with lattice constants a_{NM} and c_{NM} leads to the $D0_{22}$ crystal structure used to describe the martensite phase. The subscript 'NM' stands here for the non-modulated martensite. Because the axes of this crystal structure are parallel to the $L2_1$, it allows an easy comparison between the martensite and austenite phases and is therefore used throughout this thesis if not stated otherwise. Another description as the base centered tetragonal (bct) $L1_0$ structure is often found in the literature. The relationship between the $D0_{22}$ and $L1_0$ structure is shown in Figure 2.8 b) and c). The $L1_0$ structure is rotated by 45° to the $D0_{22}$ cell thus the relationships between their lattice constants are $a_{\mathrm{NM}} = \sqrt{2}a_{\mathrm{bct}}$ and $c_{\mathrm{NM}} = c_{\mathrm{bct}}$.

In order to fully describe the symmetry of the twinned martensite larger, monoclinic (M) crystal structures from modulated $L1_0$ unit cells are constructed. Frequent observed modulated martensite structures in the NiMn-based Heusler compounds are the 10M and 14M modulations [7, 34]. Their respective projections on the (001) plane are shown in Figure 2.8 d) and e).

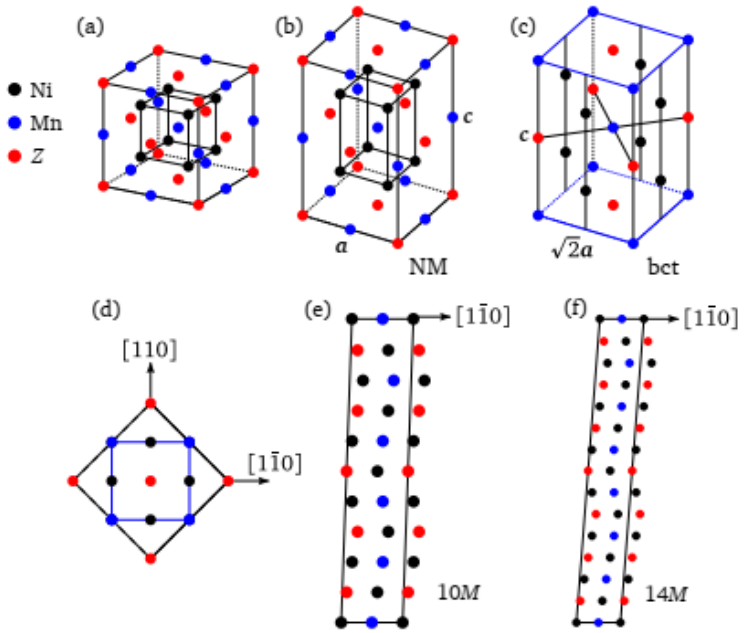

FIGURE 2.8: Visualization of the crystal structures for martensitic Ni-Mn-Z Heusler compounds. Shown are the a) $L2_1$ unit cell of the austenite, b) the non-modulated (NM) martensite and the alternative $L1_0$ bct unit cell c). The relation between them is visualized by the top-down view in d). The 10M unit cell is shown in e) and the 14M cell in f). The figure is taken from Teichert [27].

They can be constructed from periodically stacking basal planes, which are derived from the (001) planes of the $L1_0$ martensite structure. Each basal plane is displaced in the $[1\bar{1}0]$ direction relative to the neighboring planes. As shown, the 10M modulation consists of 10 shifted basal planes while the 14M structure contains 14. The Zhdanov notation [44] is often used to explicitly describe the stacking periodicity, which is $(3\bar{2})_2$ and $(5\bar{2})_2$ for the 10M and 14M structure, respectively. The type of modulation occurring in an alloy depends on the lattice parameters of the austenite and martensite phases. In $Ni_{50}Mn_{25+x}Ga_{25-x}$ and $Ni_{50}Mn_{25+x}Sn_{25-x}$ systems the occurrence of NM, 10M and 14M martensite is dependent on the chemical composition of the alloys.

In this work thin films of the Ni-Mn-Al system are investigated. It is experimentally and theoretically confirmed that the stoichiometric composition $Ni_{50}Mn_{25}Al_{25}$ does not exhibit a MT. For becoming a MSMA Al has to be substituted by excess Mn atoms such that their general formula is given by $Ni_{50}Mn_{25+x}Al_{25-x}$. Thin film studies have confirmed the existence of the 14M modulated martensite structure in this alloy [16]. The Ni-Mn-Al system has a metamagnetic phase transition from a weak ferromagnetic austenite state with a Curie temperature T_c below room temperature to a martensite phase, which exhibits antiferromagnetic coupling or spin glass behavior. For applications it is often beneficial to increase the magnetization and T_c in the austenite state, which can be achieved by substituting Ni atoms by ferromagnetic materials such as Co or Fe. Dutta et al. [6, 45] explained this behavior by ab-initio calculations. In the absence of these substitution elements the magnetic moments of the host Mn-sublattice and the excess Mn atoms occupying the Al sublattice sites couple antiferromagnetically in the austenite state. Upon addition of Co or Fe the strong ferromagnetic exchange interaction between them and the Mn atoms aligns the magnetic moments in parallel irrespective of their positions in the crystal lattice, thus increasing the magnetization. The magnetization in the martensite state however remains unaffected as the strongest ferromagnetic exchange in this configuration is still three times smaller than the antiferromagnetic exchange between the host and excess Mn moments.

Several experimental studies have confirmed that the martensitic transformation temperature depends almost linearly on the mean number of valence electrons per atom (e/a) in the NiMn-based Heusler systems [7, 46]. Thus, it is possible to tune the transition temperature in $Ni_{50}Mn_{25+x}Al_{25-x}$ by adjusting the Al content of a large temperature range from 50 K to 550 K [46–48]. This system is very sensitive to the Al content as it was shown in bulk samples that a difference in 2 at % corresponds roughly to a shift in the transformation temperature of about 100 K [49]. The introduction of Co results in a nonlinear dependency of T_{MT} of the (e/a) ratio. Furthermore, with increasing Co concentration the martensitic transformation shifts to higher temperatures. In compositions with a large $T_c - T_{\mathrm{MT}}$ difference it was found that the martensitic transformation can be completely suppressed [50]. The magnetic contribution to the total entropy change ΔS_{tot} is of opposite sign as the lattice contribution. It is experimentally verified that if the magnetic contribution is on the same order of magnitude the total entropy change decreases with increasing $T_c - T_{\mathrm{MT}}$ until the MT would not lead to a favorable entropy change anymore. Thus the martensitic transformation is depleted. This is known as the kinetic arrest phenomena and provides a lower limit to the transformation temperature range in the NiMn-based shape memory alloys.

Experimental methods 3

In this chapter the theory behind the sample preparation by sputter deposition and characterization by x-ray diffraction are presented. Briefly, only the most important aspects relevant for this work are covered. For further interest the reader is referred to additional literature as for both methods several good references are available [51–53].

3.1 Sputter deposition

Fabrication of thin films by sputter deposition is a well as established method in both research and development as well in industrial manufacturing. Over the years many different modes of operations, such as DC, RF, pulsed, reactive gas or ion beam assisted deposition have been developed and thus a large variety of materials can be deposited as thin films. Even the mechanical and

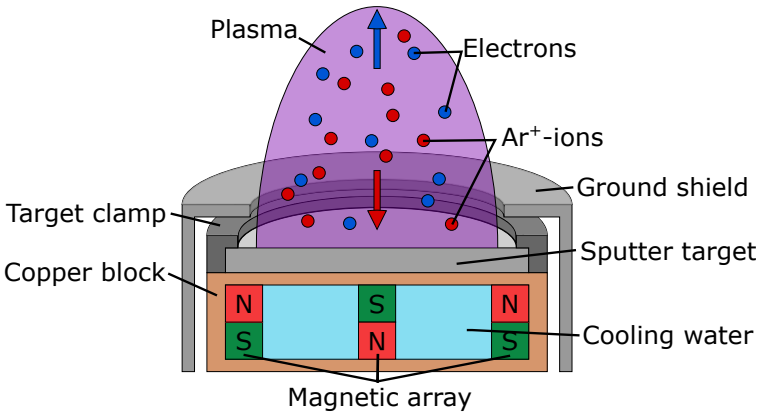

Figure 3.1: Illustration of a cross section through a typical magnetron sputter source used in thin film deposition systems.

crystallographic properties can be tuned by choosing the right conditions from the broad parameter space. In this work the most common deposition modes DC and RF are used and will be therefore focused on.

The underlying principal of the sputter deposition technique can be described as follows. Inside an ultrahigh vacuum chamber an inert gas, mostly Ar, is injected under low pressure. A plasma is ignited and the Ar^+-ions are accelerated onto a target surface, consisting of the material for the thin film. Upon impact the target atoms are sputtered off and eventually reach the substrate surface forming a thin layer. A lot of heat is generated on the sputter target and thus it is usually clamped on a water cooled copper block to prevent the target from melting. The sputter source is surrounded by a grounded shield as without it undesired parts, such as the target clamp or the copper block would be exposed to the ion bombardment and contaminate the film. Significant improvements of the deposition rate can be achieved by placing a magnetic array below the target, which extends the path of the electrons. Accordingly, areas of high ionization rates form above the target surface. The plasma can be sustained at lower pressures and therefore the films suffer less from incorporation of sputter gas defects with the drawback of a non uniform erosion of the sputter target, which reduces its lifetime significantly. A simple illustration of a commercial magnetron sputter source is shown in Figure 3.1.

The simplest mode of operation is the DC sputter deposition. By applying a constant negative voltage to the sputter target a plasma is ignited and sustained by Townsend discharge. This kind of operation is limited to conducting target materials as for insulating materials a positive charge would build up at the surface, preventing further Ar^+-ions from reaching the target. In order to deposit from insulating materials RF-mode operation has been developed. Instead of a constant voltage an alternating electric field, which changes its sign after half a cycle, with a commonly used frequency of 13.56 MHz is applied to the target. The microwave field not only serves to ignite the plasma but also the reversing sign of the field ensures that the net current onto the target surface remains zero after one full cycle. A DC bias has to be superimposed to the RF-field to account for the different mobilities of the electrons and Ar^+-ions. At such high frequencies the circuit has to be matched by an impedance network to prevent power to be reflected to the generator.

The sputter chamber used in this work, manufactured by Bestec GmbH, is equipped with eight magnetron sputtering sources, which are arranged in a confocal sputter-up geometry around the central substrate sample holder. The sputter sources hold 3" targets and six of them are operated in DC-mode while the other two are operated in the RF-mode. Due to limitations of the machine when sputtering from four sources simultaneously, one RF

source and 3 DC sources have to be used. The distance between targets and the substrate is 21 mm. A boron-nitride radiation heater is incorporated into the sample holder and allows heating the substrate to temperatures as high as 1000 °C. To compensate the non uniform deposition due to the confocal arrangement the substrate is rotated constantly during deposition with a speed of 10 rpm. Ar gas is injected with a flow rate of 10 sccm and the pressure in the chamber is regulated by a butterfly valve in front of the turbo molecular pump.

3.2 X-ray diffraction

Sample characterization by x-ray diffraction (XRD) techniques has become an integral part of material analysis since the discovery of x-rays. The measurements are generally nondestructive and often does not need any complex sample preparation beforehand. Many different samples can be investigated, ranging from nanoparticles to powders, bulk materials, thin films and even biological samples. XRD is suitable and accurate to determine crystal structures, symmetries, disorder, grains as well as texture and strain analysis, which is another reason for the wide success of this measurement method.

The general concept of XRD can be described as follows. A monochromatic beam of x-rays with a wave vector $\vec{k}_{in}$ is focused on the sample under an angle ω and scattered by the electron hulls of the sample atoms. The scattered intensity is then monitored in an angle θ by an x-ray detector. If the atoms are arranged periodically on a lattice the transformation into k-space shows discrete points, which reflect the periodicity of the sample. Their position $\vec{G}$ is given by the Miller indices h, k, l and the reciprocal lattice vectors $\vec{b}_j$:

$$\vec{G} = h \cdot \vec{b}_1 + k \cdot \vec{b}_2 + l \cdot \vec{b}_3. \tag{3.1}$$

The reciprocal lattice vectors are calculated from the crystal lattice vectors $\vec{a}_i$:

$$\vec{b}_j = \frac{2\pi}{V} \vec{a}_m \times \vec{a}_n, \tag{3.2}$$

where V is the volume of the unit cell. An illustration of the [001]/[100]-plane in the reciprocal space from a simple cubic lattice is shown in Figure 3.2 along incident $\vec{k}_{in}$ and the diffracted $\vec{k}_{out}$ wave vectors. If the difference in $\Delta\vec{k} = \vec{k}_{in} - \vec{k}_{out}$ equals a reciprocal lattice vector $\vec{G}$ the diffracted waves interfere constructively at the detector and a diffraction peak will be visible, leading to the Laue equation:

$$\vec{G} = \Delta\vec{k} = \vec{k}_{in} - \vec{k}_{out}. \tag{3.3}$$

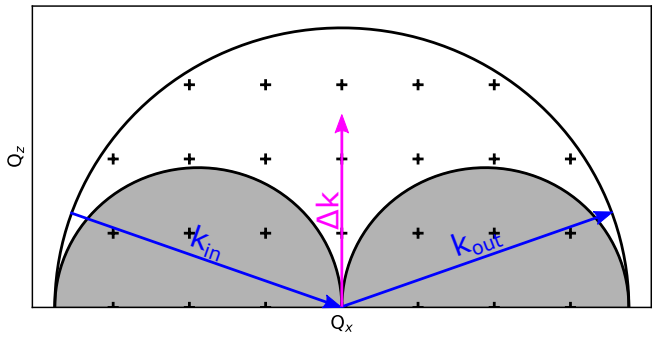

Figure 3.2: Schematic of a 2D slice in the reciprocal space of a simple cubic system. Only reciprocal lattice points (crosses) lying inside the Ewald sphere (outer cirlce) are relevant for a diffraction experiment. The grey shaded half-circles indicated regions of the reciprocal space, which are not accessible in a diffractometer. Also shown are the incident and diffracted wave vectors (blue arrows) and the difference vector (pink arrow) for a usual scattering geometry.

Eq. 3.3 is equivalent to the better known Bragg-equation:

$$n \cdot \lambda = 2 \cdot d_{hkl} \cdot \sin(\theta), \tag{3.4}$$

which links the wavelength λ, the order of diffraction n, the diffracted angle θ and the inter planar spacing of the hkl-planes d_{hkl}.

The used diffractometer in this work is a Phillips X'pert Pro MPD diffractometer equipped with Cu-anode, a secondary curved graphite monochromator and a proportional counter detector. In standard configuration the goniometer operates as a two-cycle goniometer in Bragg-Brentano geometry. A detailed list of the optics for this configuration is shown in Figure 3.3.

In this configuration a custom made cryostat can be mounted onto the multipurpose sample stage to allow temperature dependent measurements in the range from 140 – 400 K. The cryostat consists of a vacuum chamber with polymide x-ray windows. The sample is placed on a copper block, which is cooled by LN_2 from a pressurized Dewar. A self-wound resistive heater in the copper block controls the temperature. Temperature is monitored by a PT1000 sensor and feedback is provided by PID-loop control from a Newport temperature controller.

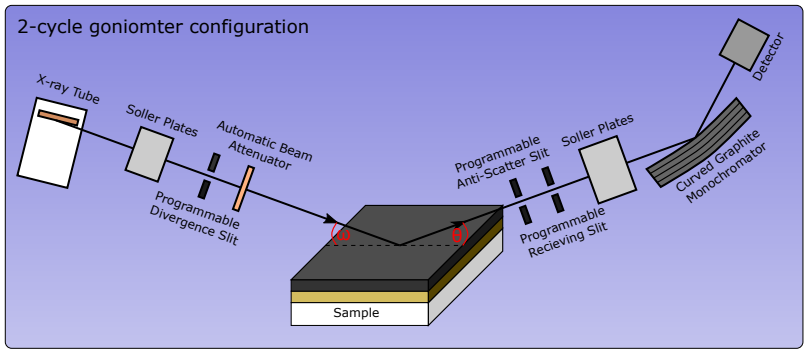

FIGURE 3.3: Illustration of the 2-cycle configuration. All optical elements of the diffractometer used in this work are shown as well.

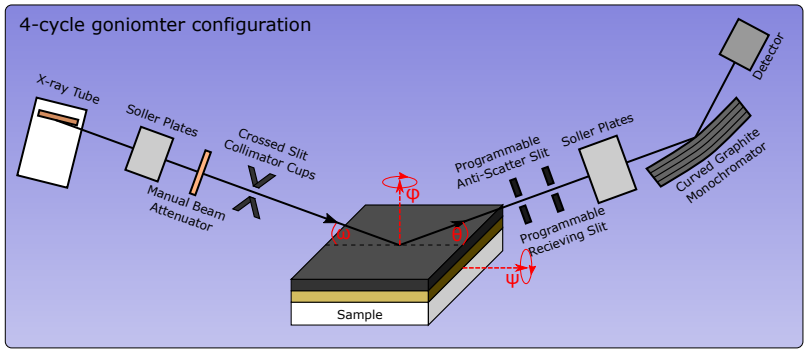

FIGURE 3.4: Illustration of the 4-cycle configuration with a eularian cradle. All optical elements of the diffractometer used in this work are shown as well. The rotational axis for ϕ and ψ are indicated by the red arrows.

In this configuration not all reciprocal lattice points within the Ewald sphere can be reached as indicated in Figure 3.2 by the grey half cycles. In these areas either the diffracted beam or the incident beam have to be below the sample surface. In order to reach these points an eulerian cradle sample stages can be employed in the system changing the diffractometer in a four-cycle goniometer. This configuration is shown in Figure 3.4.

An important technique used throughout this work to characterize epitaxial thin film samples are texture measurements. The scattering vector $\Delta\vec{k}$ is held constant throughout the measurement while the sample is rotated

by the eularian angles $\phi \in [0°, 360°]$ and $\psi \in [0°, 87°]$. The intensity is recorded for each ϕ, ψ-pair. These rotations cause a movement of the reciprocal lattice points along the surface of a sphere in the reciprocal space. A diffraction peak is observed in this map if Equation 3.3 is met at a ϕ, ψ-combination. From this the orientation of the unit cell and the peak symmetry can be determined. The intensity maps are often displayed in pole figures. The polar angle ϕ is maintained as the polar angle in the pole figure while the azimuth angle ψ is encoded in the radius. In this work the coordinate system is always defined by the MgO-substrate. The center of the pole figure at $\psi = 0°$ corresponds to the $[001]_{\mathrm{MgO}}$ direction, $\phi = 0°,\ \psi = 90°$ corresponds to the $[100]_{\mathrm{MgO}}$ direction and $\phi = 90°,\ \psi = 90°$ corresponds to the $[010]_{\mathrm{MgO}}$ direction.

Not only is the angle of diffraction important but the intensity of the peaks contain a lot of information about the sample system as well. The effect on disorder, in the context of Heusler systems, is discussed in the next subsection.

3.2.1 Role of disorder in Heusler systems on diffraction peaks

The main contribution to the intensity of a diffraction peak is the structure factor F_{hkl}, which is a measure of the scattering potential of the crystal lattice. It is calculated by:

$$F_{hkl} = \sum_{n=1} N f_n \cdot e^{[2\pi i(x_n h + y_n k + z_n l)]}, \tag{3.5}$$

with f_n being the atomic scattering factor and x_n, y_n, z_n the coordinates within the unit cell of the n-th base atom. As a consequence certain hkl diffraction peaks cannot be observed even if the Laue-condition is satisfied depending on the crystal structure. Therefore it is possible to distinguish between e.g. a simple cubic from a face-centered cubic and body-centered cubic lattice.

Considering the general Heusler structure, it is best described as four interpenetrating f.c.c. sublattices A, B, C, D with the base coordinates:

A	B	C	D
(0,0,0)	(0.25,0.25,0.25)	(0.5,0.5,0.5)	(0.75,0.75,0.75)
(0,0.5,0.5)	(0.25, 0.75,0.75)	(0.5,0,0)	(0.75, 0.25,0.25)
(0.5,0,0.5)	(0.75,0.25,0.75)	(0, 0.5, 0)	(0.25,0.75,0.25)
(0.5,0.5,0)	(0.75,0.75,0.25)	(0,0,0.5)	(0.25,0.25,0.75)

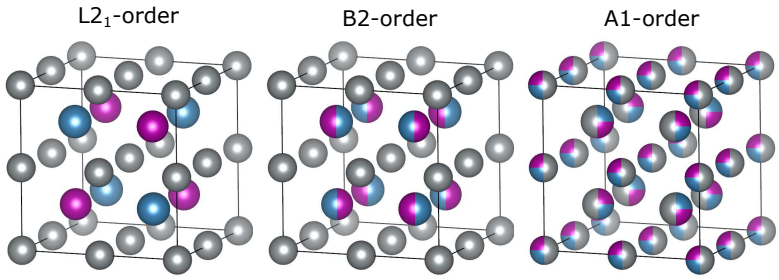

FIGURE 3.5: Illustration L2$_1$- (left), B2- (middle) and A1-ordering present in Heusler compounds.

and average scattering factors f_A, f_B, f_C, f_D. evaluating this for the (111), (200) and (400) planes and rearranging yields following results [54]:

$$\begin{aligned} F(111) &= 4\sqrt{(f_A - f_C)^2 + (f_B - f_D)^2} \\ F(200) &= 4[f_A - f_B + f_C - f_D] \\ F(400) &= 4[f_A + f_B + f_C + f_D] \end{aligned} \tag{3.6}$$

It can be seen, that there are two types of diffraction peaks. One type is always visible since it involves only sums of the average scattering factors and the other one is only visible under certain conditions. The first type is called principle reflections and the other ones are signatures of the ordering present in the unit cell. In the case of the standard L2$_1$-ordering in Heusler compounds with chemical formular X$_2$YZ the structure factors are the following ($f_A = f_C = f_X, f_B = f_Y, f_D = f_Z$) all of the above reflections are visible. This changes in the presence of B2-ordering where the Y- and Z- sublattices are interchanged equally. In this case the average scattering factors become $f_B = f_D$ and therefore the (111) plane is not visible anymore. Upon further decrease in ordering, which results in A1-ordering, where the atoms of the sublattices are intermixed equally all scattering factors become the same, thus only the principal 004-diffraction peak remains visible. Those three peaks are therefore suitable to determine the atomic disorder in the sample. A visualization of the three discussed ordering present in Heusler compounds in shown in Fig. 3.5.

The principle 004-diffraction peak is also suitable to quantify the martensitic phase transformation, as it is not dependent on the ordering in the sample and is one of the most intensive peaks. Therefore, the peak is measured and a linear background is subtracted. The peak is then fitted with two

PseudoVoigt-functions with an fixed ratio of 1:0.5 for the $K_{\alpha 1}$ and $K_{\alpha 2}$ contributions. If a martensite peak becomes visible, it is fitted by PseudoVoigt-functions as well, to increase the accuracy. The area under of the peak is then normalized to the highest measured area in the fully austenitic state. Thus, the residual austenite fraction can be measured for a given temperature.

The magnetic proximity effect in Ni_2MnAl 4

In this chapter the enhancement of the magnetization in Ni_2MnAl by the magnetic proximity effect is described. After an introduction to the subject a brief overview of the theoretical aspects of XMCD and XRMR measurements is given to the reader. In the experimental section the sample preparation and pre-characterization is presented first followed by the results of the impact on the Ni and Mn magnetic moments.

4.1 Introduction

In chapter 2.2 it was shown that the difference in the Gibbs free energy between the martensite and austenite is proportional to the difference in magnetization M between the two phases:

$$\Delta G \propto -\mu_0 H(M_A - M_M). \tag{4.1}$$

In the development of inverse magnetocaloric materials many experimental studies confirmed that a large change in magnetization from the martensite to the austenite state is necessary to drive the phase transformation efficiently. Conventionally this is achieved by the substitution of Ni by a ferromagnetic material such as Fe or Co. Ab-initio calculations show that the substitution leads to an enhancement ferromagnetic coupling between the host Mn atoms and the excess Mn atoms in the austenite state.

Another coupling phenomenon, which is able to enhance magnetic properties, is the magnetic proximity effect (MPE). When two materials with different magnetic order are in close vicinity, the static magnetic exchange coupling leads to a change in of magnetism at the interface due to coupling to the other material. This effect is strongly related to the exchange Bias effect in AFM/FM-bilayer samples. The MPE has not yet been considered for manipulating MSMA materials but could be an interesting alternative to the aforementioned substitution with FM materials.

Directly measuring the change in magnetization due to the MPE during MT is challenging because thin films do not show a complete transfor-

mation into the martensitic state, even at very low temperatures. In such a structurally and magnetically inhomogeneous thin film the separation of the contributions from the martensite and austenite phase is not easily possible. Therefore, in order to determine the strength and interaction length of the magnetic exchange coupling in a proof-of-concept study, a Heusler compound with an effective magnetic moment as low as possible is the material of choice.

For this reason, stoichiometric Ni_2MnAl is an optimal candidate for this proof of concept study. Theoretical [55, 56] and experimental [57, 58] investigations have confirmed that this alloy is antiferromagnetic in the B2 structure with a Néel temperature close to room temperature and FM in its $L2_1$ structure. Bulk studies confirmed that the desired B2 structure can be easily prepared. In contrast, the ferromagnetic $L2_1$ order can only be obtained in $L2_1$ + B2 mixed phases under careful annealing procedures [59]. Furthermore, no martensitic transformation is present in the absence of excess manganese, which enables measurements at very low temperature to enhance signal to noise ratio.

To answer the question whether MT might be improved by a static MPE, we prepared thin Ni_2MnAl/FM bilayer systems and investigated the Ni and Mn moments by x-ray magnetic circular dichroism (XMCD) at their respective $L_{2,3}$-absorption edges. However, from XMCD measurements only the mean spin polarization can be determined. In order to get an estimated value for the penetration depth of the MPE x-ray resonant magnetic reflectivity (XRMR) measurements [60, 61] are employed.

4.2 Theory of XMCD and XRMR

4.2.1 Theory of X-ray magnetic circular dichroism

Absorption experiments with light are often used to investigate the electronic structure of materials and molecules as they are almost non destructive and given the circumstances a lot of information can be extracted from those measurements.

Especially x-rays are often utilized since their high energy photons can also excite the core electrons of the atoms present in the sample. This, is exploited to access information about element specific magnetic properties using the x-ray magnetic dichrosim effect. To probe the ferromagnetism in materials circular polarized light is employed thus the method is called x-ray circular dichrosim (XMCD), which will be described in this section.
In this experiment, the sample under investigation is irradiated with monochromatic and circular polarized x-rays. Two absorption measurements $\mu_+(E)$ and $\mu_-(E)$ are obtained in the energy range of interest by either

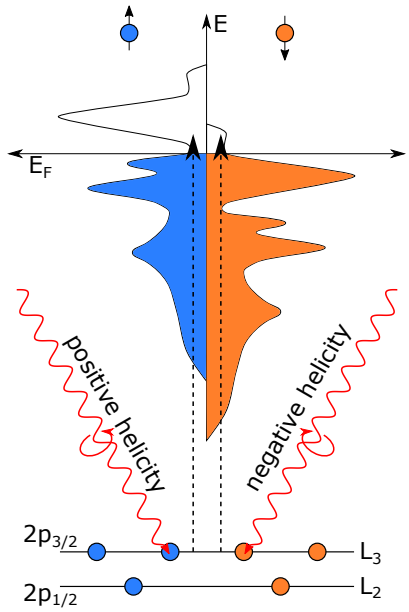

FIGURE 4.1: Illustration of the excitation process in a x-ray absorption experiment with circular polarized light in a ferromagnetic material.

fixing the direction of the external magnetic field to saturate the sample and switching the helicity of the incident light or equivalently by fixing the helicity and switching the direction of the magnetic field. For the 3d transition metals, which are investigated in this work, the usual energy intervals cover the $L_{2,3}$-absorption edges. The absorption process can be explained in a one-electron picture and is illustrated for the L_3-absorption in Figure 4.1.

Absorption of a photon with sufficient energy is absorbed in the sample it can excite an electron from the $2p_{3/2}$ or $2p_{1/2}$ orbital to the d band. If polarized light is used the process becomes dependent of the spin of the electron according to Fermi's selection rules for conversation of angular momentum. In a ferromagnetic material the d bands for the minority (blue) and majority (orange) electrons are not symmetric but are shifted by a small energy difference thus, leading to a different amount of available free states N_h for the spin channels. Since the transition probability is proportional to N_h there will be a difference in the absorption of left and right circular polarized light. For analysis the average absorption (XAS-signal) and the difference in absorption (XMCD-signal) are then calculated from $\mu_+(E)$

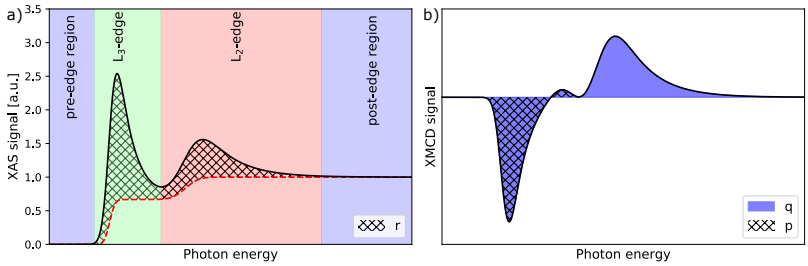

Figure 4.2: Illustration of a) the average x-ray absorption spectra (XAS) and b) the difference in left and right circular polarized light.

and $\mu_-(E)$ according to:

$$XAS(E) = \frac{1}{2}[\mu_+(E) + \mu_-(E)] \tag{4.2}$$

$$XMCD(E) = [\mu_+(E) - \mu_-(E)] \tag{4.3}$$

A typical illustration of those two spectra is shown in Figure 4.2 a) and b).

The spectra can be divided in 4 energy ranges. In the pre-edge region the absorption and difference in absorption should be normalized to zero as the x-ray energy is not sufficient to excite the electrons in the d-band. This is usually accomplished by fitting the experimental data in the pre-edge region with a polynomial of third or fourth order, which is then subtracted from the spectra. The pre-edge region is followed by the the L_3- and L_2-absorption edges. In the post-edge region the XMCD-signal should also fall to zero. It is also common practice to normalize the spectrum in this region to one, which is equivalent of scaling the experimental data to a fixed thickness. Furthermore the data have to be corrected for the incomplete beam polarization P_c and the angle ϕ between the external magnetic field and the x-ray beam by $1/P_c \cos(\phi)$.

The next step in the analysis involves subtraction a background function from the XAS-signal, which arises from electron transitions to unbound free states. This background is assumed to be a two-step like function with the jumps occurring at both absorption edge, which is illustrated in Figure 4.2 a) by a red line. For this work an error-function of the from $A[1 + \mathrm{erf}((E-\mu)/\sigma)]/2$ with:

$$\mathrm{erf}(x) = \frac{2}{\sqrt{\pi}} \int_0^x \exp^{-\tau^2} \, d\tau, \tag{4.4}$$

A the amplitude, μ the centre and σ the width of the step. μ was chosen to be the same as the turning point of the left flank of the respective absorption

edge and σ was fitted to the left flank data points. The amplitude for the two steps are set to a 2:1 ratio due to number of initial electrons in the 2p-states. However, the true background function is usually not known and therefore this can be a large source of error for small XAS signals. The integral r (marked in Figure 4.2 a) by the meshed area) is calculated from the corrected XAS data as well the two integrals p (meshed area in Figure 4.2 b)) and q (blue marked area in Figure 4.2 b)). These quantities are used to determine the orbital magnetic momentum m_{orb} and spin magnetic momentum m_{spin} in the standard sum-rule analysis for 3d-transition metals:

$$m_{orb} = N_h \frac{2q}{3r} \tag{4.5}$$

$$m_{spin} = N_h \frac{(3p - 2q)}{r}. \tag{4.6}$$

N_h has be extracted from ab-initio calculations or from reference data.

Synchrotron facilities offer the possibility to produce monochromatic x-rays over a broad range of photon energies with a high intensity, which is not feasible with standard laboratory equipment. The absorption experiments in this work were performed at the beamline 6.3.1 of the Advanced Light Source (ALS) in Berkeley, USA. Measurements were taken in a Cryostat at 80 K to improve the signal to noise ratio. The beam polarization was fixed and the in-plane external magnetic field was switched between $-0.4\,\mathrm{T}$ and $0.4\,\mathrm{T}$. The degree of beam polarization provided by the bending source was assumed to be $P_c = 60 \pm 0.5\%$ and an angle of $\phi = 30°$ is employed between the incident beam and magnetic field. Two measurement modes can be measured simultaneously, which are depicted in Figure 4.3. In the total electron yield (TEY), which is focused on in this work, Auger and secondary electrons are emitted from the sample surface upon absorption of the incoming x-ray photons. By grounding the sample a net current is measured to quantify the absorption. Due to the limited escape depth of the electrons the probed region of this mode is confined to the surface region, which is marked by the red region in Figure 4.3 a). On the other hand the luminescence yield (LY) is sensitive to the entire thickness of the film. Secondary electrons in the thin film causes excitations in the substrate, which in turn emits light in the visible range. Behind the substrate a photodiode is placed to detect the visible light in the range λ =190 nm to 1000 nm. This detection mode is not applicable for any kind of substrate as suitable emissions bands are not always present. MgO as the substrate material offers a suitable spectral response but produces artifacts in the absorption spectra due to the second order Mg peak at 651.5 eV.

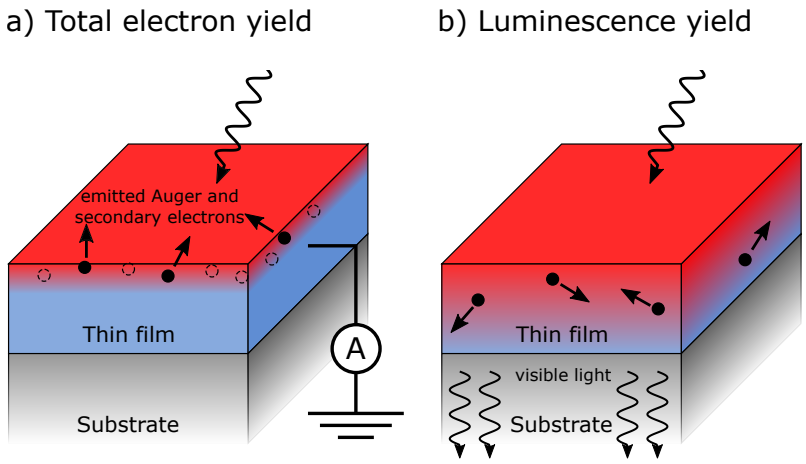

Figure 4.3: Illustration of the probe modes, a) total electron yield (TEY) which is only sensitive to the surface, while b) the luminescence yield (LY) is sensitive to the entire thickness of the film.

4.2.2 Theory of x-ray resonant magnetic reflectivity

Although XMCD is able to provide element specific information about the magnetic interactions in the sample present, it can only provide limited amount of information about the spatial distribution of the magnetism. X-ray resonant magnetic reflectivity (XRMR) has proven to be able to overcome this issue. The measurement is similar to XRD, which is described above in chapter 3, but only grazing incidence angles are recorded. A typical range is from $0°$ to $10°$. In this range the x-rays are not scattered by the crystal lattice but from interfaces of materials with different refraction index n, which is given by a dispersive part δ and an absorption part β accordingly:

$$n(E) = 1 - \delta(E) + i\beta(E). \tag{4.7}$$

The energy of the incident x-rays are set to the absorption edges of the material of interest. Similar to XMCD two reflectivity measurements $I_{\pm}$ are collected with left and right circular polarized light. An average reflectivity (XRR) and an asymmetry ratio ΔI are calculated from these two measure-

ments:

$$XRR = \frac{1}{2}(I_+ + I_-) \tag{4.8}$$

$$\Delta I = \frac{(I_+ - I_-)}{(I_+ + I_-)} \tag{4.9}$$

Exemplary measurements for an XRR and asymmetry ratio are shown in Figure 4.4 for a fictional 30 nm ferromagnetic film.

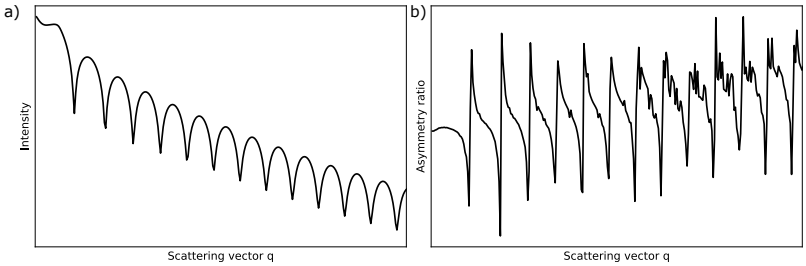

FIGURE 4.4: Illustration of an a) XRR measurement and b) the asymmetry ratio for a fictional 30 nm magnetic material.

Simulation of the XRR data and asymmetry ratios in dependence of the scattering vector $q = (4\pi/\lambda)\sin\theta$, with λ being the wavelength of the x-rays and θ the angle of incidence, are done using the ReMagX software package [62]. Within this model all layers in the multilayer system are described by six parameters: t thickness, σ roughness, β, δ and the magnetooptical parameters β_{mag} and δ_{mag}, which describe the change in absorption and dispersion due to magnetism. The latter two can often be neglected for simulation of the XRR data. The XRR data are analyzed by a recursive Parratt algorithm [63]. For this the true depth profile of multilayer system is approximated by slicing it into m slabs with constant density as shown in Figure 4.5. In this convention $m = 0$ corresponds to the air/vacuum and $m = m + 1$ to the substrate. The ratio between reflection and transmission coefficients of the j-th layer is given by the recursive formula:

$$X_j = \frac{r_j}{t_j} = e^{-iq_{z,j}z_j}\frac{r_{j,j+1} + X_{j+1}e^{iq_{z,j+1}z_j}}{1 + r_{j,j+1}X_{j+1}e^{iq_{z,j+1}z_j}}. \tag{4.10}$$

z_j is the depth of the j-th layer from the top layer, $q_{z,j} = 2k_{z,j}$ and $r_{j,j+1}$ is given by:

$$r_{j,j+1} = \frac{q_{z,j} - q_{z,j+1}}{q_{z,j} + q_{z,j+1}}. \tag{4.11}$$

It is assumed that no reflection occurs from the substrate layer, thus $X_{m+1} = 0$. The total reflection from the multilayer system is calculated from $R = |X_0|^2$. The roughness of the layers is often treated within the Névot-Croce approximation. This assumes that the interface profile can be approximated by an error-function as defined in Eq. 4.4. Equation 4.10 have to be multiplied by the additional exponential damping factor $e^{-0.5 q_{z,j} q_{z,j+1} \sigma^2_{j,j+1}}$.

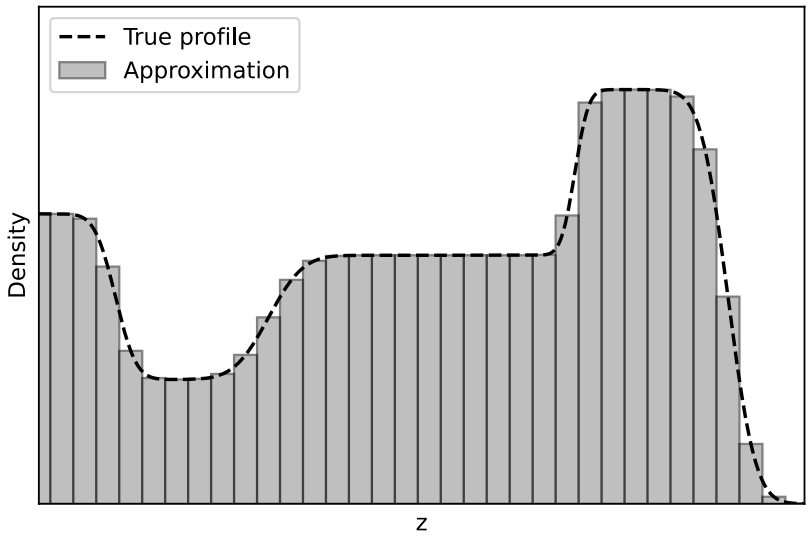

Figure 4.5: Illustration of the slicing of the depth profile.

For the analysis of the asymmetry ratio the Zak matrix formalism [64] is used to fit the data because the Parratt algorithm does not account for the change in polarization upon reflection from the layers. The difficulty of this measurement method is the large number of free parameters, therefore for multilayer systems a careful analysis scheme has to be employed, which will be described in the following.

First the XRR data are analyzed. An initial model for the multilayer system is developed by means of other acquisition methods, such as Auger depth profiling. Based on this the model is refined by fitting only the thicknesses and roughnesses of the layers for the off-resonant data. The optical parameters β and δ are not fitted, because far from any absorption edges both tend to not vary much. They can be extracted or calculated in the case of alloys from the Henke tables [65]. The refined values are exported and the resonant XRR data are fitted by only refining this time β and δ for each element available. If not for all XRR-measurements a consistent solution

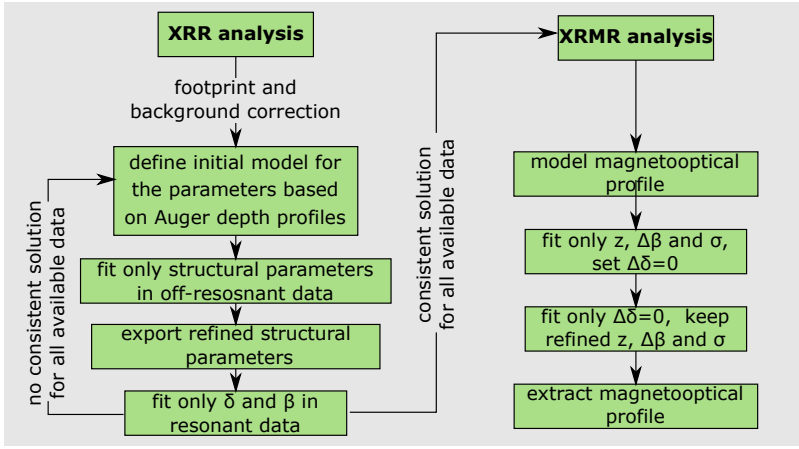

FIGURE 4.6: Analysis scheme for the analysis of the XRMR data (adapted and modified from [61]).

is found another model for t and σ have to be found and the process is repeated. In case of a consistent solution the asymmetry data is analyzed. For this an artificial magnetooptical profile is defined in the shape of a Gaussian function with center z and width σ for β_{mag} and δ_{mag}. The Gaussian profile is convolved with the density profile of the layer. The FWHM of the resulting function is defined as the effective penetration depth for the MPE. In order to reduce the number of free parameters a two step fitting procedure is employed. For the first fit δ_{mag} is set constant to 0, as given by the Kramers–Kronig relations at the absorption edge. The other parameters are then refined. In the second step z, σ and β_{mag} are then held constant and δ_{mag} is refined. The whole analysis procedure is illustrated in Figure 4.6. A more sophisticated analysis scheme can be found in [61, 66].

4.3 Experimental details

4.3.1 Sample preparation and pre-characterization

Thin film multilayer systems were prepared by dc magnetron sputter deposition in a vacuum system with a base pressure $< 5 \times 10^{-9}$ mbar. 10 nm thick Ni_2MnAl films were co-deposited from pure element Ni-, Mn- and Al-targets onto MgO(001) substrates at 450 °C to achieve epitaxial growth conditions. Different 1 nm thick FM layers consisting of Co or Fe were

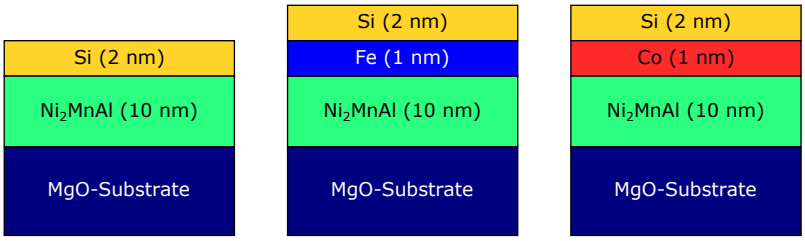

Figure 4.7: Illustration of the investigated multilayer systems for the study of the magnetic proximity effect. The samples are labeled by their ferromagnetic layer respectively from the left to the right: No-layer, Fe-layer, Co-layer.

deposited on top of the Heusler material. A sample without a FM layer severed as a reference. To prevent from oxidation, all samples were capped by a 2 nm Si layer. Prior to the deposition of any FM and capping layers the samples were cooled down to room temperature with a rate of 16 K/min to avoid interdiffusion into the Heusler layer. Stoichiometry of the Heusler layers was derived from the individual deposition rates of the elemental targets. All sample systems are illustrated in Figure 4.7 and are labeled according to their FM layers: No-layer, Fe-layer and Co-layer. An additional sample with a 100 nm thick Ni_2MnAl film on top of a MgO-substrate served to determine the crystal growth and structure.

To investigate the deposition and crystallization behavior of the Ni_2MnAl film, x-ray diffraction was preformed on a 100 nm thick film. The thin films grow epitaxially on top of the MgO-substrates with an in-plane relationship $[110]_{MgO}$ || $[100]_{Ni_2MnAl}$ and an out-of-plane relationship $[001]_{MgO}$ || $[001]_{Ni_2MnAl}$ as determined by texture measurements (shown in Figure 4.8 b)), which is a common growth behavior for Heusler compounds on this substrate. $\theta/2\theta$-scans along the [001], [101] and [111] crystallographic directions of the Ni_2MnAl are shown in Figure 4.8 a). Along the principal (004), (202), (222), (404) and (444) diffraction peaks the order dependent (002) peak is also observed indicating the desired B2 phase. The odd superstructure peaks (111) and (333), associated with the FM $L2_1$ phase, are not observed in the $\theta/2\theta$-scan along the [111] direction. The lattice constant was determined to be a = 5.83 Å, which is in good agreement with bulk values [59].

A temperature dependent resistivity measurement was additionally performed for the 100 nm thick film in a closed loop helium cryostat between 2 K and 300 K in van-der-Pauw geometry. The measurement is shown in

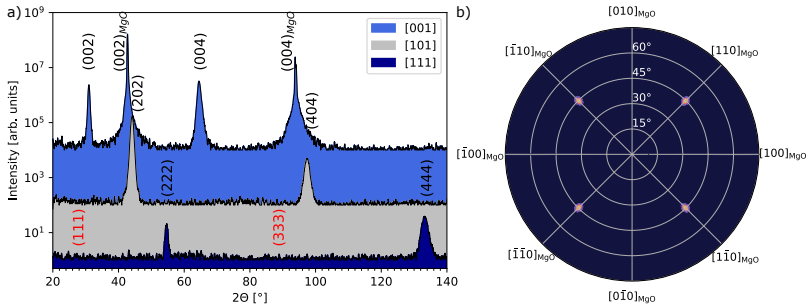

FIGURE 4.8: X-ray diffraction measurements of a 100 nm thick Ni_2MnAl film. Shown are $\theta/2\theta$-scans along the [001], [101] and [111] direction of the Heusler compound. MgO-substrate peaks are subscripted and the red marked Miller indices indicate the position of the absent Ni_2MnAl diffraction peaks.

Figure 4.9. For this measurement the sample is split into a 5 x 5 mm piece and glued to a sample holder. On the four corners of the sample Au 50 nm thick contact pads are placed by sputter deposition. Electrical contact between the samples and holder was achieved by Au-wire bonding to avoid possible thermoelectric artifacts in the measurements due to dissimilar materials. The exact size of the sample is irrelevant as the geometric spacing of the contacts are irrelevant for the van-der-Pauw method. The measurement can be described as follows: On two neighboring contacts a constant current is applied, while the voltage drop is measured. At least four measurements need to be taken for this method. The contacts are then rotated and four voltage drops are measured while the constant current is applied. The sheet resistance ρ is then calculated by:

$$\rho = \frac{\pi}{\ln 2} f t \frac{V_1 - V_2 + V_3 - V_4}{4I}. \tag{4.12}$$

In this equation t is the film thickness and f a geometric correction factor, which has to be solved numerically by the following equation:

$$\frac{Q-1}{Q+1} = \frac{f}{\ln 2} \operatorname{arccosh}\left(\frac{e^{\ln 2/f}}{2}\right) \tag{4.13}$$

with $Q = \frac{V_1 - V_2}{V_3 - V_4}$. For the prepared film a sheet resistance of 1.1 µΩ cm to 1.2 µΩ cm was measured in the investigated temperature range. The behavior is typical for a metal, following a linear relationship for temperatures

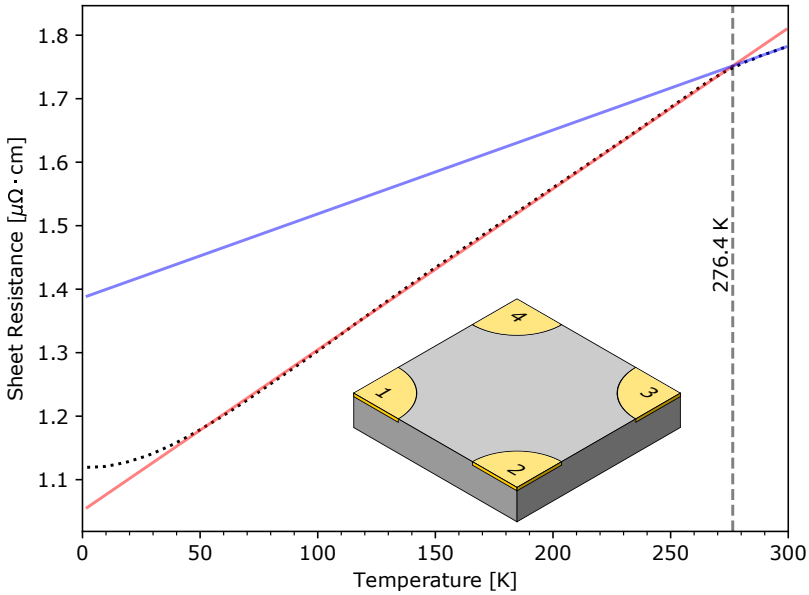

Figure 4.9: Sheet resistance in dependence of temperature for a 100 nm thick Ni_2MnAl film on MgO measured in van-der-Pauw geometry with gold deposited contact pads at the four corners of the sample.

above 50 K and reaches a saturation value for very low temperatures due to defect scattering. A kink is observed at a temperature of (267.4 ± 0.1) K. This kink is theoretically predicted for antiferromagnetic materials near the Néel temperature due to fluctuations of the sublattice magnetizations [67] and were first measured in bulk antiferromagnetic MnIr [68] and MnPt [69] . Thus the temperature of this kink is regarded as the Néel temperature which corresponds well with the values for Ni_2MnAl thin films reported by Tsuchiya et. al. [70]. The reported value is lower than the ones reported for bulk [59, 71].

Antiferromagnetic B2-ordering is further confirmed by magnetization measurements, which are shown in Figure 4.10 at 80 K for the No-, Fe- and Co-layer samples. Without Co or Fe capping layers no FM response from the pure Ni_2MnAl film could be measured. The hysteretic magnetization loops of the Fe and Co layers are clearly visible in the magnetization data. Both are saturated well below 100 mT.
Furthermore, no enhanced magnetic moment is detected in the Fe- and Co-layer samples in comparison to bulk samples. In fact the saturation magne-

tization of both samples is around 300 kA m^{-1} to 350 kA m^{-1} lower than in bulk (Fe: 1750 kA m^{-1}, Co: 1450 kA m^{-1}) [72]. The reduction could be attributed to interfacial effects or the resolution of the magnetometer.

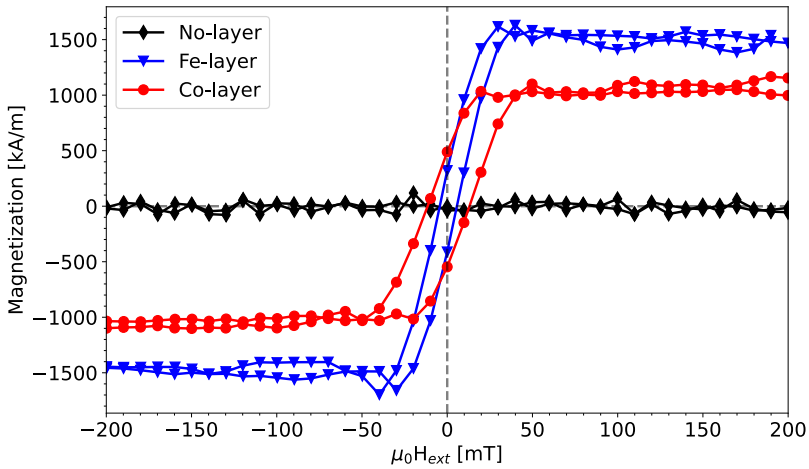

FIGURE 4.10: Magnetic hysteresis loops at 80 K with an external magnetic field applied in-plane for all three investigated sample systems.

4.3.2 Depth profile model for the Fe layer sample

XRMR is a measurement technique, which investigates magnetism reasonably well for simple systems, such as bilayers. However, if several more layers have to be included in the model, analysis becomes quite complicated due to the sheer number of free fitting parameters for simulating a multilayered stack. This results in a parameter space with many local minima and a potentially ambiguous best-fit solution makes it necessary to acquire additional depth profile information or a more complex analysis procedure prior to the fitting process.

In order to support the XRMR analysis with elemental depth profiles, Auger spectra in the energy ranges 25 eV to 106 eV and 483 eV to 523 eV in combination with Ar^+ ion beam milling has been recorded on the Fe-layer sample. The smoothed and differentiated spectra depending on the distance to the substrate surface are shown in Figure 4.11 and Figure 4.12. The Auger lines of Mg, Ni, Al, Fe, Si and O can be clearly identified. Mn on the other hand provides only a slightly pronounced Auger response at 41 eV and is therefore not marked in the spectra. The multilayer system starts with a 85 Å

thick Ni_2MnAl layer on top of the MgO substrate as indicated by the Ni and Al signals, which is followed by an about 20 Å thick Fe layer. The sharp drop off of those signals suggest that no significant interdiffusion between those two layers occurred and that the interface is fairly smooth. In contrast, a large overlap in the Auger signals is observed between the Fe and the 20 Å thick Si capping layer and therefore a very rough interface has to be assumed here. Si proves to be a good protective layer as concluded from the absence of O Auger lines in the Heusler material and Fe layer. Contributions from O can only be seen at the MgO and the topmost Si atomic layers, which is supported by the chemical shift of the Si signal to lower energies [73].

Based on this depth profile a refinement of the layer parameters t and σ is done using an off-resonant XRR scan at 1000 eV. The measurement data can be very well simulated by assuming a model consisting of MgO substrate, Ni_2MnAl, Fe, Si and SiO_2 layers with constant optical parameters δ and β for each layer (Figure 4.13). They can be taken from the Henke tables [65] since far away off the absorption edges they do not change rapidly. The best-fit solution of optical depth profile is shown in Figure 4.14, which is consistent with the previously discussed Auger depth profile.

4.3.3 Magnetic properties of Mn

The normalized XAS along with their respective XMCD spectra for Mn at the $L_{2,3}$ absorption edges are shown in Figure 4.15 for all three sample systems. On first notice, the Mn spectra contain almost no multiplett features as it is in the case for MnO [74, 75] or alloys with large differences in electronegativities of the constituting elements [76]. In fact, the shape of the spectra resembles metallic Mn [77, 78], since the electronegativities of Ni, Mn and Al are close to each other. Additionally, an increased white line intensity of the Co-sample compared to the other two is observed. This could hint to a charge transfer between the Mn and Co atoms. In absence of FM layers, there is no XMCD signal as no differences in absorption between left and right circularly polarized light is detected. This is expected for the antiferromagnetic state in Ni_2MnAl and in accordance with the magnetization data. However, this changes clearly when an Co- or Fe-layer is placed adjacent to the Heusler compound. The presence of an XMCD signal proves at least partial FM ordering between the Mn moments close to the interface.

In order to quantify the induced magnetic moment, standard XMCD sum rules for 3d transition metal elements were applied. For this, a two-step background, as indicated in Figure 4.15, was subtracted from the XAS spectra. Furthermore, the signal was corrected for the angle of incidence 30° and for the degree of circular polarization of the x-rays $\approx (60 \pm 0.5)\%$). The number of free electron states N_h was calculated to be 4.07 using the

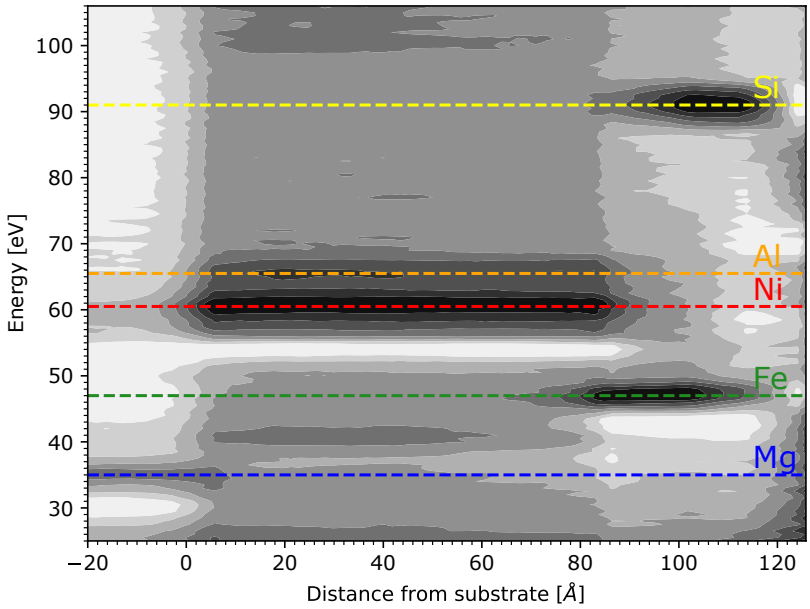

FIGURE 4.11: Smoothed and first derivative of the Auger spectra of the Fe-layer sample in the energy range 25 eV to 106 eV. The interface between the MgO-substrate and the Ni_2MnAl is defined as 0.

ab-initio density-of-states calculation from Ref. [79]. The results for the spin and orbital magnetic moments, m_{spin} and m_{orb}, respectively, are listed in Tab. 4.1. The obtained spin magnetic moments are quite small only yielding $(0.19 \pm 0.02)\mu_B$ for the Fe-layer and $(0.35 \pm 0.01)\mu_B$ for the Co-layer samples. Furthermore, Co seems to have a stronger effect on the induced magnetization than Fe by a factor of around 2. At the same time in both cases the orbital moment is negligible compared to the spin magnetic moment, which is usually the case for the transition metals. However, XMCD can only determine the average magnetic moment at the probed volume and therefore no clear estimation of the penetration depth can be made.

Therefore, XRMR was afterwards performed on this sample at the Mn L_3 edge at the energy of 638.8 eV for the Fe-layer sample. The resonant XRR curve and their simulation are shown in Figure 4.16 with the corresponding normalized asymmetry ratio data in the inset. To determine the induced MPE we define a Gaussian function for the magnetooptic parameters δ_{mag} and β_{mag} close to the Ni_2MnAl/Fe interface, which is convolved with

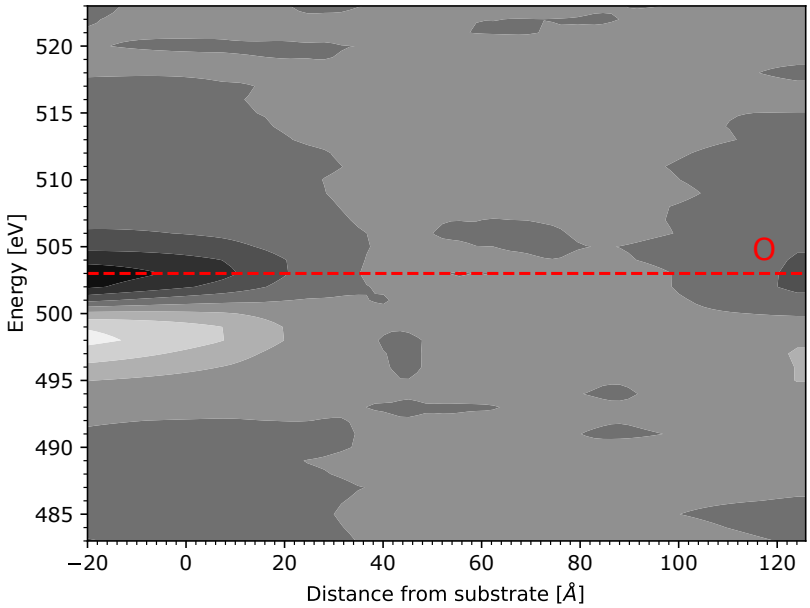

Figure 4.12: Smoothed and first derivative of the Auger spectra of the Fe-layer sample in the energy range 483 eV to 523 eV.

the structural density profile of the Ni_2MnAl layer. The resulting magnetic depth profile is a Gaussian-like curve (slightly asymmetric Gaussian depending on the roughness of the interface). This procedure has been established for the MPE at Pt interfaces. Details can be found in Refs. [61, 66, 80–82]. A close up of the interface region and the determined Gaussian-like magnetic depth profiles are visualized in Figure 4.17. Also shown is the Mn concentration at the interface. We used the FWHM of the magnetic depth profiles to define an effective interaction length, which is determined to be (7 ± 1)Å. This corresponds to the uppermost three to four atomic layers in the Ni_2MnAl. Notably, the magnetic change in dispersion δ_{mag} is significantly lower in magnitude and of opposite sign than the magnetic change in absorption β_{mag}. Such a situation arises for Mn at the energy of maximum absorption at the L3-edge, as it was shown by Brück et al. [83] by applying the Kramers-Kronig relations to reference XMCD data for metallic Mn. Thus considering the relative sign and magnitude of δ_{mag} and β_{mag} the solution seems to be valid model. It should be noted though that only much smaller numbers for the magnetooptic contribution could be retrieved

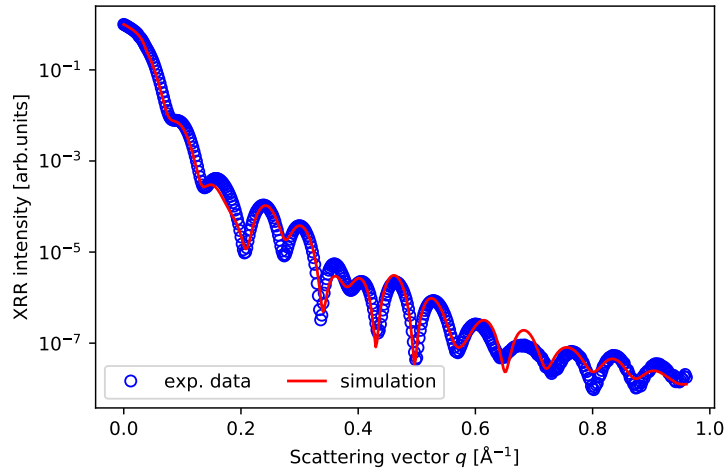

FIGURE 4.13: Off-resonant XRR data (blue circles) and simulation (red line) for the Fe-layer sample at 1000 eV.

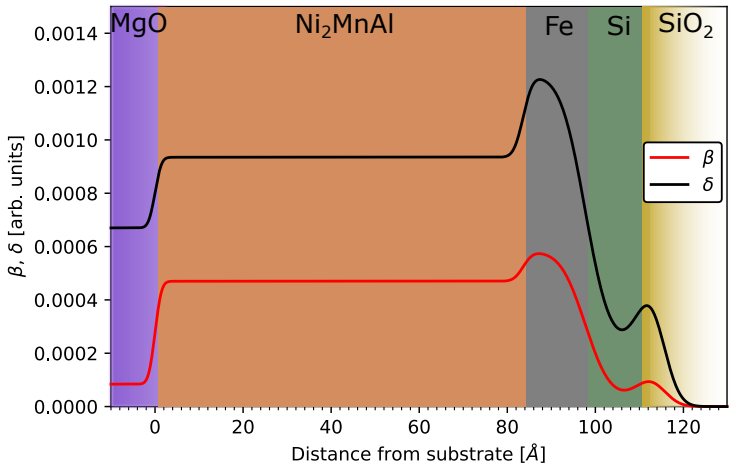

FIGURE 4.14: Magnetooptic δ and β depth profiles determined by the fit model for the off-resonant XRR scan at 1000 eV.

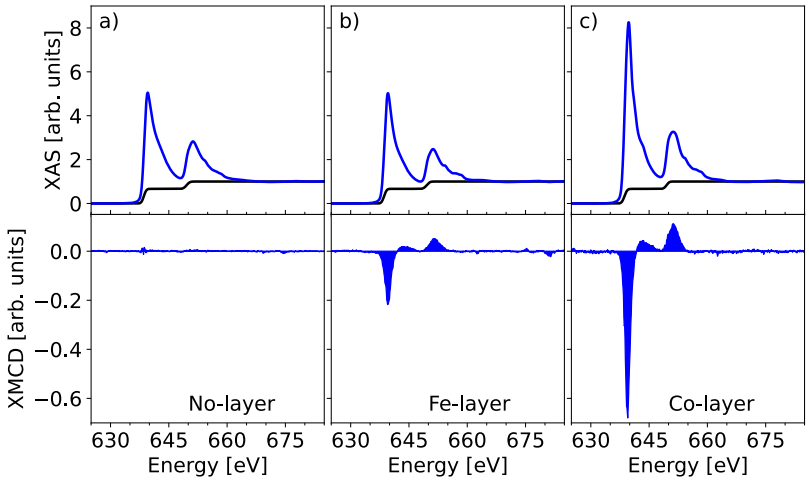

Figure 4.15: XAS and XMCD data from the Mn $L_{2,3}$ absorption edges for a) No-layer, b) Fe-layer and c) Co-layer sample.

Table 4.1: Calculated magnetic moments for Mn extracted from the experimental data in Figure 4.15.

Sample	m_{spin}	m_{orb}
No-layer	$(0.002 \pm 0.001)\mu_B$	$(0 \pm 0.003)\mu_B$
Fe-layer	$(0.19 \pm 0.02)\mu_B$	$(0.03 \pm 0.02)\mu_B$
Co-layer	$(0.35 \pm 0.01)\mu_B$	$(0.07 \pm 0.02)\mu_B$

by applying the Kramers-Kronig relations to our recorded XMCD data in Figure 4.15.

A similar value for the penetration depth is found in the Mn-based antiferromagnet MnPd/Fe bilayers [83] and many studies [84–87] found an induced magnetic moment in antiferromagnets in exchange-bias systems. They attribute this to existence of unpinned rotatable, uncompensated magnetic moments close to the interface. This could also be the case for our investigated systems.

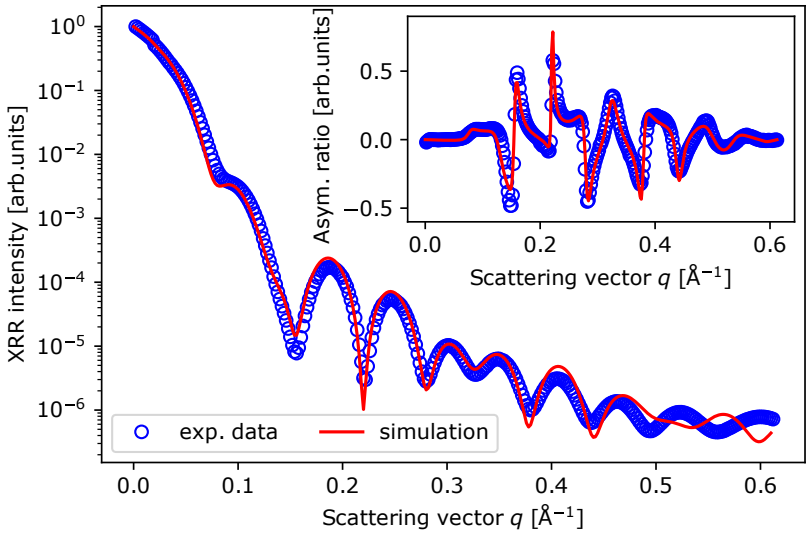

FIGURE 4.16: XRR curve at the Mn L_3-absorption edge at 638.8 eV eV. The inset shows the XRMR asymmetry ratio between left and right circularly polarized light.

4.3.4 Magnetic properties of Ni

The same investigation procedure for Mn was also carried out for the Ni $L_{2,3}$ absorption edges. The XAS spectra shown in Figure 4.18 share the same features observed for Ni_2MnGa, Ni_2MnIn and Mn-rich Ni_2MnIn in the austenitic state [88, 89]. In addition to the strong absorption peaks from the Ni 2p $\rightarrow$ 3d transition, a satellite feature is located at 859.1 eV. Ab-initio calculations for Ni_2MnGa and Ni_2MnIn suggest that this feature stems from a hybridization of the Ni 3d with the Ga 4s and with the In 5s states, respectively. Thus, we conclude the same hybridization is happening with the Al 3s sates. On closer inspection, we find of the Ni 3d with the Ga 4s and with the In 5s states, a small chemical shift in the satellite feature in the presence of an Fe- or Co-layer. In contrast to the Mn absorption spectra, there is no evidence of charge transfer in the case of Co or Fe since there is no change in white line intensity between the three sample systems.

The Ni magnetic moment follows the same behavior as the Mn magnetic moment as there is no signal present in absence of a FM layer. However, again a clear XMCD signal is present at both the Fe and Co-sample. Sum-rule analysis yields the following values for the spin and orbital magnetic

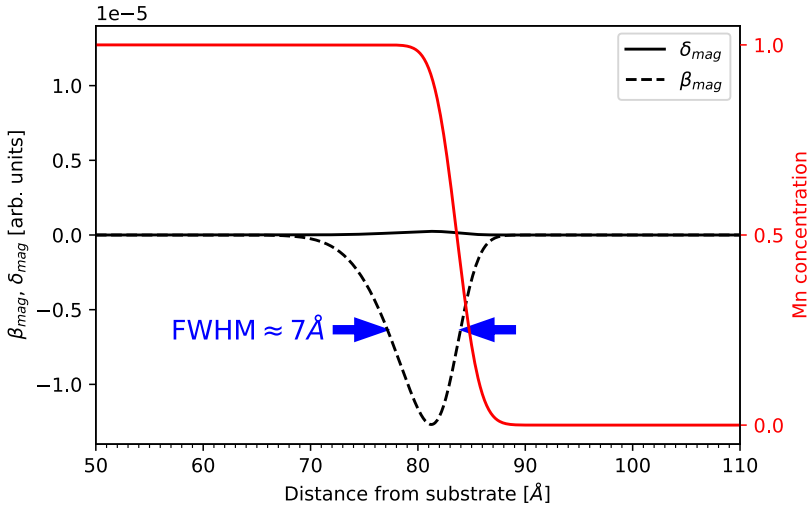

Figure 4.17: Magnetooptic δ_{mag} and β_{mag} depth profile at the Ni_2MnAl/Fe-interface for Mn. The gray line represents the Mn concentration across the interface.

moments in table 4.2, assuming $N_h = 2.22$ [79]. However, due to the low absorption cross section in Ni a large error for these values has to be assumed. For Ni, the obtained magnetic moments are comparable of the ones from Mn. However in this case Co and Fe do have the same impact on the magnitude of the MPE.

Analysis of the XRMR measurements at 851.3 eV shown in Figs. 4.19 and 4.20 yields a similar penetration depth of about (6 ± 1) Å. In this case however, another relation between β_{mag} and δ_{mag} have to be assumed to result in a good fit of the of the asymmetry ratio data. The magnetooptic parameters are of comparable magnitude and of different sign. This is expected to happen at an energy before the absorption edge [83]. The similar penetration depth and magnitude of the FM enhancement compared to the Mn magnetic moments suggest that the origin of this is the same as for the Mn.

In both, Ni and Mn moments a ferromagnetic alignment could be induced by a FM layer on top of the Ni_2MnAl Heusler compound. Due to the structural an chemical similarity we expect that these results apply to $Ni_2Mn_{1+x}Al_{1-x}$ in the austenite phase as well. Thus, the proximity effect would increase the magnetization in the high temperature phase. Comparing the obtained results to ab-initio calculations of the magnetic exchange

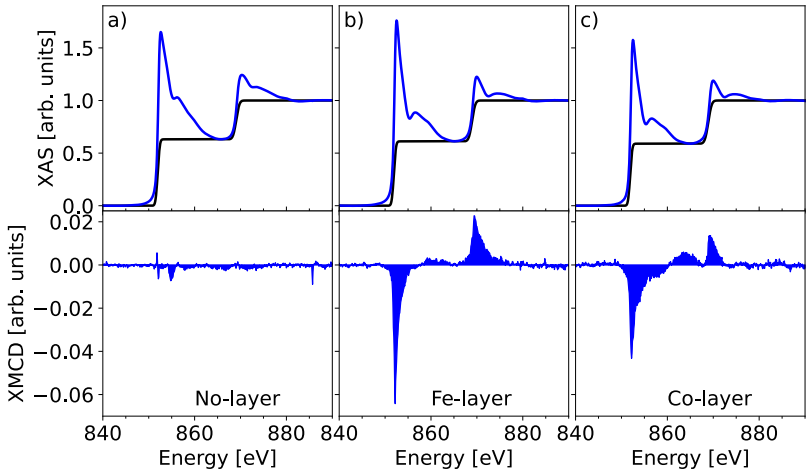

FIGURE 4.18: XAS and XMCD data from the Ni $L_{2,3}$ absorption edges for a) No-layer, b) Fe-layer and c) Co-layer sample.

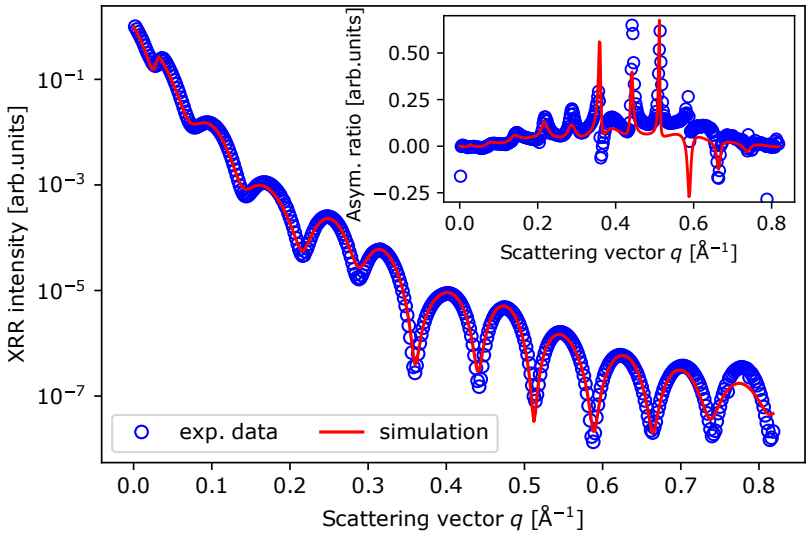

FIGURE 4.19: XRR curve at the Ni L_3-absorption edge at 851.3 eV eV. The inset shows the XRMR asymmetry between left and right circularly polarized light.

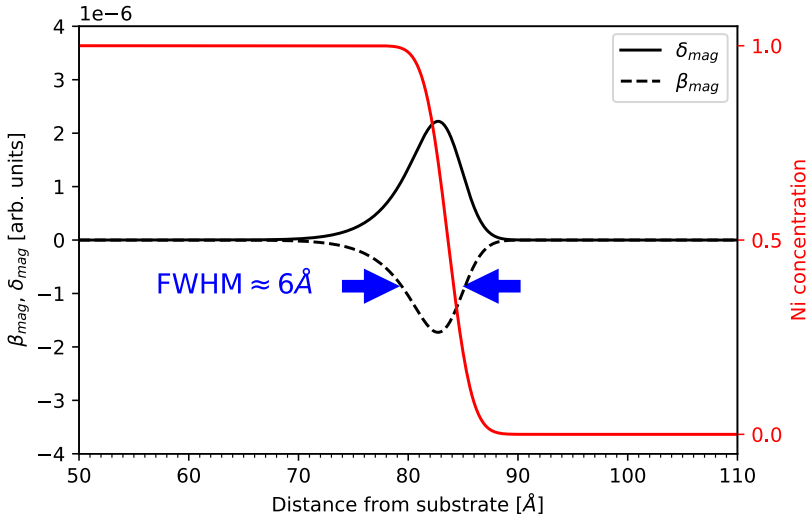

Figure 4.20: Magnetooptical δ_{mag} and β_{mag} depth profile at the Ni_2MnAl/Fe-interface for Ni.

Table 4.2: Calculated magnetic moments for Ni extracted from the experimental data in Figure 4.18.

Sample	m_{spin}	m_{orb}
No-layer	$(0.002 \pm 0.003)\mu_B$	$(-0.003 \pm 0.004)\mu_B$
Fe-layer	$(0.13 \pm 0.07)\mu_B$	$(0.001 \pm 0.07)\mu_B$
Co-layer	$(0.11 \pm 0.06)\mu_B$	$(0.022 \pm 0.03)\mu_B$

parameters in Co-/Fe-substituted $Ni_{50-x}M_xMn_{37.5}Al_{12.5}$ (M = Co or Fe) we find similar properties [6]. The Mn spins on the Al sublattice and the host lattice show an antiferromagnetic interaction, which changes to a FM alignment regardless of their position if Ni is substituted for Co or Fe. Furthermore, Co displays a FM coupling almost twice as strong as Fe, which is also the case for the extracted Mn spin moment in the given study, which further supports the assumption that the MPE has the same effect as substitution.

Not present in our samples is the exchange coupling between the Mn and excess Mn atoms. The ab-initio calculations shows that these moments couple ferromagnetically due to the Fe or Co in the cubic austenite state.

This changes to an antiferromagnetic exchange, which is more than three times larger than any other FM coupling, upon cooling to the tetragonal martensitic state. If the MPE has the same effect on this exchange interaction we expect also the ferromagnetic alignment to vanish. Thus, the MPE would contribute to the difference in magnetization between the austenite and martensite state. However a direct proof is still necessary but as mentioned in the introduction also challenging since the transformed Heusler compound cannot be sliced into several sublayers with constant magnetooptical properties as necessary for the XRMR analysis. Also surface sensitive XMCD could also be problematic because it cannot be guaranteed that the whole interface region transforms into martensite and thus separation of the contribution of martensite and austenite remains difficult.

4.4 Conclusion

In this proof-of-principle study Co or Fe layers are deposited on epitaxial antiferromagnetic Ni_2MnAl thin films and investigated by x-ray circular dichroism (XMCD) and x-ray resonant magnetic reflectivity (XRMR) at the Mn and Ni L-edges. A ferromagnetic response is found in the total electron yield XMCD signal for both Mn and Ni moments close to the interface of the ferromagnetic thin film originating from rotatable uncompensated magnetic moments. Auger spectroscopy is used to establish a structural depth profile for further analysis of the magnetic depth profile in the Ni_2MnAl/Fe sample system by XRMR. A penetration depth of the magnetic proximity effect is determined to be around 7 Å for Mn and 6 Å for Ni. Due to the similarity to the austenite phase of Mn-rich Ni-Co-Mn-Al systems, which exhibit MT, we conclude that the MPE will be able to enhance the austenite magnetization. It has yet to be determined if a martensite phase in this Heusler compound is similarly affected by the MPE. However, the small penetration depth limits the applicability to systems with large surface to volume ratios.

Point defects in ion beam irradiated Ni-Co-Mn-Al magnetic shape memory alloys 5

5.1 Introduction

In chapter 2.4 we highlighted the importance of defects in the crystal lattice for inhomogeneous nucleation to occur during the martensitic transformation. Defects in the form of substrates and seed layers [90] as well as nanoindentation by an atomic force microscope [91] have been investigated in this context before. Still, introducing defects in a somewhat controlled manner inside a crystal is a difficult task. One way to insert point-like defects in a sample after deposition is by low energy heavy ion beam irradiation. If ions are accelerated in a sufficient energy range the collision cascade in the material causes vacancies and interstitial atoms in the crystal lattice. Such techniques are used today in semiconductor physics to insert dopant materials [92]. In order to not artificially dope the system which changes the electronic structure of the target material noble gases are preferred as the ion species for irradiation experiments. The concentration of the inserted defects is proportional to the ion fluence on the sample. Thus the defect concentration can be tailored in a controlled manner. Previous studies in the last years on the magnetocaloric material FeRh [93, 94], which undergoes a first-order isotructural metamagnetic transition, reported a significant influence of ion beam irradiation on the phase transition.

In this chapter a similar study on the Ni-Co-Mn-Al system is presented. This work was achieved in close collaboration with the Helmholtz Zentrum Dresden Rossendorf (HZDR) with Dr. Rantej Bali performing the ion beam irradiation, Dr. Tino Gottschall providing magnetization measurements and Dr. Rene Hübner contributing transmission electron microscopy (TEM) data while sample deposition and XRD investigations were performed at Bielefeld University.

5.2 Sample preparation

Epitaxial $Ni_{45}Co_5Mn_{30}Al_{20}$-thin films were grown on 10 mm x 10 mm (001)MgO-substrates by magnetron sputter deposition. DC and RF sources were used to co-deposit from 3-inch targets of Ni (DC), Mn (DC), Al (DC) and Co (RF) targets with a purity of 4N. Prior to the deposition of the films the substrates were subjected to a chemical ultrasonic cleaning treatment consisting of 10 min in acetone followed by 10 min ethanol and 5 min deionized water. Finally the substrates were annealed at 700 °C for 30 min to remove any residual chemical contaminates. In order to achieve good growth conditions a 30 nm V seed layer is deposited at 450 °C immediately followed by the deposition of the 200 nm Heusler layer. To avoid interdiffusion into the Heusler compound a 2 nm Si capping layer is deposited after cooling down the sample to room temperature.

Subsequently, the samples were cut into 3 mm x 5 mm pieces and irradiated with 150 keV Ne^+-ions at the Ion Beam Center (IBC) facility of the Helmholtz Zentrum Dresden Rossendorf (HZDR). The ion fluence on the sample was varied from 1×10^{12} ions/cm^2 to 5×10^{14} ions/cm^2. A non-irradiated sample is kept as a reference. Temperature dependent magnetization measurements were performed in a Quantum Desgin MPMS instrument at the same facility. Furthermore TEM investigations were done at the Electron Micoscopy Laboratory at the HZDR. A FEI Titan 80-300 microscope is used to investigate the structure and performing selected area electron diffraction (SAED) measurements on samples. A FEI Talos F200X microscope is utilized to obtain EDX mappings of the thin film cross sections. The TEM specimen were prepared by focused ion beam milling in a Zeiss NVision 40.

5.3 Sample pre-characterization

The sputter deposited sample is characterized by XRD for crystallographic properties and by TEM in combination with energy dispersive x-ray spectroscopy (EDX) mapping for homogeneity prior to the ion beam irradiation to determine the initial conditions for the reference.

In Figure 5.1 a $\theta/2\theta$ XRD scan in the 2-cycle goniometer configuration along the $[001]_{MgO}$-direction is shown. Alongside the substrate $(002)_{MgO}$ $((42.909 \pm 0.002)^\circ)$ and $(002)_V$ peak $((60.971 \pm 0.003)^\circ)$ two peaks from the Ni-Co-Mn-Al are visible. The peaks at the 2θ angles $(31.233 \pm 0.008)^\circ$ and $(65.147 \pm 0.003)^\circ$ can be identified as the $(002)_A$ and $(004)_A$ peaks of the cubic austenite phase respectively. Therefore, the epitaxial relationship between the MgO-substrate, V seed layer and Ni-Co-Mn-Al Heusler layer

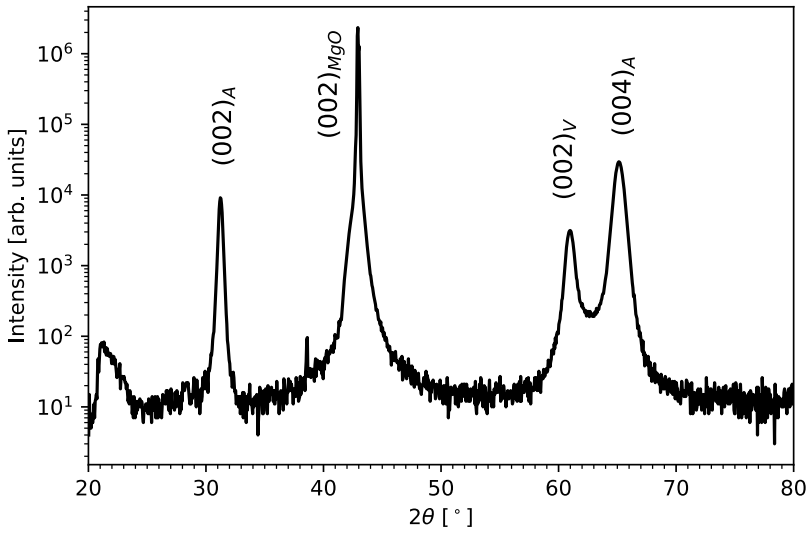

FIGURE 5.1: $\theta/2\theta$-scan for the reference sample.

for the out-of plane direction can be expressed as: $[001]_{\mathrm{MgO}}$ || $[001]_{\mathrm{V}}$ || $[001]_{\mathrm{A}}$. According to the Equation 3.4 the lattice constant is determined ot be a $=(5.723 \pm 0.001)$ Å, which is in close agreement with reported values in thin films [16] and bulk material [95] for this Heusler compound. The existence of the order dependent $(002)_{\mathrm{A}}$ peak indicates at least the B2-ordering is present. Further analysis of these peaks intensities yields an order parameter S for the B2 structure, which is defined by [96]:

$$S = \sqrt{I_{002}^{meas}/I_{004}^{meas} \cdot I_{004}^{calc}/I_{002}^{calc}}. \tag{5.1}$$

$I_{004}^{calc}/I_{002}^{calc}$ is calculated from the structure factors by assuming B2 ordering for a $Ni_{45}Co_5Mn_{30}Al_{20}$ composition with Ni and Co occupying randomly the 8c Wyckoff sites while Mn and Al distributed randomly on the 4a and 4b sites of the $L2_1$ structure. Under these assumptions an order parameter of S $=(1.04 \pm 0.01)$ is obtained. A value greater than 1 is not possible and can arise from a slightly different chemical composition as assumed, errors in the peak fitting process or due to insufficient consideration of the instrumental broadening. Still, since a the obtained value is close enough to 1 the assumed unit cell is used for further analysis.

Texture of the sample is investigated by recording a pole figure of the fundamental $(202)_{\mathrm{A}}$ peak. The measurement is shown in Figure 5.2 a). Sharp

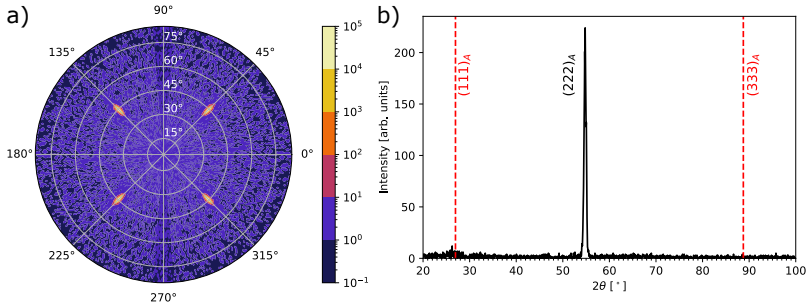

Figure 5.2: a) Texture measurement for the $(202)_A$ peak at 44.276°. b) $\theta/2\theta$-scan along the $[111]_A$ direction. Positions of the superstructure peaks for $L2_1$ ordering are marked by the red dashed lines.

diffraction peaks with a four-fold symmetry are only detected at a ψ-tilt of 45° from the $[001]_{MgO}$ direction, which is expected for a cubic structure with the above mentioned epitaxial relationship. They are furthermore located at the ϕ angles of 45°, 135°, 225° and 315°. They correspond to the $\langle 110\rangle_{MgO}$ directions. This orientation is favorable as the lowest lattice mismatches between the MgO-substrate, V seed layer and Ni-Co-Mn-Al layer are achieved if the epitaxial relationships $[110]_{MgO}$ || $[100]_V$ || $[100]_{NCMA}$ for the in plane lattice components are satisfied [16, 97].

In order to verify that the Ni-Co-Mn-Al Heusler compound is indeed B2 and not $L2_1$ ordered an additional $\theta/2\theta$-scan along the $[111]_A$ direction is performed (shown in Figure 5.2 b)). The one peak visible is identified as the fundamental $(222)_A$ at 54.783°. The expected positions of the superstructure $(111)_A$ and $(333)_A$ peaks are marked by the red dashed lines in the graph. No indications of the $(333)_A$ peak is visible in the diffraction pattern. However, at the $(111)_A$ angle a very small signal barely above the background is visible. This might indicate that a small fraction of the $L2_1$ phase is present in the Heusler compound.

Although XRD analysis suggest an epitaxial sample with a good quality and is in agreement with the literature, a number of defects present in the the film are identified in TEM investigations. For this a cross section is cut out from the sample along the $[100]_{MgO}$ direction. An overview of the specimen, recorded in scanning mode (STEM), is shown on the left side of Figure 5.3. On the right side EDX-mappings of Ni (red), Mn (green) and Co (blue) of the same area are superimposed on the STEM image to probe the chemical distribution of these elements. The first notable kind of defect present in the sample are grain boundaries, which are roughly orientated by

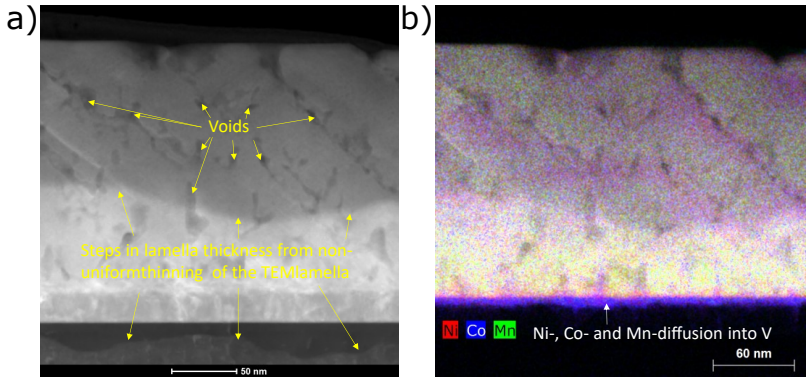

FIGURE 5.3: a) STEM overview of the reference sample. The surface of the sample is located at the top of the image. b) STEM image superimposed of EDX maps of Ni(red), Co (blue) and Mn (green) recorded for the same region.

45° to the surface normal. At these boundaries a change in the distribution of Mn atoms is visible in the EDX-mapping. While Ni and Co remains almost evenly distributed in the Heusler thin film the Mn signal at the grain boundaries is greatly reduced. It can be concluded that Mn tends to diffuse away from grain boundaries. Consequently, due to that local variations in chemical composition also local variation martensitic transformation temperature T_{MT} can be expected. Another type of defects present are indicated by the yellow arrows in Figure 5.3 a). Several dark spots are visible in STEM image of the Heusler thin film. Contrast in an TEM image can have different reasons. However, in the corresponding areas almost no EDX signal from Co, Mn and Ni is detected. Thus, these defects are either voids in the thin film or precipitates of pure Al. The cause of voids cannot be explained but Al segregation can arise if temperature during the deposition is too high such that the Heusler alloy decomposes. This is most likely the cause as also a significant amount of Mn, Co and Ni interdiffusion into the V seed layer is observed.

As a last method of characterization a SAED pattern of the Ni-Co-Mn-Al layer is recorded and simulated with the JEMS software package. Scaling inside the software was achieved by simulating a diffraction pattern for the MgO-substrate and adjust the scaling parameter until a match with an SEAD image of the substrate is achieved. For the Heusler compound the same unit cell for the XRD analysis is assumed here as well. The measurement and simulated diffraction spots for a (110) zone axis is shown in Figure

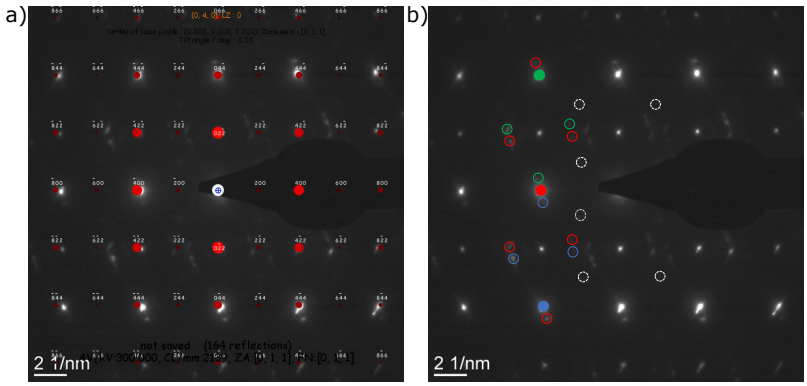

Figure 5.4: Selected area electron diffraction image of the reference Ni-Co-Mn-Al layer along the $(100)_{MgO}$ zone axis. In a) the calculated diffraction peaks and their hkl indices for the B2 ordered structure by the JEMS software package are shown as red points. In b) unidentified spots are marked by the open circles. Open circles might be satellite peaks of the full-color reflections.

5.4 a). All of the main diffraction spots are well reproduced by the simulation, which confirms that the average ordering present in the Heusler layer is B2. But also some smaller spots with lower intensity are visible that are not explained by the simulation. Some of them are marked by open circles in Figure 5.4 b). These additional diffraction spots have not yet been clearly identified. One possible assumption is that the colored outlined reflections are satellite peaks of the full-color reflections due to modulations. Since the possibility of small precipitates present in the sample could not be entirely excluded they might also be the cause for those minor diffraction spots. Similar to the XRD pattern, diffraction spots with very small intensity are barely visible at the $L2_1$ superstructure positions $\{111\}$ and $\{133\}$, which are marked by the open white dashed circles. It is found that those signals are most pronounced if the interface region of the V seed layer is included. It can be therefore assumed that the interdiffusion of Ni, Co, Mn and possibly Al atoms forms with the V atoms another Heusler compound (e.g. Mn_2VAl [98, 99]). If the lattice constant is similar to that of the Ni-Co-Mn-Al system these new Heusler cells would integrate into the multilayer system with the same epitaxial relationships. The low intensity of the diffraction spots suggest that only a very small portion of the sample is in the undesired $L2_1$ phase and thus can be ignored in the further analysis.

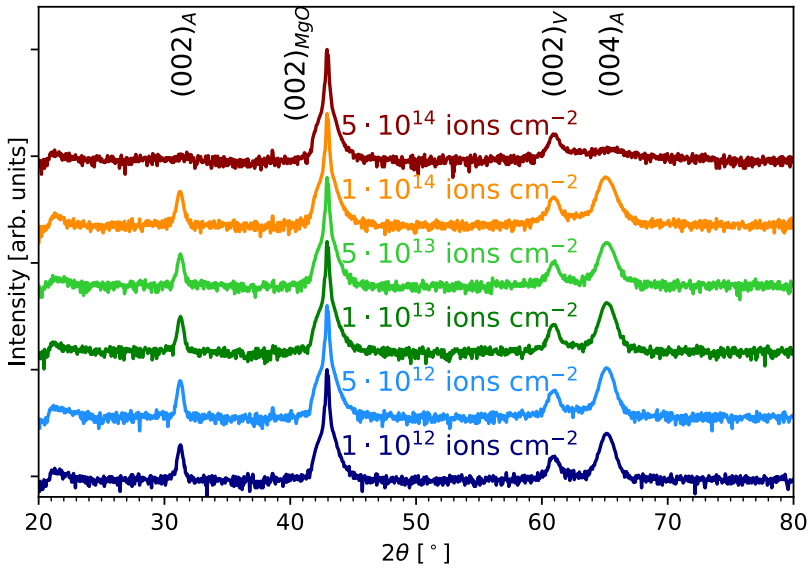

FIGURE 5.5: $\theta/2\theta$-measurements for all irradiated samples. Datasets are offset to each other for better visibility.

5.4 Irradiation results

The impact of the irradiation on the samples crystal structure is first investigated by XRD. For all irradiated samples a $\theta/2\theta$-scan in the range from 20° to 80° is recorded, which are shown in Figure 5.5. Offsets for the diffraction patterns are used for the purpose of better visibility. Up to an ion fluence of 1×10^{14} ions/cm^2 barely any difference to the reference pattern is visible. The absence of additional peaks from other phases attests the low damage induced by the ion bombardment. Only above an ion fluence of 5×10^{14} ions/cm^2 significant changes in the crystal structure become apparent. Not only does the $(002)_A$ peak vanish but the fundamental $(004)_A$ peak as well indicating that the concentration of generated defects is sufficient enough to prevent coherent scattering of x-rays to occur. Noteworthy is that the $(002)_V$ peak remains rather unaffected in this sample.

The out-of-plane lattice parameter, calculated from the $(004)_A$ peak and the B2 order parameter S, as defined in the section above, can be used to visualize the slight changes in the crystal structure caused by the ion beam irradiation. Calculated values for both of them in dependence of the ion fluence are shown in Figure 5.6 a) and b) respectively. Other studies found

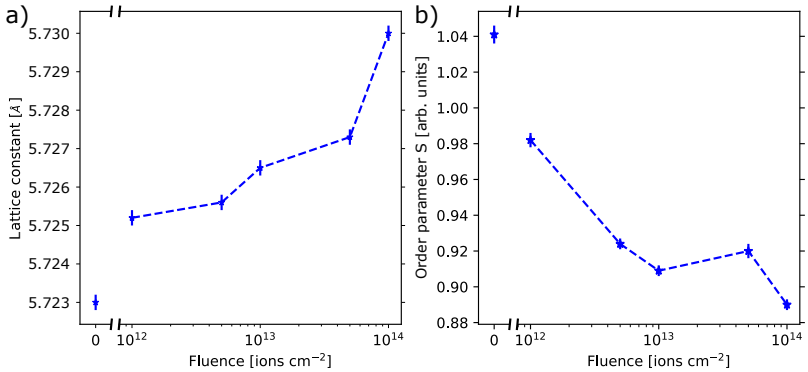

Figure 5.6: a) Austenite lattice constant calculated from the $(004)_A$ peak in dependence of the ion fluence. b) Order parameter S for the B2 structure in dependence of the ion fluence according to Equation 5.1. Dashes lines serve only as a guide for the eye.

that induced disorder by ion beam irradiation enlarges the unit cell [93, 100] thus, an increase in the mean lattice constant is expected. Indeed, a monotonic increase in the lattice constant from 5.723 Å to 5.730 Å is calculated from the $(004)_A$ peak, which corresponds to an relative expanse of 0.12 % on average. Accordingly the order parameter for B2 structure decreases with increasing fluence further confirming the induced structural damage of the crystal lattice.

For the characterization of the martensitic transformation temperature dependent magnetization measurements for heating and cooling in the range from 50 K to 350 K at external fields of 1 T and 2 T were performed for the reference sample and the four highest ion fluences. Magnetization data from a pure MgO-substrate are subtracted from the obtained curves to exclude the diamagnetic background. The final thermal hysteresis curves for all samples are shown in Figure 5.7 a) and b).

The reference sample (blue curve) shows a clear thermal hysteresis from the MT between 100 K to 225 K. The transition region for cooling and heating cover rather large temperature ranges of several tens of kelvin respectively and displays a nonlinear behavior. This is probably due to the large number of initial defects and the inhomogeneous distribution of the elements present in the sample. Furthermore, the magnetization at very low temperatures remains quite large despite the martensite having a rather weak magnetic state in the Ni-Co-Mn-Al system. This points to a large residual austenite present in the sample after MT. Unfortunately, the exact amount

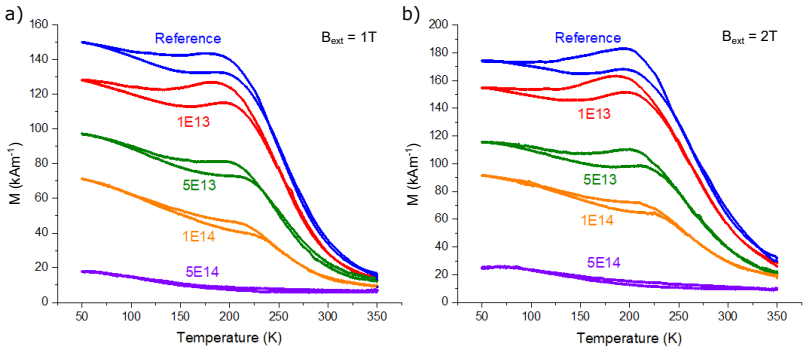

FIGURE 5.7: Magnetization in dependence of temperature for heating and cooling in an external magnetic field of a) 1 T and b) 2 T of the irradiated samples.

could not be determined from temperature dependent XRD measurements as the accessible temperature range of the custom build cryostat is not sufficient to cover the whole transition region. The Curie temperature T_c for the reference sample is below room temperature, which is in accordance with literature values for Co contents around 5 % [14, 48, 50].

The effects of point defects by ion beam irritation become apparent in the temperature dependent magnetization curves of the 1×10^{13} ions/cm^2, 5×10^{13} ions/cm^2, 1×10^{14} ions/cm^2 and 5×10^{14} ions/cm^2 samples. Notably, the magnetization diminishes upon increasing the ion fluence while the thermal hysteresis of the MT becomes less pronounced. No MT is measured anymore for the highest ion fluence of 5×10^{14} ions/cm^2, which can be expected from the large radiation damage in the crystal structure indicated by XRD.

For the other fluences a steady shift in the hysteresis towards higher temperatures with increasing fluence is observed. The shift can be better seen in the transition temperatures T_M (blue) and T_A (red) in Figure 5.8 a) and b) for both external magnetic fields. They are defined as the inflection points of the hysteresis curves and are obtained by taking the numerical derivative of the cooling and heating branch respectively. For a ion fluence of 1×10^{14} ions/cm^2 a maximum increase of about 35 K for T_M and T_A to the unirrdiated sample is measured at 1 T. At 1 T the shift in both temperatures is slightly lower 29.1 K and 31.2 K respectively. Surprisingly, the hysteresis width $\Delta T = T_A - T_M$, shown in Figure 5.8 c), remains rather unaffected by the concentration of defects in this sample. For the reference

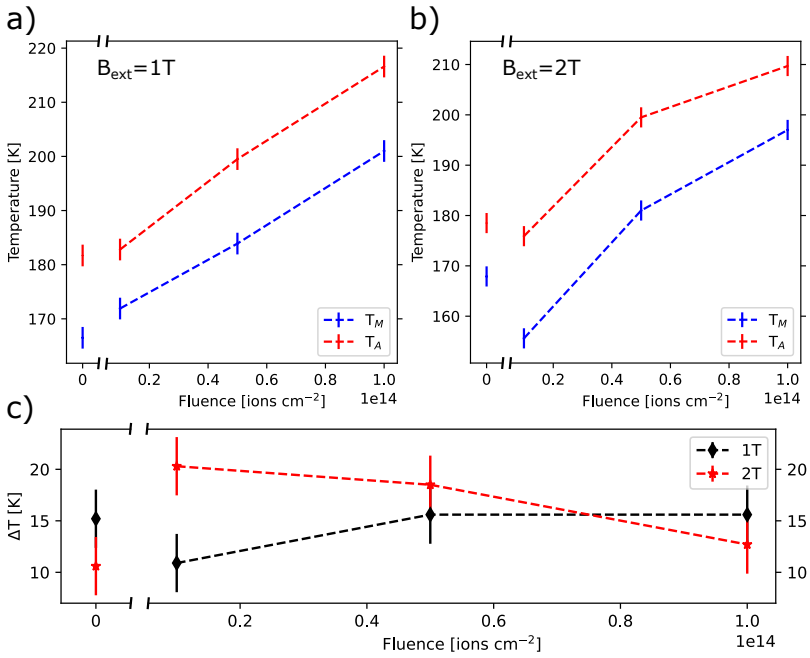

Figure 5.8: Transition temperatures T_M (blue data points) and T_A (red data points) in dependence of the ion fluence for an external magnetic field of a) 1 T and b) 2 T. The data points were determined form the M(T)-curves in Figure 5.7. In c) the hysteresis width, defined as the difference of T_M and T_A is shown. Dashed lines only serve as a guide for the eye.

and the irradiated samples an almost constant hysteresis width of about 15 K is determined at an external field of 1 T.

Interpretation of the obtained results remains difficult as many underlying principles of the impact of structural disorder on the martensitic transformation in NiMn-based MSMA's are not understood so far. The situation is difficult to model, because many different types of structural defects can be created in the collision cascade. They can range from slight displacements of the atoms from their respective lattice positions to intrinsic interstitial atoms, extrinsic interstitial atoms (e.g. trapped Ne^+-ions) or vacancies [92, 101, 102]. Even clusters of the mentioned point defects can occur. Each of them will affect the MT, either by induced strain fields in their surroundings or by altering the exchange coupling between neighboring magnetic moments.

The irradiation damage in the crystal can roughly be divided into two regimes. Below a critical fluence the damage can be treated as disorder without a change in the lattice on average, while above the critical fluence it is more appropriate to treat the damage as a change of the crystal lattice to a less symmetric structure. Our XRD results suggests that the critical fluence is between 1×10^{14} ions/cm^2 to 1×10^{15} ions/cm^2.

In order to get a qualitative insight about the influence of structural disorder on the magnetism and MT we take a look at the different in nature yet related chemical disorder in Ni-Co-Mn-Al. A change in chemical disorder is believed to be the reason for evolution in magnetization, entropy change and cell volume observed during different annealing times in melt-spun ribbons [96]. Very short annealing times lead to a transformation of A2 to the desired B2 phase, which is accompanied by a sharp increase in magnetization and entropy change during MT. Upon longer annealing times a further improvement of the magnetization and entropy change is observed at first. Both quantities however decrease if the samples are annealed any further although almost no change in B2 ordering is detected by XRD. During annealing time a shift of approximately 31 K for the MT towards higher temperatures is observed as well.

The high sensitivity of the properties of Ni-Co-Mn-Al Heusler compounds for chemical disorder is further confirmed by ab-initio calculations. Studied were the impact on Co substitution in $Ni_{50-x}Co_xMn_{31.25}Al_{18.75}$ [6, 45] and the impact of the distribution of Mn atoms on the Mn and Al sublattice of two non-equivalent B2-cells in $Ni_{43.75}Co_{6.25}Mn_{31.25}Al_{18.75}$ [96]. The most important results obtained from these calculations are:

- Nearest neighbor interaction of host Mn and anti-site Mn moments on the Al sublattice is antiferromagnetic regardless of their respective positions in $Ni_{50}Mn_{31.25}Al_{18.75}$.
- Substitution of Ni by Co favors a parallel alignment of all nearest neighbor moments in the austenite state.
- Chemical disorder in non-equivalent B2 configurations affect the internal energy and volume of the austenite unit cell.
- A ferromagnetic or antiferromagnetic alignment of the magnetic ground state in the austenite phase is determined by chemical disorder.

Impacts on magnetization and electronic structure were also demonstrated by ab-initio calculations in Ni-Co-Mn-Ga [103] and similar results obtained in Ni-Mn-based MSMA's annealing studies [104–106] further highlights the sensitivity of chemical disorder in these systems. Based on

this it can be assumed, that the properties of Ni-Co-Mn-Al is similar sensitive to structural disorder. The ab-initio results might also explain the reduced magnetization measured in our irradiated samples. If Co atoms are displaced from the unit cell during the collision cascade the strong ferromagnetic exchange between the neighboring magnetic moments will be lost in the austenite state. As a result the magnetization would decrease. Similarly, the ion beam irradiation would increase in Mn anti-site defects, which are likely to couple antiferromagnetically to the neighboring Mn moments. However, comparisons to chemical disorder cannot predict if a particular point defect in a damaged cell will still show a martensitic transformation. The less pronounced MT present in the M(T)-curves suggests that this is not the case. Still, they can serve as nucleation sites for the martensite, which lower the energy barrier and thus results in a shift in transformation temperatures as less undercooling is needed.

Interestingly the Heusler compound system behaves opposite to comparable studies on performed on FeRh. FeRh, as one of the most promising magnetocaloric materials, shows a first-order isostructural metamagnetic transition from a cubic ferromagnetic at high temperatures to a cubic antiferromagnetic state at low temperatures. In contrast to our Heusler compound irradiated FeRh thin film samples show a shift of the MT towards lower temperatures [93, 94]. Furthermore, with increasing ion fluence a stabilization of the ferromagnetic ordering is observed at low temperatures. Eggert et al. [94] attribute this to a second magnetic phase with an identical hyperfine field splitting to the B2-FeRh phase evolving due to ion beam irradiation. In these thin film studies the thermal hysteresis also broadens significantly and displays a nonlinear behavior with increasing ion fluence [93, 94]. This is in accordance with the findings of Malygin [43]. Equation 2.16 predicts a broadening of the transition region $\Delta\tau$ proportionally to the defect concentration C in the sample. For point like defects the broadening should also be especially pronounced since $\Delta\tau$ is inversely proportional to r^3, where r is the radius of the obstacle. This increase is not visible in our samples. This might be masked due to the initial broad martensitic transition in the sample.

Another very important aspect about the impact of ion beam irradiation on the MT, which should be considered for applications, are the resulting thermodynamic properties. The entropy change during the phase transition is particular important in the context of magnetocaloric refrigeration. Their ability to refrigerate is directly linked to the difference in magnetization and the amount of volume participating in the martensitic transformation. Cervera et al. [93] could measure a drop in cooling capacity by a factor of 2 for an FeRh sample irradiated with a fluence of 1.7×10^{13} ions/cm^2. Because the magnetization difference and the volume of transformed material

is significantly reduced in our samples by irradiation a decrease in cooling capacity can be expected in our samples as well. Although the transition temperature can be tuned by ion beam irradiation the worsening of the magnetic and thermodynamic properties in MSMA's can limit this post-processing method in applications.

5.5 Conclusion

$Ni_{45}Co_5Mn_{30}Al_{20}$ thin films were prepared and irradiated with 150 keV Ne^+ ions at different ion fluences to investigate the effects of point like defects on the martensitic transformation in this system. We found that with increasing concentration of defects the martensitic transformation shifts to higher temperatures, which can be interpreted as an average decrease in the nucleation barrier. This comes with the disadvantage of less material being transformed and deterioration of the magnetic properties in this system. These might have direct impact on the desired properties such as cooling capacity. A reduction in hysteresis width is not observed in the prepared samples. A possible influence might be overshadowed by the already present number of defects present in the sample during sample preparation, which resulted in a very broad transition region. Therefore to further verify the obtained results the experiment should be repeated after improved deposition conditions. Nonetheless, the ion beam irradiation offers a new degree of freedom to tailor NiMn-based MSMA's to the desired needs.

Martensitic intercalations in Ni-Co-Mn-Al shape memory alloys 6

6.1 Introduction

Existing studies showed that thermal hysteresis can be minimized by either optimizing the chemical composition of the material system of interest [107], applying hydrostatic pressure to enhance the phase compatibility between martensite and austenite [108] or nanoindentation [91]. Another recently investigated option is just cycling through minor loops of the thermal hysteresis [26, 41]. The latter method is based on the idea that the reverse MT is stopped before the full austenite state is reached. Thus the nucleation step is avoided as martensite nuclei are always present in the minor loop cycle. A physically very similar concept followed in this work is the use of martensitic intercalations in thin film stacks, presented in this chapter. Two material systems, an active transforming layer (AL) with a MT below a working temperature and a martensitic intercalation (MI) with a transition temperature well above the working temperature, are put together in a multilayer like fashion. As in the case for the minor loop concept martensite is always present, which serves as nuclei while the AL undergoes thermal hysteresis.

As stated in Chapter 2.5 in Mn-rich $Ni_{50-x}Co_xMn_{25+y}Al_{25-y}$, which undergoes a cubic-to-tetragonal transition, the MT temperature can be shifted by slightly varying the Al or Co content[14, 48]. This offers the advantage that the whole intercalation system can be constructed with the same material system. In addition, the highly geometrical, controlled distribution of martensite cores due to the layer stacking could be advantageous for the transformation behavior. Moreover, in contrast to the simple minor loop concept the full transformation cycle of the AL can be utilized. Little is yet known about the transformation behavior of such martensitic intercalated systems. Therefore we investigate these effects in sputter deposited epitaxial thin film multilayer systems and characterize the MT in terms of hysteresis width, transformation temperature and residual austenite.

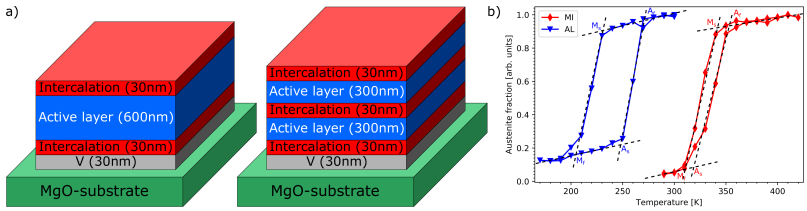

Figure 6.1: a) Illustration of the 2 MI and 3 MI sample systems. All sample systems are capped with 2 nm Ru to prevent oxidation, which is not shown here. b) Visualization of the austenite fraction in dependence of temperature for the MI (red) and AL (blue) compositions calculated from temperature dependent XRD measurements.

6.2 Experimental details

6.2.1 Sample preparation and characterization methods

Thin film Ni-Co-Mn-Al multilayer systems were prepared in a magnetron co-sputter deposition chamber from 3" pure elemental Ni (DC), Mn (DC). Al (DC), Co (RF) targets with a base pressure better than 5×10^{-9} mbar and a target to substrate distance of 21 mm. MgO(001) is used as the substrate material and is heated up in the deposition chamber to 450 °C prior to the deposition of the thin films. In earlier studies we found that a less rigid seed layer than MgO improves the martensitic transformation in thin films [90] and therefore a 30 nm V seed layer is deposited before any of the Heusler films. In order to minimize diffusion effects between the active layers and martensitic intercalations the sample was immediately cooled down to room temperature after the deposition of the Heusler layer. Furthermore all samples are capped with a 2 nm thick Ru layer to prevent oxidation.

Sample systems were prepared with 0, 2, 3, 4, 7 and 13 MI's. Every intercalation layer has a thickness of 30 nm. The total thickness of the active layers was always held constant at 600 nm and divided into equally thick parts in order to have a constant amount of AL volume throughout the sample series. Thus, the thickness t_{AL} of one AL in the sample systems can be calculated by $t_{AL} = |\frac{600\ \mathrm{nm}}{N_{\mathrm{MI}}-1}|$, with N_{MI} being the number of martensitic intercalations. An illustration of the 2 MI and 3 MI sample systems are shown in Figure 6.1 a).

Structural investigations were carried out in a Philips X'pert MPD x-ray diffractometer in Bragg-Brentano geometry using Cu K_α radiation. A custom build LN_2 cryostat with a temperature range from 140 K to 470 K was utilized in order to investigate the crystallography in dependence of temper-

Table 6.1: Martensite start M_s, martensite finish M_f, austenite start A_s and austenite finish A_f temperatures for the AL and MI thermal hysteresis shown in Figure 6.1 b).

Layer	M_s [K]	M_f [K]	A_s [K]	A_f [K]
AL	232	204	248	271
MI	342	310	319	353

ature. The austenite fraction at a specific temperature was determined by fitting the (004) austenite peak of the Heusler compound with a Pseudo-Voigt function and measuring the area under the curve. The data is then normalized to the measured intensity in the fully austenitic state.

Temperature dependent magnetization measurements in the range from 100 K to 320 K were performed in a 7 T vibrating sample magnetometer (VSM) with an in-plane applied external magnetic field of 500 mT.

High resolution images and selected area electron diffraction (SAED) were recorded in a JEOL FS-2200 transmission electron microscope (TEM). The local micro-structure in the samples is determined by fast-Fourier transformation (FFT) analysis of the images. Furthermore diffusion effects are investigated by energy dispersive x-ray spectroscopy (EDX) mapping of the samples cross section.

For convenience reasons, room temperature (RT) was chosen as the working point for this study. Before the preparation of the intercalation samples, a composition with a MT below and a composition above RT have to be found. For this 200 nm thick Ni-Co-Mn-Al films with different compositions were deposited and their transition temperatures were measured by temperature dependent XRD measurements. Thin films with nominal compositions $Ni_{43}Co_7Mn_{31}Al_{19}$ for the AL's and $Ni_{47}Co_3Mn_{33}Al_{17}$ for the MI's were found to be suitable. The nominal compositions were derived from the individual deposition rates of each target. Their respective thermal hysteresis is depicted in Figure 6.1 b). The AL (blue triangles) composition shows a very broad hysteresis between 200-250 K while the MI (red diamonds) exhibit a very small hysteresis between 320-340 K. Both transitions are completed at RT and therefore their martensitic transitions do not overlap. Tab. 6.1 lists the values for the transformation temperatures as indicated in the figure.

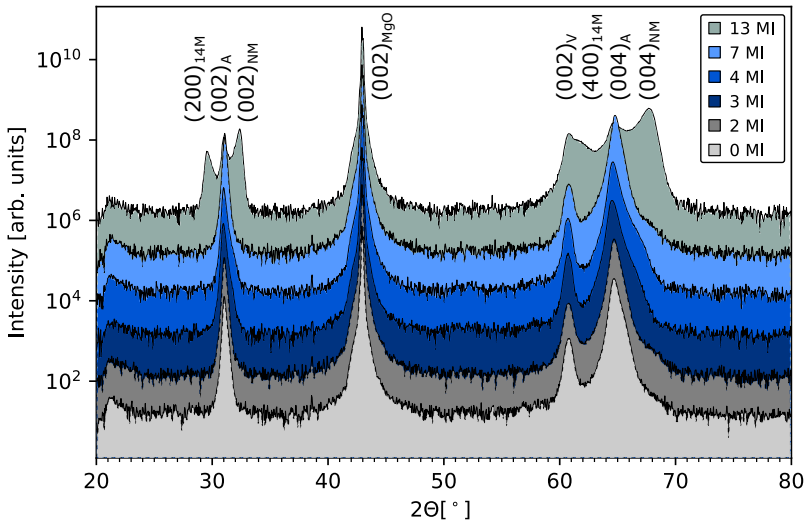

Figure 6.2: $\theta/2\theta$-measurements at room temperature for the sample series.

6.2.2 Structural Characterization and Temperature Profile of the Martensitic Transformation

From both compositions the intercalations samples were fabricated. Figure 6.2 shows the $\theta/2\theta$-scans used to determine the structural properties of all investigated samples. The $(002)_{MgO}$ peak at 42.91°, the $(002)_V$ peak at 60.73° are clearly visible in all scans as well as the diffraction peaks (002) 30.97° and (004) at 64.54° associated with the austenite phase. The austenite can be described in Ni-Co-Mn-Al as a cubic B2-structure with a lattice constant of $a = 5.771$. Martensite features from the intercalations are only present in the 13 MI sample. At 32.36° the $(200)_{NM}$ and at 67.68° the $(400)_{NM}$ peak are visible from the nonmodulated martensite unit cell. Furthermore to the left of both austenite peaks there is also a diffraction peak visible which could be attributed to the 14M modulation of the martensite, which frequently occurs in this alloy to reduce the interfacial energy between the martensite and austenite [16, 109]. The lattice parameters were found to be $a = 5.53$ and $c = 6.62$.

Characterization of the martensitic transformation was performed by temperature dependent magnetization measurements in the range from 100-320 K with an external in-plane magnetic field of 500 mT, which are shown in Figure 6.3. Transformation behavior differs widely between the 4, 7 and 13 MI samples on one and the 0, 2 and 3 MI samples on the other side.

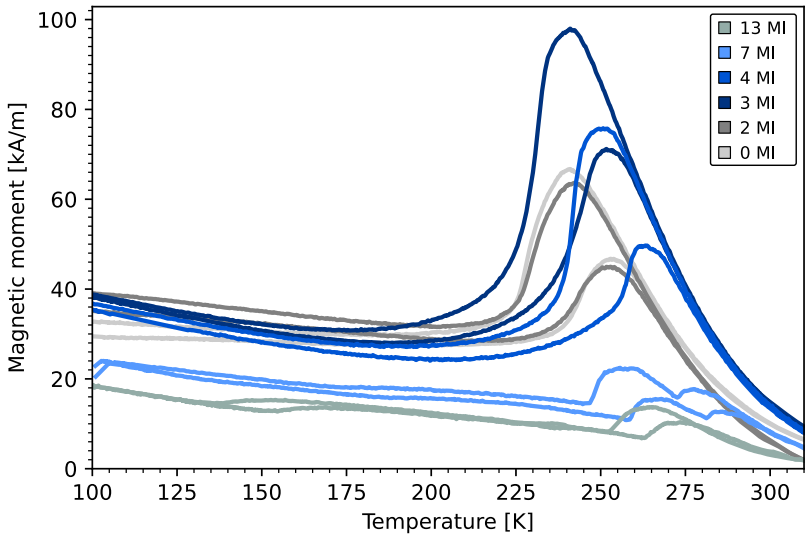

FIGURE 6.3: Magnetic moment in dependence of the temperature. External magnetic field of 500 mT applied in-plane.

Starting with the first three samples of the series we find a sharp martensitic transformation occurring around 230 K.

Figure 6.4 a) and b) show the values for the martensitic transformation temperature T_M and reverse transformation temperature T_A alongside the hysteresis width $\Delta T = T_A - T_M$. These Temperatures are defined by the inflection points of the cooling and heating branch respectively. With increasing number of intercalations we find a steady decrease in hysteresis width from 16.9 K to 13.8 K. Looking at the transformation temperatures we find that T_M remains constant at 278 K while T_A shifts to higher temperatures. In this regard the martensitic intercalations behave similar to as the minor-loops in Ni-Mn-Ga thin films [41].

Figure 6.4 c) shows the amount of residual austenite at low temperatures, which is another important quantity to characterize martensitic transformations. The data points are calculated from XRD measurements of the $(004)_A$ peak at 140 K normalized to measurements at room temperature, which are shown in Figure 6.5. In contrast to the decrease in hysteresis width, we find a steady increase in residual austenite from 2.5% to almost 20% for the 3 MI sample in this case. In thin film systems it was shown that the martensite nuclei take the shape of flat, elongated diamonds with their phase boundary inclined by a few degrees from the $\{011\}_A$ planes, which

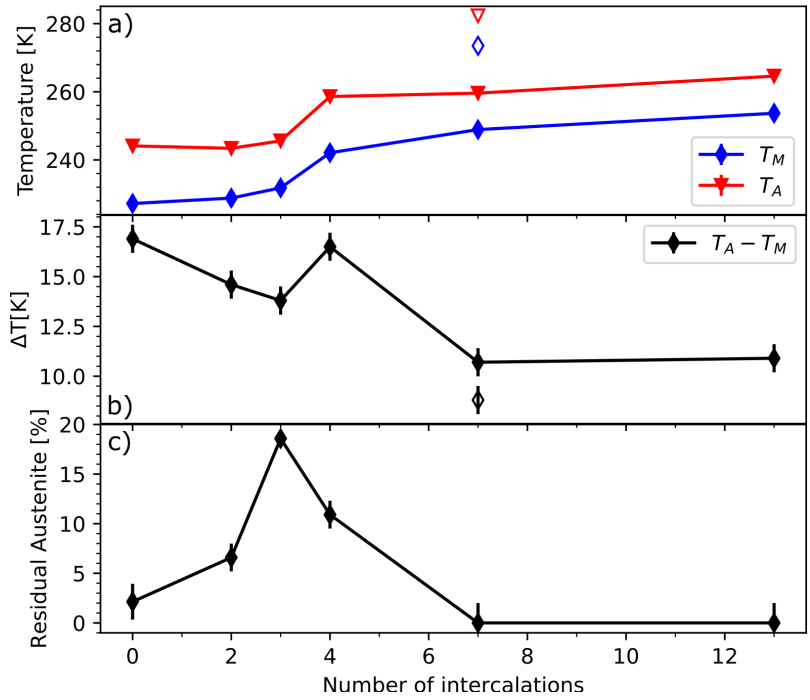

Figure 6.4: a) Transition temperatures, b) hysteresis width and c) residual austenite content in dependence of the number of martensitic intercalations. The open symbols are the values for the second hysteresis in the 7 MI sample.

mainly grow in length not in width during martensitic transformation[35]. The nuclei stop to grow if the tip of the diamonds touch other phases, such as substrates or other martensite nuclei, because an energetically unfavorable incoherent interface has to be formed. Thus, in thin films the thickness of the film dictates the maximum size of a martensitic nucleus[6]. As the thicknesses of the AL's become smaller with increasing number of intercalations the maximum size of the martensite nuclei are reduced as well, leaving a lot of untransformed material in between the nuclei. In this regard the MI's can be viewed as barriers for the growth of the martensite. At the moment it is unclear if the martensite nuclei in the MI layers simply grow during cooling and protruding inside the AL layers or if different martensitic nuclei begin to grow inside the active layers, which is facilitated by local strain fields of the MI layers.

The situation drastically changes for the 4, 7, and 13 MI sample systems

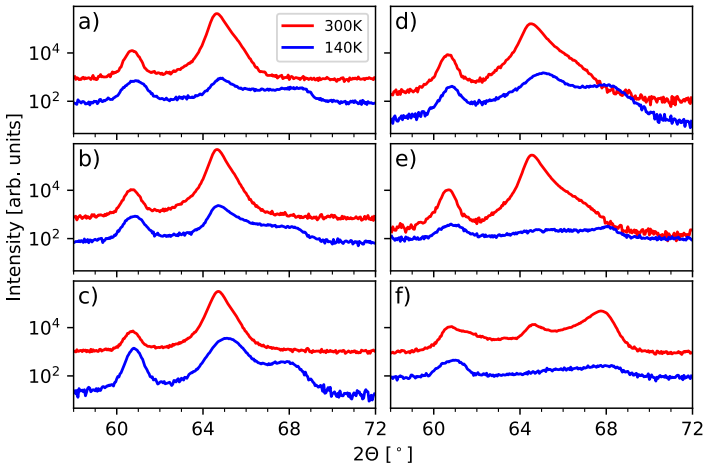

FIGURE 6.5: $\theta/2\theta$-scans in the range 58° to 72° at 300 K (red graph) and 140 K (blue graph) for the a) 0 MI, b) 2 MI, c) 3 MI, d) 4 MI, e) 7 MI and f) 13 MI samples.

in which the thicknesses of the AL's approaches the thickness of the MI's. A sudden shift in the MT towards RT is noticeable. In the 7 and 13 MI samples, a splitting of the hysteresis in multiple ones is observed, indicating the presence of regions with different transformation behavior. Still, hysteresis width reduces further to 10.7 K except for the 4 MI sample,. The residual austenite content at low temperatures decreases and remarkably for the 7 and 13 MI samples, no intensity from the $(004)_A$ peak could be distinguished from the background. Thus, in these two samples the amount of residual austenite can be neglected.

6.2.3 Interdiffusion across the interfaces

Since the deposition of the samples takes place at elevated temperatures, diffusion has to be taken into account. Especially the light elements Al and Mn tend to diffuse easily. In order to estimate this effect, a 30 nm thick sample was deposited with the same composition of the AL's at the same deposition temperature. To get a high difference in chemical composition the power at Mn source is instantly halved and at the same time the power of the Al source doubled after half of the deposition time. The sample stays heated the same amount of time as the 13 MI sample. Thus the sample

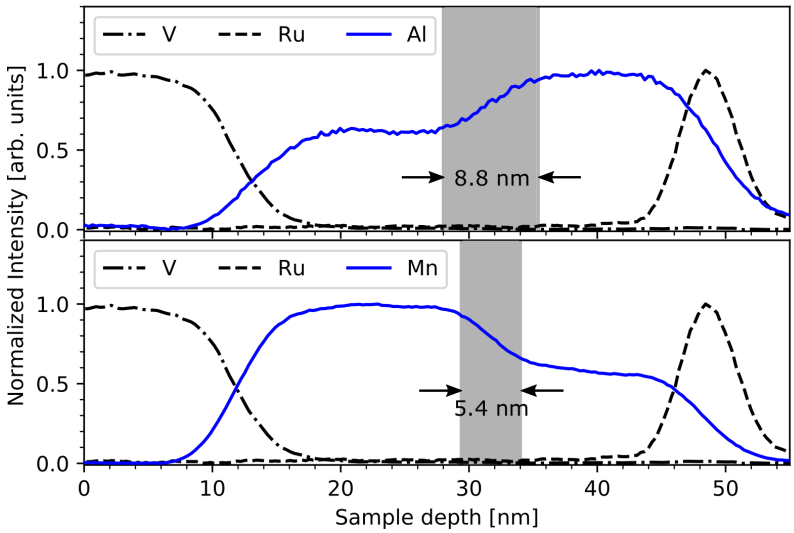

Figure 6.6: Normalized concentration line profile of the test sample for Al (upper panel) and Mn (lower panel) calculated from the EDX-mapping.

should be representative for the bottom most AL/MI-interface in the 13 MI sample as well as serve as a worst case scenario for all other interfaces. A line profile is calculated from EDX-mapping of a cross section. Diffusion between the AL's and MI's can be ruled out as the reason for the shift in transformation temperatures. From the normalized line profiles shown in Figure 6.6 we find that only a region of about 9 nm for Al and 5.5 nm for Mn around the interface is affected in the worst case. Thus most of the inner parts of all layers should be chemically intact.

Instead, we find evidence that elastic coupling between the different layers rearranges the martensite nuclei and guides their growth during cooling. In the 13 MI sample this leads to a very inserting long range ordering phenomenon as can be seen from cross sections cut along the $[100]_A$ direction in TEM. Figure 6.7 shows two of these images. Over the entire area of the Heusler thin film checker board like arrangement of brighter and darker regions are seen. From FFT analysis of high resolution TEM (HRTEM) images we could determine that the contrast results from martensite and austenite regions. The existence of Moiré-pattern in all cells, which could arise from overlaps of martensite and austenite lattices suggests that this ordering also extends in the third dimension as well. A detailed analysis of this checker board will follow in the next chapter. Such a structure raises inter-

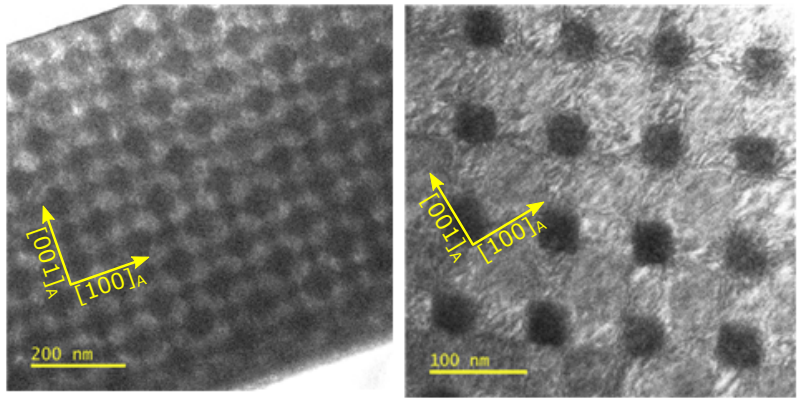

FIGURE 6.7: TEM images of an cross section from the 13 MI sample. The phase contrast stems from different crystal structures inside the sample.

est because complex magnetic structures might emerge due to the periodic arrangement of ferromagnetic and non-ferromagnetic areas.

6.3 Conclusion

Hysteresis and transformation behavior were studied in epitaxial Ni-Co-Mn-Al magnetic shape memory alloy thin films with varying number martensitic intercalations (MI's) placed in between. MI's consists of a different Ni-Co-Mn-Al composition with a martensitic transformation occurring at much higher temperature than the host composition. With increasing number of intercalations, we find a decrease in hysteresis width from 17 K to 10 K. For a large difference in the layers thicknesses, this is accompanied by a larger amount of residual austenite. If thicknesses become comparable, strain coupling between them dominates the transformation process. This manifests in a shift of the hysteresis to higher temperatures, a splitting of the hysteresis in sub hysteresis and a decrease in residual austenite to almost 0 %. A long-range ordering of martensite and austenite regions in the shape of a 3D checker board pattern is formed at almost equal thicknesses.

3D checkerboard 7

In this chapter the origin and behavior of the checkerboard sample are discussed. First the XRD data are presented as they allow the determination of the lattice parameters and the general orientation of the martensite and austenite unit cells. In the second part these results are then correlated with the data obtained from TEM experiments. The TEM data in this chapter was produced by Daniela Ramermann and was kindly made available for this chapter. For further TEM-analysis the reader is referred to her PhD thesis [110].

7.1 XRD analysis

In a first step, XRD analysis is performed on the sample. From this the cell parameters for the martensite and austenite as well their respective orientations to the MgO-substrate can be measured. A $\theta/2\theta$-scan for the $(002)_M$ peak and the $(004)_A$ and $(400)_M$ peaks are shown in Figure 7.1. The peaks are fitted by Pseudo-Voigt-functions as described in 3.2.1. A linear function is subtracted to account for the background noise.

A fit for the $(004)_A$ peak yields a 2θ-angle of $(64.721 \pm 0.009)^\circ$, from which according to Equation 3.4 a lattice constant of (5.761 ± 0.008) Å for the austenite unit cell is calculated. As for the martensite a position of

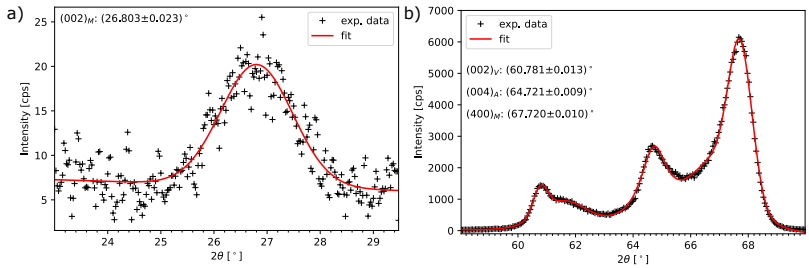

FIGURE 7.1: $\theta/2\theta$-scan for the a) $(002)_M$ peak and b) $(004)_A$ and $(400)_M$ peak and their respective fits.

$(67.720 \pm 0.010)^\circ$ for the $(002)_M$ peak and a position of $(26.803 \pm 0.023)^\circ$ for the $(400)_M$ peak is determined. Therefore, the unit cell parameters of the tetragonal cell are a =(5.534 ± 0.010) Å and c =(6.652 ± 0.018) Å. These values are in close agreement with lattice constants found in other studies for this alloy [16]. A tetragonality factor c_T for the martensite of (1.202 ± 0.003) is found for this case. In order for the $(004)_A$ and $(400)_M$ fit to converge the $(002)_V$ peak from the V seed layer at $(60.781 \pm 0.013)^\circ$ has to be considered as well in the fitting process. Additionally two more Pseudo-Voigt functions have to be introduced centered at $(61.593 \pm 0.186)^\circ$ and $(66.775 \pm 0.169)^\circ$ for the fit to converge. Both peaks could be caused by the 14M-modulated superstructure occurring in this Heusler compound.

In order to get the orientation of these cells, texture measurements at selected austenite and martensite diffraction peaks have been performed. The pole figures for the austenite $(004)_\mathrm{A}$, $(202)_\mathrm{A}$ and $(602)_\mathrm{A}$ peaks are shown in Figure 7.2 a)-c) on the left column. The austenite peaks are located close to the positions with a 4-fold symmetry, which follow from the epitaxial relationships: $[001]_\mathrm{A}$ || $[001]_\mathrm{MgO}$, $[100]_\mathrm{A}$ || $[110]_\mathrm{MgO}$. On closer inspection there is a slight tilt observed of about $(2 \pm 1)^\circ$ in either ϕ or ψ for all peaks. This can be explained by assuming four different austenite orientations present in the sample, whose orientations are given by the following matrices A_1, A_2, A_3 and A_4 (all entries are given in Å). As usually defined in crystallographic theory the columns of the matrices are the a, b, c-vectors of the crystal structure.

$$A_1 = \begin{pmatrix} 4.071 & 4.071 & 0.201 \\ -4.074 & 4.074 & 0.0 \\ -0.142 & -0.142 & 5.757 \end{pmatrix}, \quad A_2 = \begin{pmatrix} 4.071 & 4.071 & -0.201 \\ -4.074 & 4.074 & 0.0 \\ 0.142 & 0.142 & 5.757 \end{pmatrix}$$

$$A_3 = \begin{pmatrix} -4.071 & 4.071 & 0.201 \\ -4.074 & -4.074 & -0.0 \\ 0.142 & -0.142 & 5.757 \end{pmatrix}, \quad A_4 = \begin{pmatrix} -4.071 & 4.071 & -0.201 \\ -4.074 & -4.074 & 0.0 \\ -0.142 & 0.142 & 5.757 \end{pmatrix}$$

Using these orientation matrices any arbitrary reciprocal lattice position in a pole figure can be obtained by transforming the reciprocal lattice coordinates into spherical coordinates and plotting their polar and azimuthal angles. This is shown on the right column in Figure 7.2 for the respective (004), (202) and (602) peaks. Each color represents the diffraction peaks for a different orientation (blue for A_1, red for A_2, green for A_3 and black for A_4). It can be seen that all of the pole figures can be reproduced well by those four austenite orientations. However a tilt between the residual

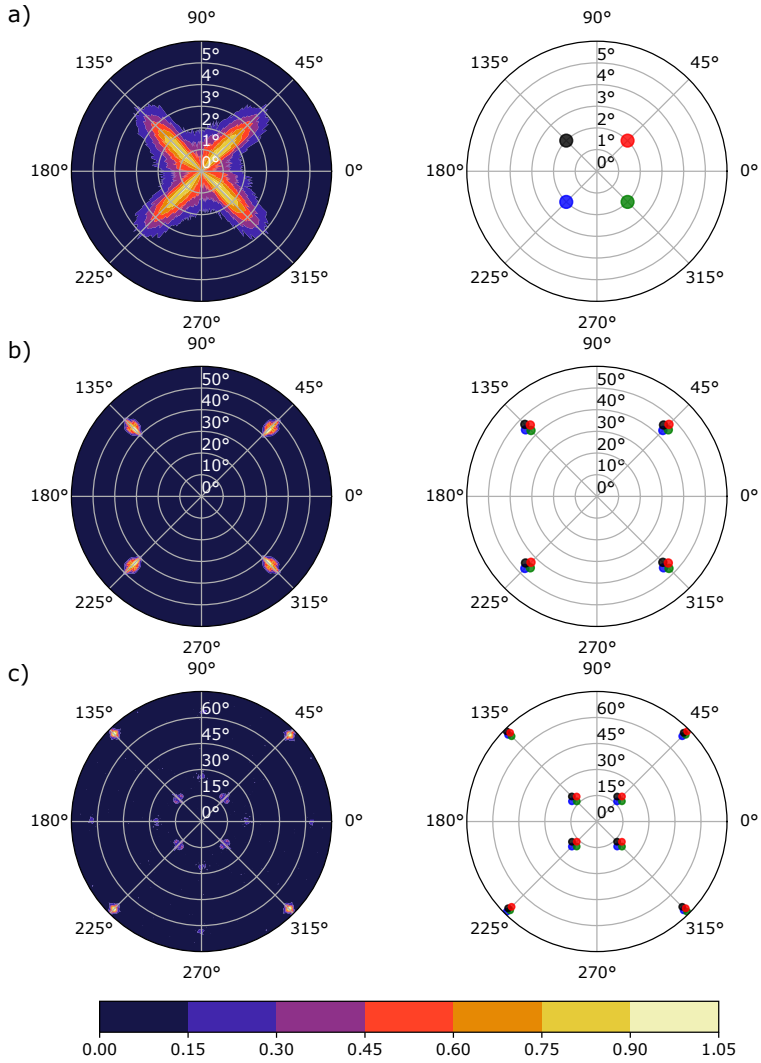

FIGURE 7.2: Pole figures for the a) $(004)_A$ peak at $2\theta = 64.7°$, b) $(202)_A$ peak at $2\theta = 44.33°$ and c) $(602)_A$ peak at $2\theta = 113.58°$. On the right side the measurements are shown and on the left side the corresponding calculation of the peak positions for the crystal orientations given by the orientation matrices A_1, A_2, A_3 and A_4. The measurements are normalized to the maximum intensity in the pole figure.

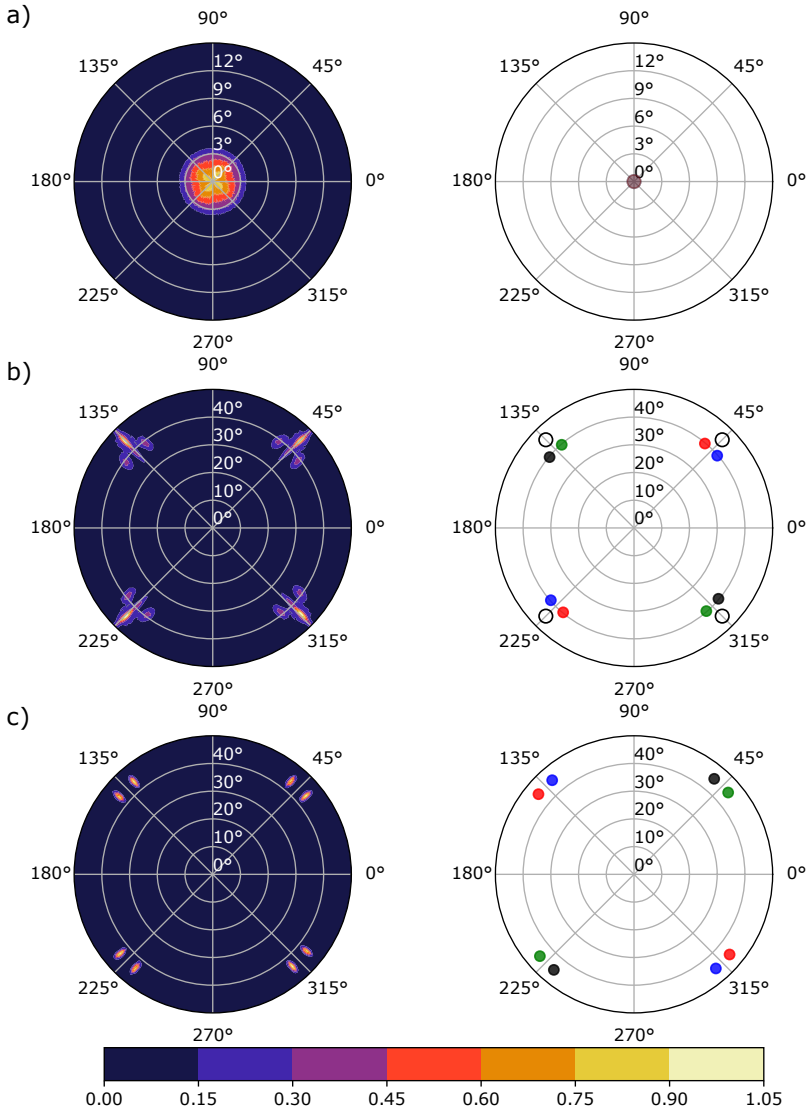

FIGURE 7.3: Pole figures for the a) $(202)_M$ peak at $2\theta = 26.8°$, b) $(202)_M$ peak at $2\theta = 42.59°$, c) $(220)_M$ peak at $2\theta = 46.45°$. On the right side the measurements are shown and on the left side the corresponding calculation of the peak positions for the crystal orientations given by the orientation matrices M_1, M_2, M_3 and M_4. The measurements are normalized to the maximum intensity in the pole figure. The black open circles in b) are indicating diffraction peaks from the (110) Vanadium peak.

austenite and the MgO-substrate is usually not observed in a conventional sample during its martensitic transformation.

Texture measurements for martensite diffraction peaks were performed as well to investigate their orientations in the sample. Selected for this were the $(200)_M$ at $2\theta = 26.8°$, the $(202)_M$ at $2\theta = 42.59°$ and the $(220)_M$ peaks at $2\theta = 46.45°$, which are shown in Figure 7.3 a), b) and c) respectively. Intensity for the $(002)_M$ peak was only observed in the center of the pole figure at $\psi = 0°$ in the ψ-range 0° to 87°. Thus, the $\langle 100 \rangle_{\mathrm{M}}$-directions are always aligned parallel to the $[001]_{\mathrm{MgO}}$-direction for all martensite cells. This further implies that the long $[001]_{\mathrm{M}}$-axis of the tetragonal unit cell has to be orientated in an in-plane direction. For such oriented martensite cells with a tetragonality factor of about c_T =1.202 the $(202)_M$ diffraction peaks should be observed at a ψ-tilt of 39° with a two-fold symmetry for a single martensite orientation. In Figure 7.3 b) four different peaks with a two-fold symmetry are observed at this ψ-tilt. Two of them are centered at $\phi = \pm 5°$ around the $[110]_{\mathrm{MgO}}$-direction at $\phi = 45°$ and the other two likewise centered around the $[\bar{1}10]_{\mathrm{MgO}}$-direction at $\phi = 135°$. This can be understood by solving the compatibility conditions for two martensite variants. A coherent interface between them is possible if they are tilted by a twinning angle α_{TW} to each other. The twinning angle can be obtained by solving the twinning equation or the c_T-ratio according to the equation:

$$\alpha_{TW} = \arctan c_T - \arctan c_T^{-1}. \tag{7.1}$$

For the measured c_T-ratio this yields a twinning angle of 11.5°, which is close to the difference of $(10 \pm 2)°$ measured in the pole figure around the $[110]_{\mathrm{MgO}}$ and $[\bar{1}10]_{\mathrm{MgO}}$-directions. Additionally this confirm the existence of a modulated superstructure present in the martensite nuclei. Another, more intense peak at a ψ-tilt of 45° with a four-fold symmetry is observed in the pole figure. It belongs to the close $\{101\}$ planes of the cubic Vanadium seed layer at $2\theta = 42.14$, which grows on top MgO with the epitaxial relationships $(001)_{\mathrm{V}} \parallel (001)_{\mathrm{MgO}}$ and $(100)_{\mathrm{V}} \parallel (110)_{\mathrm{MgO}}$. In the last pole figure the $(220)_M$ peaks are measured at the predicted ψ-tilt of 45°. They also show the twinning behavior of the $(202)_M$-peaks, confirming the obtained results.

As in the austenite case all texture measurements can also be reproduced by considering four different martensite orientations, given by the matrices M_1 (red), M_2 (blue), M_3 (green), M_4 (black) down below and a Vanadium unit cell fulfilling the epitaxial relationships (black open circles).

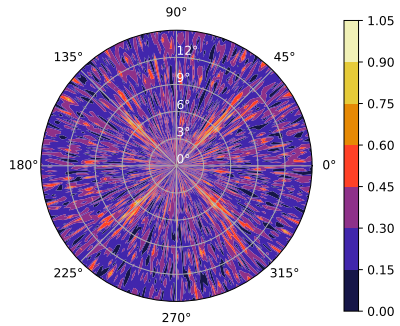

FIGURE 7.4: Pole figure for the $(002)_M$ peak at $2\theta = 26.8°$. The measurement is normalized to the maximum intensity in the pole figure.

$$M_1 = \begin{pmatrix} 0.0 & 4.364 & 5.02 \\ 0.0 & 4.177 & -3.631 \\ 5.535 & 0.0 & 0.0 \end{pmatrix}, \quad M_2 = \begin{pmatrix} 0.0 & 4.276 & 5.096 \\ 0.0 & -4.24 & 3.558 \\ 5.535 & 0.0 & 0.0 \end{pmatrix}$$

$$M_3 = \begin{pmatrix} 0.0 & -4.364 & 5.02 \\ 0.0 & -4.177 & -3.631 \\ 5.535 & 0.0 & 0.0 \end{pmatrix}, \quad M_4 = \begin{pmatrix} 0.0 & 4.276 & -5.096 \\ 0.0 & -4.24 & -3.558 \\ 5.535 & 0.0 & 0.0 \end{pmatrix}$$

As a final experimental verification to the determined orientations an additional pole figure was recorded for the $(002)_M$ peak at $2\theta = 26.8°$, shown in Figure 7.4. In the case of the above mentioned martensite orientations present, no signal should br observed in the ψ-range between 0° to 87°. However, four signals were found at $\psi = 6°$ and $\phi = 45°$, 135°, 225° and 315°, which cannot be explained by the orientations above. A closer investigation is omitted as the intensity is rather small. A $\theta/2\theta$-scan at $\psi = 6°$ $\phi = 45°$ is shown in Figure 7.1 a) and used to directly measure the lattice parameter c for the martensite unit cells. It can be assumed that those four additional orientations are not a major constituent of the checker board itself but belong to martensite regions close to either the interface at the Vanadium seed layer or the sample surface.

Summarizing, four austenite and four major martensite orientations are identified by XRD texture measurements at room temperature in the sample. A clear twinning behavior is observed for the martensite cells. However from the XRD measurements alone, the micro structure of the checkerboard

cannot be determined. Therefore in the next section results from TEM-analysis of the sample is discussed.

7.2 TEM analysis

For the TEM-analysis a cross section is cut out from the sample along the $[110]_{MgO}$ direction by means of Ga^+-ion beam milling at 30 keV and polishing at 5 keV in a FEI Helios DualBeam FIB by Martin Gottschalk and Björn Büker. Two different TEMs were utilized by Daniela Ramermann for this work. A JEOL JEM-2200FS located at the Bielefeld University and a JEOL ARM200F at the University in Paderborn.

7.2.1 General analysis

The checkerboard consists of three different areas, which are shown in Figure 7.5. Visible are two regions of different sizes, which appear as squares and are separated by rectangles. They are therefore labelled throughout this chapter as Small Squares (SS), Large Squares (LS) and Rectangles (R). They are not characterized by their brightness because they depend on the illumination conditions inside the TEM [110]. Both square regions align themselves such that their edges are inclined by $(45 \pm 2)^\circ$ to the sample surface. Furthermore, in both regions strong parallel Moiré-patterns can be observed but not in the R regions. Notably, the Moiré-patterns from the LS and SS regions are perpendicular to each other and are aligned parallel or perpendicular to the sample surface respectively. Moiré-patterns are a kind of interference effect observed in transmission electron microscopy if either [111]:

- two lattices with different lattice spacings are placed on top of each other
- two lattices of the same kind are rotated against each other
- a combination of both aforementioned possibilities

A line profile over several checkerboard regions is utilized to measure the size of the different regions. This is shown in Figure 7.6. From this a size for the LS regions of (50 ± 5) nm, for SS regions a size of (44 ± 4) nm and for the R regions $(50 \pm 5)\,\text{nm} \times (44 \pm 4)$ nm. However, it is difficult to obtain the accurate values for the sizes because the contrast between the regions is strongly dependent on the tilt of the sample. Figure 7.7 shows the normalized contrast difference measured over the same area under different sample tilts. It can be seen that the highest contrast is achieved at around 0°. Within the region of -35° to 35° an oscillatory behavior of the contrast can

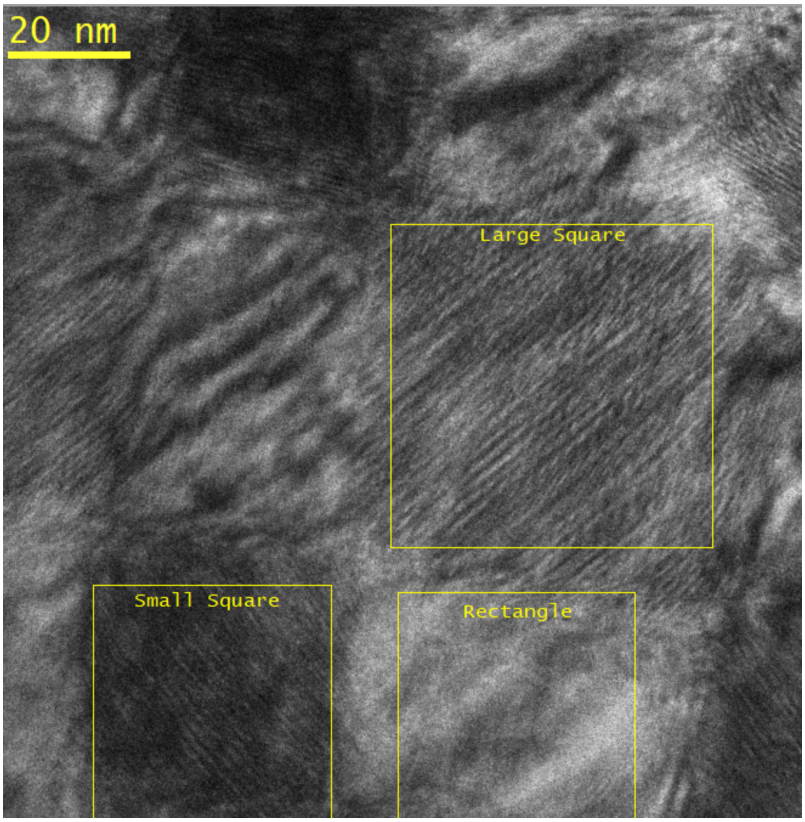

Figure 7.5: High resolution TEM-image of the checkerboard sample. Marked are also the three different regions and area which is used for FFT-analysis.

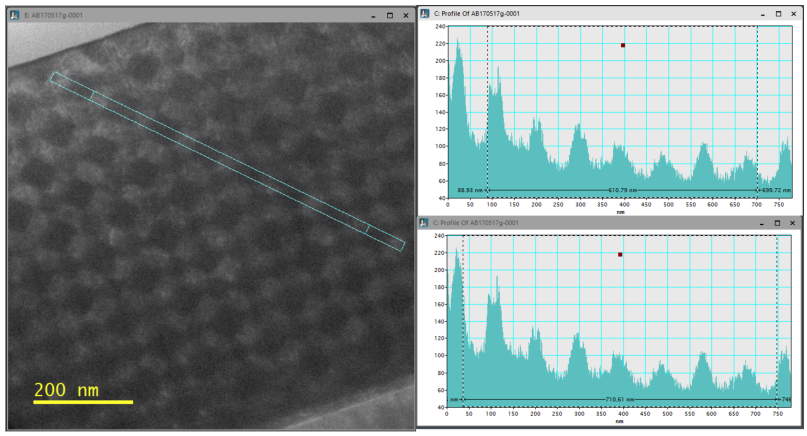

FIGURE 7.6: TEM-cross section of the checkerboard sample along with the line profile over several areas for the calculation of their respective sizes.

be found. At higher tilt angles, the contrast drops to zero and no checker board can be seen.

An explanation for this could be that the contrast difference is caused by the overlap of different crystal lattices in certain regions. Depending on the crystal structures and their orientation to each other electrons might pass the regions easier under certain tilt angles.

From a relative thickness map, recorded in the TEM, a thickness of about 80 nm at the surface of the sample, which increases to about 200 nm to the substrate.

7.2.2 Microstructure analysis

In order to determine the microstructure of the checkerboard it is necessary to link the cell orientations, measured by XRD in the section 7.1, to the different regions shown in the TEM-images. If the first two monolayers of the austenite and martensite orientations from the XRD analysis are projected onto the $[110]_{MgO}/[001]_{MgO}$-plane, three different unique projections should be observable in the TEM-images. They are shown in Figure 7.8 along the distances between the atoms. Note, that for the sake of simplicity the small tilt between the MgO and the four different austenite orientations is neglected as the deviations would result in a deviation less than the resolution capabilities of the analysis down below. For the martensite, two different projections are possible. The first one are the projections of the orientation matrices M_3 and M_4. The second projection stems from the M_1

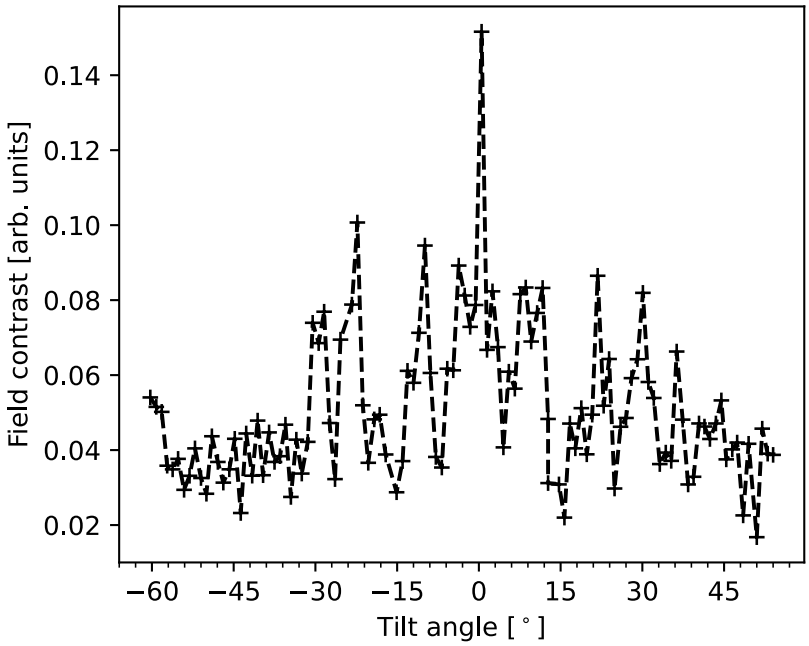

Figure 7.7: Average intensity difference between bright and dark areas in dependence of the tilt angle. Difference is normalized to the sum of the intensities. The dashed lines serve as a guide to the eye. The data were kindly provided by Daniela Ramermann [110].

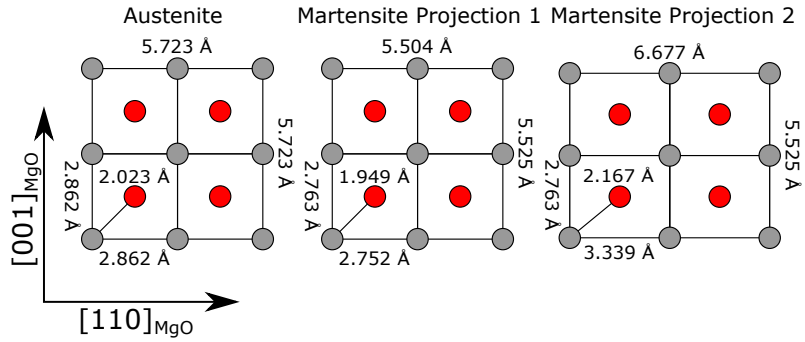

Figure 7.8: Projections of the first two atomic layers of martensite and austenite orientations onto the $[110]_{MgO}/[001]_{MgO}$ plane from the XRD measurements. The small tilt of the austenite cells relative to the MgO-lattice is neglected fro simplicity.

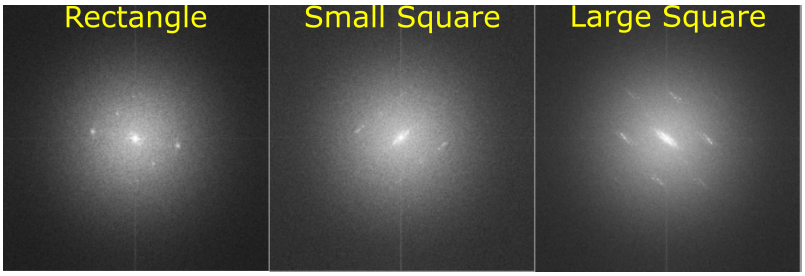

FIGURE 7.9: FFT-images from the regions marked in Figure 7.5

and M_2 orientations. Twinning is not visible if only the first two monolayers are considered in for this projection.
Selective area electron diffraction of the defined areas containing only a single element of the checkerboard structure was not possible due to their small size and limitations of the TEM. Therefore, another approach to identify the orientations is chosen. From the high resolution image the marked areas in Figure 7.5 are cropped from the image and a fast-Fourier transformation (FFT) is applied to them. They are shown for the three regions in Figure 7.9.

In all FFT images several spots can be seen, which contain the interatomic distances present. The rectangle regions shows only a small amount of spots while the square regions display a much more complicated pattern. Due to the high background and the weak intensity of the spots their position in the FFT image cannot be measured very well by simply taking line-profiles of the images. In order to quantify them more accurately the following analysis procedure is employed:
In a first step the absolute square values of the FFT images are smoothed by a gaussian filter in order to reduce the noise. Care must be taken in choosing the window size for the filter as this could introduce artifacts or smooth out low intensity signals. A window size of 2 by 2 pixel was deemed sufficient for this study. Each pixel of the smoothed image is then assigned a radius r' from the image center, calculated from the pixel position and rounded to the nearest integer value. r' is then scaled by the FFT pixel scaling factor to yield a proper distance in reciprocal space. From all pixels with the same radius from the center the variance is calculated. If a peak is located in the FFT image at a particular radius the variance should be significantly higher than the variance obtained at a radius containing only smoothed noise. To further enhance the visibility of the peaks the variance is divided by the sum of the pixel intensities. Obtained values are plotted against r'^{-1} to convert the radii to atomic distances in real space. This procedure is similar to

power spectral density (PSD) analysis of signals. Possible peak positions and widths are found by a peak search algorithm.
The found peaks do not necessarily belong to a peak in the FFT image but can also be caused by artifacts of the transformation process or the smoothing of the image. Thus it is necessary for each peak to calculate the anisotropy of the intensity distribution. For a real signal most of the intensity of the peak should be contained in certain angle intervals around the center while for artifacts only noise should be detected. Therefore, from each peak position and width an inner radius r'_i and outer radius r'_o is defined and the pixels outside this interval are masked. The remaining pixels inside this ring are then split in angle intervals of 1° beginning from the top of the image in clock-wise direction and summed over. They are normalized by the total intensity of the ring and plotted against the angle. For further discussion only peaks clearly visible in the anisotropy spectrum are plotted and the rest is discarded.
It should be noted that there are limitations to this analysis method. Peaks close to the center of the FFT image are less accurate to analyze because the distance in real space is inversely proportional to r'. It is also evident that the pixel density for a small radius is quite low compared to a larger radius thus, in the anisotropy measurement not all angle intervals contain a pixel. In all following variance plots, a single dashed, gray, vertical line is plotted marking the distance where every angle contains at least one pixel.

Other sources of errors leading to deviations in the measurements can occur during the sample preparation and measurement. The largest source of error might be a misalignment to the $[110]_{\mathrm{MgO}}$ direction during the ion beam milling process. Also local deformations in the TEM lamella and sample mounting can further introduce errors. An error of 0.5 % for he measured lengths and an error of 5° for the measured angles is therefore estimated to account for these sources of error.

Applying the aforementioned analysis procedure for the FFT in Figure 7.9 of the rectangle region yields the variance and anisotropy plots shown in Figure 7.10 a) and b). Only two clearly visible peaks are found in this region at the distances 2.022 Å (red) and 2.810 Å (blue) in the variance plot. Comparing these values to the smallest atomic distances of the austenite projection in Figure 7.8 we find an almost perfect agreement for the distances between the gray border atoms (2.862 Å) and the distance between the border atoms and the red center atoms (2.023 Å). Strong signals are observed in the anisotropy plot at 170° and 350° for the 2.022 Å distance and at 126° and 306° for the 2.819 Å distance. Between them is an angle difference of 44°, which is close to the expected value for the cubic austenite cell. However, neither of the large signals shows the expected four-fold symmetry, which could be due to the low quality of high-resolution TEM-image. Two smaller

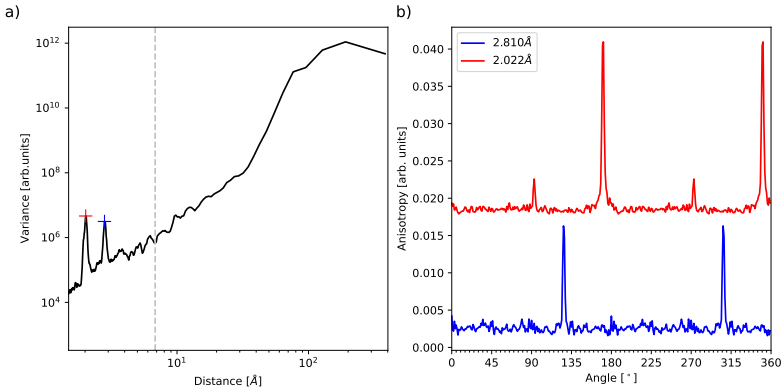

FIGURE 7.10: a) Variance in dependence of the distance from the center of the FFT-image for the R region. Investigated peaks are marked by a colored cross. b) Anisotropy of the intensity for the investigated peaks in a) in dependence of the angle.

peaks are measured at 93° and 273° for the 2.022 Å distance. Between them and the larger peaks only a 77° relation is calculated instead of the expected 90°. This can either hint at another austenite orientation present in this region or the peaks are caused by artifacts. A second austenite direction with such a large tilt however stands in contrast to the measured XRD pole figures, which confirm only slight tilts of a few degrees between them. Also one could expect Moiré-patterns to emerge from two tilted unit cells, which is not observed in any rectangle region even under different tilt conditions. Thus, those small peaks are likely to be caused by artifacts. To conclude the rectangle regions consists of a single austenite orientation. Furthermore, since the edge-atoms distances from the austenite point almost along the $\langle 110 \rangle_{MgO}$ or $\langle 001 \rangle_{MgO}$ directions, those directions should be found around 35°, 125°, 215° and 305°.

Focusing of the small square area, a much different behavior is found. The results of the peak analysis are shown in Figure 7.11. Five different distances are found with a clear anisotropy at 1.940 Å (cyan), 2.044 Å (orange), 2.209 Å (green), 2.711 Å (red) and 17.374 Å (blue). Similar to the rectangle region the austenite edge-center atom distance (2.023 Å) fits well to the measured 2.044 Å with the large peaks occurring at almost same angle of 169° and 349°. Also two smaller peaks are located at 90° and 270°. Since they also do not share 90° relations to the larger peaks they are considered as artifacts as well. A distance matching the austenite edge-atoms is not found.

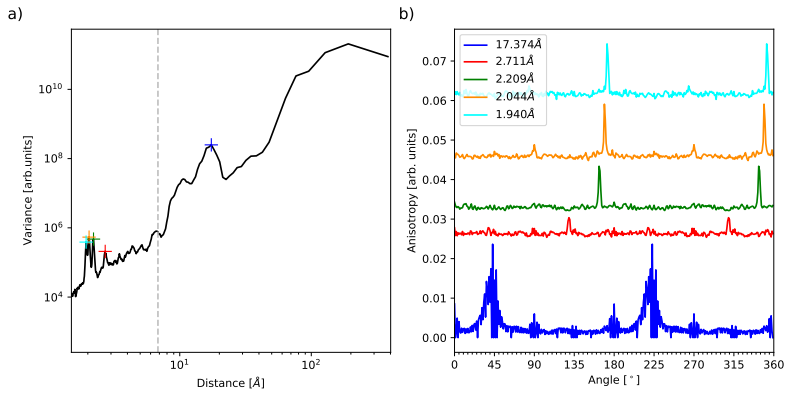

FIGURE 7.11: a) Variance in dependence of the distance from the center of the FFT-image for the SS region. Investigated peaks are marked by a colored cross. b) Anisotropy of the intensity for the investigated peaks in a) in dependence of the angle.

On the other side clear indications for the presence of martensite cells are visible. The smallest distance of 1.940 Å is close to the expected value for the edge-center atom of the martensite projection 1. Two small and two large peaks are seen in the anisotropy plot for this distance at 84°, 172°, 264° and 352°. Unlike the austenite those peaks feature an average distance of $(90 \pm 2)°$ to each other, being the only lattice distance with a four-fold symmetry. From the XRD pole figures an angle of 45° between the $[110]_M$ direction and the $[110]_{MgO}$ or the $[001]_{MgO}$ is expected. Taking the estimated angles for the MgO-directions confirms that the difference in angles is between 47° to 49°. The edge-center distance from the first martensite projection is measured and with a distance of 2.209 Å, compares well to the expected distance in the second martensite projection of 2.167 Å. They occur at 163° and 343°. Special about this martensite direction is that its angle to the $[110]_{MgO}$ and its angle to the $[001]_{MgO}$ direction do not coincide thus allowing differentiation between the two MgO-directions. The calculated difference between the martensite peak at 163° and the MgO-direction at 125° equals 38°, which is close to the expected value of 39° to the $[110]_{MgO}$ direction. Conversely to the perpendicular MgO-direction at 215° their difference is 52°, which again is quite close for the expected angle of 51° to the $[100]_{MgO}$ direction. Thus the $[001]_{MgO}$ direction can be associated with the angle 35° and the $[00\bar{1}]_{MgO}$ direction can be associated with the angle 215°. It follows, the $[110]_{MgO}$ direction is found at 215° and the $[\bar{1}\bar{1}0]_{MgO}$ direc-

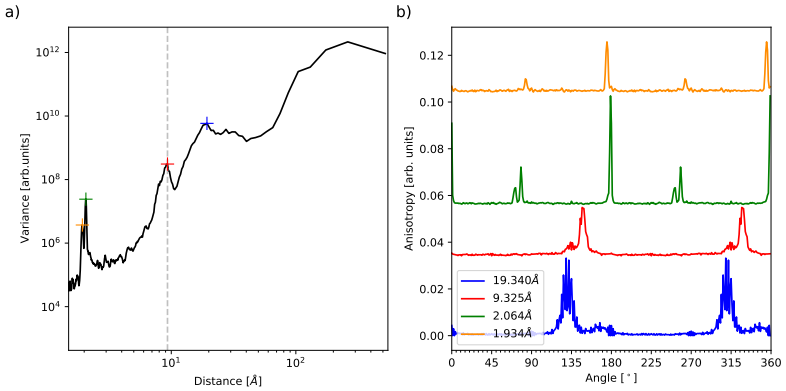

FIGURE 7.12: a) Variance in dependence of the distance from the center of the FFT-image for the LS region. Investigated peaks are marked by a colored cross. b) Anisotropy of the intensity for the investigated peaks in a) in dependence of the angle.

tion at 305°. The measured atomic distance of 2.711 Å could be either the edge atom distances from the $[110]_{MgO}$ direction of the martensite projection 1 or from the $[001]_{MgO}$ directions of both martensite projection. The peak occurrence at 129° and 309°, which is close to the $[110]_{MgO}$ direction, suggests that the first assumption holds true. The last measured distance of 17.374 Å peaks are found at about 42° and 222°. This large distance cannot be associated with interatomic distances from the crystal structures. Instead it belongs to the observed Moiré-pattern present in this region. Due to the low accuracy and the large amount of possible combinations of interatomic distances it is not possible to gain further insight about the microstructure from them.

Similar to the small square area the large square region contains several peaks inside the FFT image, which are shown in Figure 7.12. Only four different distances are found this time at 1.934 Å (orange), 2.064 Å (green), 9.325 Å (red) and 19.340 Å (blue). The two largest distances result from the visible Moiré-patterns in this region. For the 19.340 Å distance two large peaks were found at 130° and 310° and two smaller peaks at 167° and 347°, while for the 9.325 Å Moiré-pattern only peaks at 148° and 328° were found. The small shoulder visible on the left side of each peak is probably an artifact from the large 19.340 Å Moiré. As in the case before, those peaks cannot be utilized to obtain additional structural information about the sample as it is not possible to determine which combination of lattice spacing would yield

them. The smallest spacing of 1.934 Å can be identified as the edge-center atom distance of the martensite projection 1. Again their peaks have a 90° distance to their neighboring peaks and are almost 45° tilted to their nearest MgO directions.
For the 2.064 Å distance, which is very close to the austenite center-edge distance, six peaks can be seen. The peaks, located at 78° and 258°, have an almost 45° difference to the nearest MgO directions and therefore fit the expectations well. For the other four peaks this does not hold true. The smallest peak at 71° has a difference of 36° to the $[001]_{MgO}$ direction and a difference of 54° to the $[110]_{MgO}$ direction. Likewise the largest peak at 179° has a difference of 36° to the $[00\bar{1}]_{MgO}$ direction and a difference of 54° to the $[110]_{MgO}$ direction. The same holds true for the peaks 180° relative to them. It is unlikely that these peaks result from the austenite as the angle difference is not symmetric to the MgO directions.There might be a different interpretation: On a closer look, in Figure 7.12 a) a small dip on the right side of the corresponding peak at 2.18 Å is barely visible. This small signal cannot be separated from the peak but the measured distance for this dip is very close to the center-edge distance occurring in the martensite projection 2. This interpretation, however leads to an inconsistency with the XRD measurements, as this would necessitate a martensite unit cell orientation with the long c-axis tilt by 3° in the out-of-plane direction. Such orientated martensite cells with a 3° ψ-tilt were found in the pole figure Figure 7.4 but they were neglected due to their low intensity. The existance of martensite, oriented this way in the sample, could not be determined or in case it exists, might belong to austenite orientations or are artificial spots otherwise.

Despite this, the analysis confirms that the contrast between the checker board regions is caused by the presence of different martensite and austenite unit cells. The rectangle regions, which show no Moiré-patterns, consist of only austenite unit cells. In contrast to that, a martensite nucleus is present in both square regions with different martensite orientations. This probably results from a modulated structure, but this cannot be verified because of poor image quality. Austenite signals could be measured in those regions as well. The austenite is most likely located before or behind the martensite nuclei, which is possible due to the large thickness of the TEM-lamella. The exact 3D shape of those nuclei remains unclear.

7.2.3 Chemical analysis

Not only the mircostructure of the checkerboard regions is important but also their position relative to the martensitic intercalations and active layers, which will be investigated in this section. The interfaces of these layers can only be resolved by chemical analysis of the checkerboard. Thus EDX-

measurements are performed in the ARM200F-TEM with a 200 kV excitation voltage in the energy range from 0 keV to 20.48 keV with a resolution of 10 eV. In order to yield better HRTEM images the rather thick sample was rethinned in a second perparation step inside the FIB. Evaluation and calculation of the chemical composition were carried out by the Gatan GMS3 STEM SI toolbox.

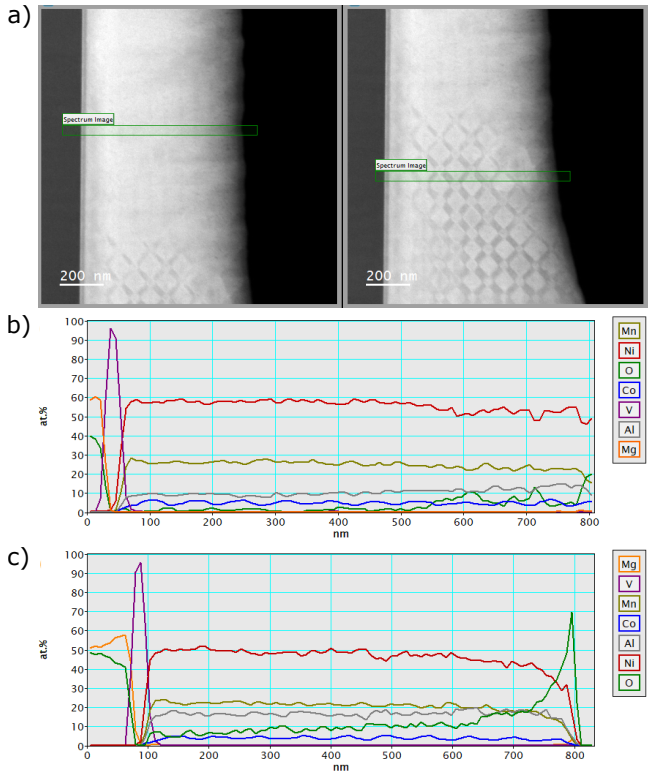

Figure 7.13: a) STEM-dark field images used for the EDX-lineprofiles of the rethinned lamella. The green boxes indicate the areas used to measure the EDX-lineprofiles. Atomic concentrations in dependence of the depth for several elements determined from EDX-measurements b) of the region with visible checkerboard and c) without checkerboard. MgO-substrate is always to the left of the profiles. The data was kindly provided by Daniela Ramermann [110]

.

In Figure 7.13 a) STEM-dark field (DF) images of the rethinned lamella

are shown. Notable changes in the checkerboard are present compared to the prior measurements. First of all, in the center part of the lamella the checkerboard has completely vanished, while only a the ends of the lamella the checkerboard is present. There are also notable changes in the sizes of the rectangles and small squares at if the local thicknesses of the lamella changes. One reason for this could be aging effects, such as oxidization, which is discussed in more detail in the recent PhD-thesis of Daniela Ramermann [110].

EDX-lineprofiles, perpendicular to the sample surface, were recorded at the marked regions for an area with and without a checkerboard pattern to ensure that no chemical deviations occur in those regions. They are shown in Figure 7.13 b) and c) respectively for O, Mg, Al, V, Mn, Co and Ni. The MgO-substrate and V seed layer are easily recognized in the left part of the profiles. Mn, Ni and Al seems to be constant throughout the entire Heusler compound layer. The Co, however, shows a clear oscillatory behavior, which is expected as the Co power was adjusted during the deposition of the MI and AL films. For the determination of the chemical composition of the two layers, regions of 24.7 nm with around a Co maximum and Co minimum were extracted and averaged over from the two lineprofiles. The compositions are accordingly labelled as On Check for the values from profile Figure 7.13 b) and Off Check from profile Figure 7.13 c). A third lineprofile, which was recorded at another region without the checkerboard and labelled Off Check2, is not shown here. The resulting values are listed in Table 7.1. Concentration measurements from EDX for thin sample systems tend to be only accurate within 5% without a proper calibration sample [112], which was not available for this investigation.

Table 7.1: Chemical composition of Heusler compound on areas with and without checkerboard. The data points are taken from the lineprofiles shown in Figure 7.13 b) and c). The composition is averaged over a 24.7 nm wide region. The listed errors are the standard deviation calculated from the data points. The Off Check2 values are extracted from a lineprofile at another position of the lamella, which is not shown here.

Region	Ni [at.%]	Co [at.%]	Mn [at.%]	Al [at.%]
On Check, Co max	58.6 ± 1.0	6.0 ± 0.3	26.5 ± 0.7	8.9 ± 0.6
On Check, Co min	58.9 ± 0.4	4.5 ± 0.2	26.9 ± 0.9	9.7 ± 0.8
Off Check, Co max	54.0 ± 0.4	5.5 ± 0.4	23.1 ± 0.1	17.3 ± 0.6
Off Check, Co min	54.7 ± 1.6	3.6 ± 0.1	24.3 ± 0.4	17.5 ± 1.7
Off Check2, Co max	50.7 ± 0.9	5.3 ± 0.3	23.6 ± 1.1	20.3 ± 0.1
Off Check2, Co max	51.5 ± 0.8	3.6 ± 0.1	25.0 ± 0.5	19.9 ± 0.9

For the Ni content, which should be equal throughout the sample, a lot of variation was measured for the different lineprofiles ranging from 50.7 at % to 58.9 at %. The difference between the Co minimum and Co maximum within one lineprofile is always less then 1 at %. The largest concentration was was found for the relatively thick checkerboard region, indicating a thickness dependence in the final concentration result. The closest value of around (51 ± 5) at % to the nominal Ni concentration of 45 at % is measured for the Off Check2 region. For Mn, which is also held at constant power during the deposition process, the spread of the conentrations is rather consistent, ranging from 23.1 at % to 26.9 at %. In the NiMnAl-shape memory system the Heusler compound, ab-inito simulations found that excess Mn has to be present for the martensitic transformation to occur. Therefore the measured Mn concentration should be closer to 30 at %, which is in the error interval of 5%. For the Co concentration, a consistent value of 3.6 at % for the minima and a value of 5.5 at % is measured form the lineprofiles without the checkerboard pattern. The checkerboard region yields a 1 at % higher value for both regions. The largest uncertainty factor is the Al content. Large deviations for more than 10 at % are measured between the regions with and without the checkerboard. An Al content with less than 10 at % is not possible because at such low Al contents the martensitic transformation is suppressed by the kinetic arrest phenomena. The obtained concentrations on the checkerboard regions are therefore considered too inaccurate for interpretation purposes. The obtained values around 17 at % and 20 at % for the non checkerboard regions are much closer to realistic Al contents. A distinction between the regions of high Co and low Co content

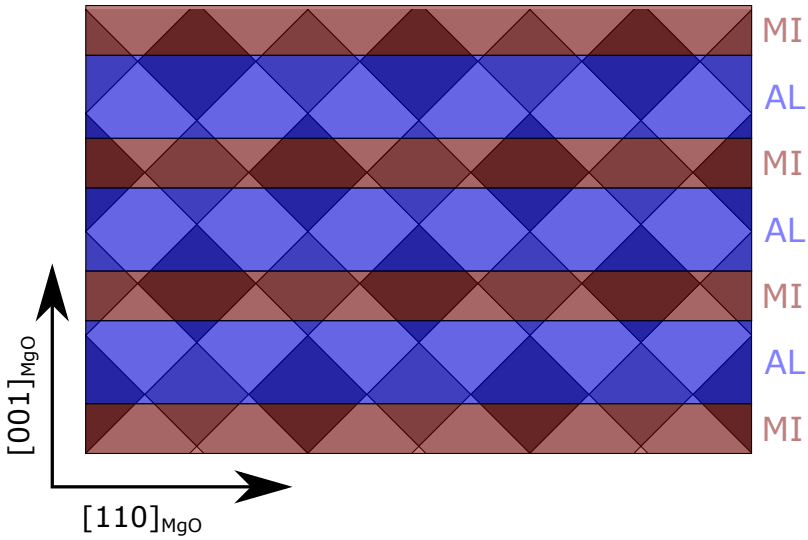

Figure 7.14: Illustration of the relation between the thicknesses of the martensite intercalaionts and active layers to the sizes of the R, SS and LS regions. All sizes are scaled to the measured values.

cannot be made, because thee difference in the nominal Al concentration is just 2 at %. As a much lighter element than the other three, Al in particular is, not easy to quantify in EDX due to it's low x-ray fluorescence yield. This might also explain the absence of oscillations in the lineprofile.
From the Co lineprofile, a thickness of (32.9 ± 8.2) nm for the layers with low Co content is measured and a thickness of (49.4 ± 8.2) nm with high Co content. This agrees well with the intended thicknesses of 30 nm for the MI layers and 50 nm for the AL layers. Based on this it is assumed that the layer structure in the checkerboard sample is intact.

By illustrating the measured sizes for the R, SS and LS regions and the thicknesses of the MI and AL layers, the relative relationship between them can be seen in Figure 7.14. The square areas are drawn as dark regions separated by the rectangluar bright regions. The intercalations and active layers are marked by the red and blue area respectively. The sizes of the elements in the illustration scale to the measured values. A clear relationship between the layer thicknesses and the sizes of the checkerboard regions is not visible. The interfaces seem to roughly coincide with the edges of the square regions but this is not always the case. This is clear evidence that neither the intercalations nor the active layers are fully in the austenite or martensite

state. There may be a dependence between the region sizes and the thicknesses present but they are not mainly responsible for the final arrangement of the checkerboard pattern. The elastic coupling between them might be responsible for this.

7.2.4 3D model of the checkerboard structure

It is still challenging to determine an exact 3D model for the arrangement of the martensite nuclei in the sample. A simple model is discussed in this section based on the observations made before. First, the contrast in the checkerboard is of crystallographic origin. Regions of pure austenite are more transparent to the electron beam and therefore appear bright, while regions containing martensite appear dark. In the thick lamella, the martensite is always accompanied by austenite, which is believed to be the reason for the low transparency of the electrons in those regions.
Second, the regions containing martensite appear always as squares in the TEM cross section with their edges pointing along the out-of-plane and in-plane directions. Thus the martensite nuclei have to have a shape providing a square cross section.
Third, a strong dependence of the lamella's thickness on the visibility of the checkerboard is observed. A strong difference in contrast can be seen in rather thick lamellas, while it vanishes completely in thinner ones and is replaced by layers with weak contrast difference in STEM images. Furthermore, a thickness dependence of the square and rectangle regions is observed in the transition areas between checkerboard and non-checkerboard regions.
In the XRD measurements, only two martensite variants, which correspond to the rotated cells given by the matrices U_2 and U_3 given in Equation 2.6, could be measured and confirmed by TEM images. It is assumed that a modulated arrangement of those two variants form all martensite nuclei in the sample. From the measured lattice constants of the unit cells the values $\alpha = 0.96059$ and $\beta = 1.15466$ are calculated. Following the results of Ball and James [28] from those two values a possible orientation for the habit plane as a solution to Equation 2.10 can be calculated. One of the eight possible solutions is given by the vector:

$$\vec{m} = \begin{pmatrix} 1.723 \\ 0.096 \\ 1 \end{pmatrix}. \tag{7.2}$$

The values of this vector refer to the cubic austenite reference system. Considering the relative orientation to the MgO-substrate this vector translates

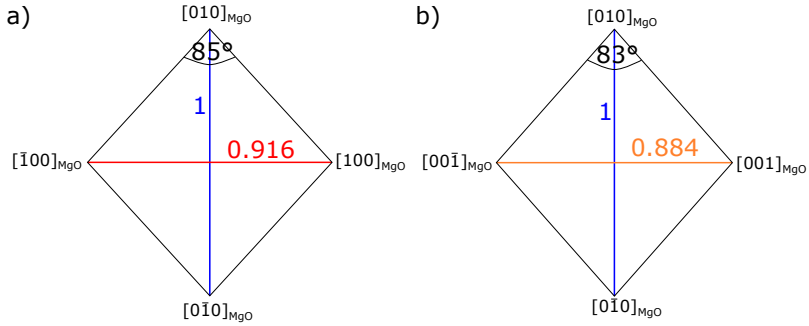

FIGURE 7.15: Illustration of the deformed octaeder martensite nuclei projected on the a) $[100]_{MgO}/[010]_{MgO}$ plane and b) $[001]_{MgO}/[010]_{MgO}$ plane. The colored lines are the axis of this shape and the slices through the habit planes are shown as the black outline.

to

$$\hat{m} = \begin{pmatrix} 0.5639 \\ 0.6324 \\ 0.5311 \end{pmatrix} \tag{7.3}$$

in the MgO reference system. The other vectors are found by changing the signs of the components. These vectors are inclined by a few degrees to the $\{111\}_{MgO}$ planes. Constructing a 3D shape form those planes results in a slightly deformed ocataeder. the projections of this nucleus onto the $[100]_{MgO}/[010]_{MgO}$ plane and onto the $[001]_{MgO}/[010]_{MgO}$ plane along with the aspect ratios of the axis are depicted in Figure 7.15 a) and b) respectively. If this structure is looked at from the $[110]_{MgO}$ an almost square cross section can be seen, in which martensite and austenite overlap, which is a key requirement for the checkerboard.

In experiments from the martensitic transformation of Ni-Mn-Ga thin films, it is observed that martensite tends to nucleate in parallel, similarly shaped nuclei in a regular distance d_0. For this reason it is proposed that an autonucleation process is of importance for the martensitic transformation [35]. This process assumes that a primary martensite nucleus induces an inhomogeneous elastic stray field in the surrounding austenite matrix, which facilitates the growth of other nuclei in a certain distance and direction. The distance of two adjacent nuclei is proportinal to the width b_0 of the martensite nucleus:

$$d_0 = r \cdot b_0. \tag{7.4}$$

In the FEM simulations, considering only the volume change during the martensitic transformation, the proportionality factor r is determined to be

around 2 for nuclei inside the volume [35, 113].

It is possible to explain the occurrence of this regular pattern if this autonucleation process is happening in the sample and the martensite nuclei take the shape of distorted octaeder, with it's faces inclined by a few degrees to the $\{111\}_{MgO}$ planes. The disappearance of the checkerboard at thin points of the lamella can also be explained. At smaller thicknesses, the areas where martensite and austenite overlap also become smaller. If one also assumes that electron scattering is mainly proportional to the superposition of austenite and martensite, the areas of different contrast would completely vanish for very small thicknesses. Instead, they could be replaced by layers with light contrast differences, whereby the contrast could be caused by the different composition of the active layers and martensitic intercalations. In fact, Daniela Ramermann shows a correlation between the thicknesses of these layers and the Co EDX lineprofile, further supporting the hypothesis [110].

The obtained data so far is insufficient to verify this model for the arrangement of martensite nuclei in the intercalations sample. Thus additional proof should be acquired by comparison of different TEM cross sections in cut along different crystallographic directions or 3D structure reconstructions from several tomography measurements.

7.2.5 Influences of the MI and AL thickness on the checkerboard formation

At last, the influence of different intercalation and active layer thicknesses is investigated for the checkerboard. In this section four different samples are considered. The first sample is the 7MI taken from the MI-sample series presented in chapter 6. This sample consists of 7 martensitic intercalations with a thickness of 30 nm and 6 active layers with a thickness of 100 nm. Additionally, three more samples were prepared by sputter deposition in the same manner as the samples in the intercalation sample series. Each of them features 5 active layers, which are sandwiched between 6 martensitic intercalations. The first sample has a MI thickness of 10 nm and an AL thickness of 30 nm and therefore labelled as MI10/30. For the second sample the MI thickness was increased to 30 nm such that both thicknesses are equal. It is referred to as MI30/30. The last sample is a simple reproduction of the original checkerboard but with fewer intercalations. The sample is accordingly labelled as MI30/50. For each TEM-investigation, a lamella is cut from the sample along the $[110]_{MgO}$ direction.

In a survey image of the 7MI sample, shown in Figure 7.16 no immediate checkerboard structures can be identified. In the inset a magnification of an area close to the surface of the sample is shown. On closer inspection,

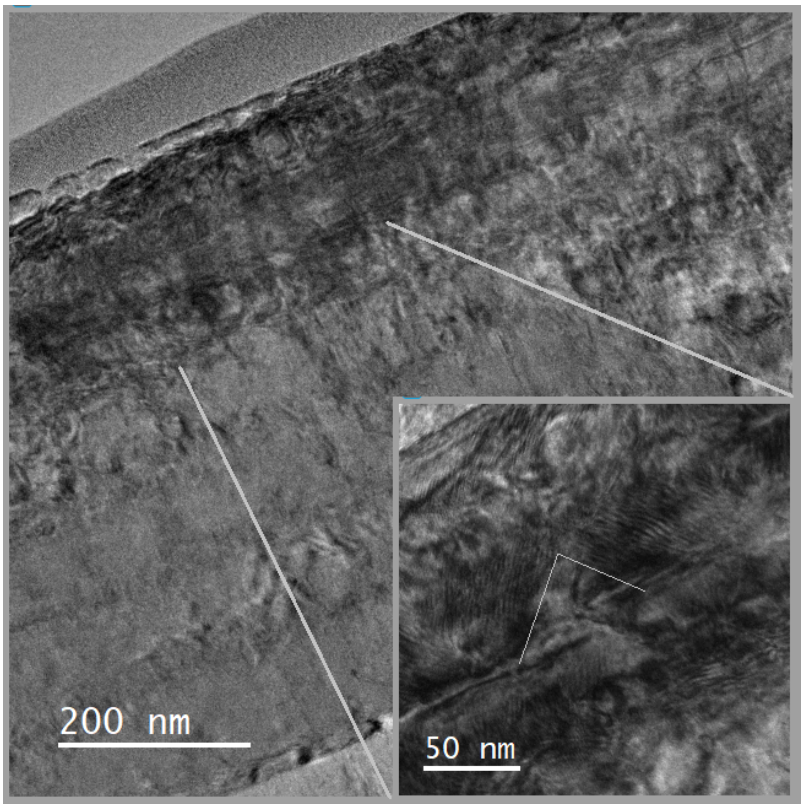

Figure 7.16: TEM cross section of the 7MI sample. A checkerboard is not visible in the survey can. The inset contains a close up of the marked region. Moiré-patterns, which are tilted by 90° to each other, are slightly visible within. The data were kindly provided by Daniela Ramermann [110].

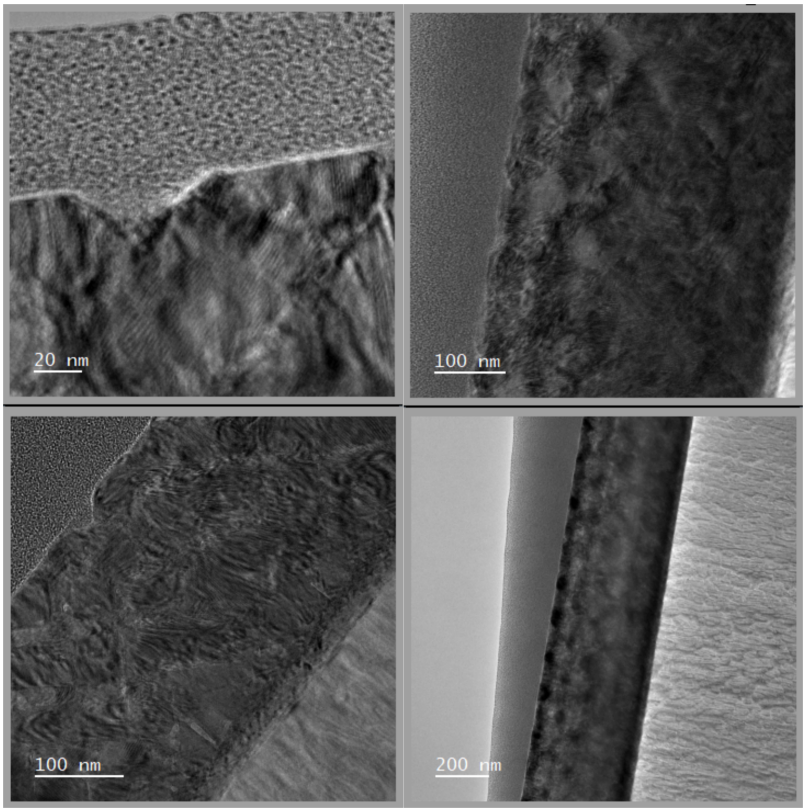

FIGURE 7.17: TEM cross sections of the MI30/30 sample (left) and the MI30/50-sample (right). The top row is a magnification of the overview images in the bottom row. The data were kindly provided by Daniela Ramermann [110].

rectangular regions containing Moiré-patterns can be identified. Similar to the checkerboard sample those regions are tilted by 45° to the sample surface. Another shared feature for both samples is the perpendicular arrangement of the Moiré-patterns of two adjacent regions. Considering this the sample might be on the verge of forming the regular arrangement of martensite nuclei.

In the MI30/30 and MI30/50 samples the checkerboard arrangement is present, as shown in Figure 7.17, on the left and right side respectively, although the contrast between the regions is not as large as in the original checkerboard specimen. This could be due to a smaller thickness of both

cross sections. The boundaries of between the regions, stretching over the entire Heusler compound film, from the MI30/30 sample can be clearly seen in a brigth-field STEM image, shown in Figure 7.18, where they appear very bright. The low contrast in both samples makes it difficult to determine their respective field sizes. In the MI30/30 sample small squares with an edge length of about (25.3 ± 8.2) nm and large squares with (46.8 ± 7.6) nm are measured. The rectangle areas have therefore sizes of (25.3 ± 8.2) nm x (46.8 ± 7.6) nm. In the MI30/50 sample, slightly larger sizes were determined. Values of (38.3 ± 5.2) nm for the small squares, (53.7 ± 6.6) nm for the large squares and (38.3 ± 5.2) nm x (53.7 ± 6.6) nm for the rectangle regions are obtained. The sizes are similar to the ones in the original checkerboard, thus the size of the regions is almost independent of the thicknesses of the intercalations and active layers.

In the MI10/30 sample no notable features of a checkerboard formation can be detected. This is important because this sample and the 7MI sample represent the limits for the thicknesses of the intercalations and the active layers for the checkerboard formation by autonucleation. FEM calculations predict an inhomogeneous elastic stray field in an austenite matrix induced by a primary martensite nucleus. This stray field can facilitate the nucleation of secondary martensite nuclei in preferred locations and orientations. For the formation of the checkerboard structure those stray fields from the primary nuclei, which will nucleate in the martensitic intercalations, need to facilitate the nucleation of martensite in the active layer regions. The absence of the checkerboard in the 7MI sample suggests, that the regular arrangement of the nuclei is only possible, if the elastic stray fields from the top and bottom martensitic intercalations penetrate most of the active layer region. Thus there is an upper limit to the thickness to the active layers.

On the other hand, if the martensite intercalation thickness is too small nucleation of primary nuclei might not be possible. It is energetically unfavorable to form small martensitic nuclei below a critical size because the elastic energy stored in the habit-planes and twin boundaries exceeds the reduction in inner energy by the martensitic transformation. Thus, the checkerboard formation is suppressed, which might be the reason for the absence of the checkerboard in the MI10/30 sample.

7.3 Conclusion

In this chapter the structure of the checkerboard sample microstructure is investigated by XRD- and TEM-analysis. We found that in this sample four different austenite orientations and at least four different martensite orientations are present in this sample. The observed contrast in thick TEM

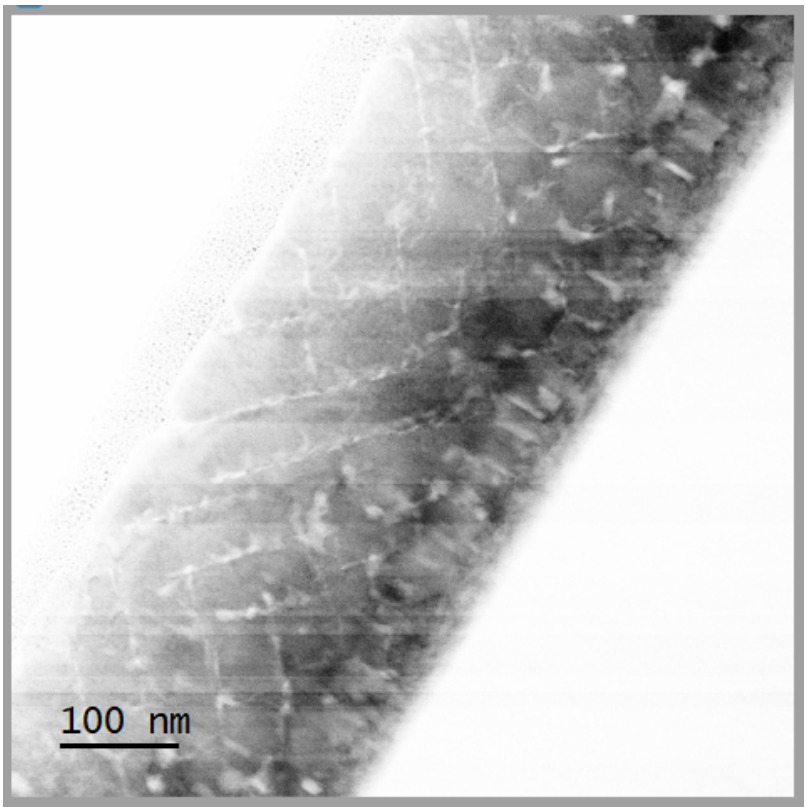

Figure 7.18: Bright-field STEM image of the MI30/30 sample. A rectangular pattern tilted by 45° to the surface normal is seen. The substrate is located at the bottom right of the image. The data were kindly provided by Daniela Ramermann [110].

specimen is due to the arrangement of evenly spaced martensite nuclei surrounded by austenite. Regions, where martensite and austenite overlap appear dark while regions containing only austenite appear very bright. Notably, the checkerboard can only be seen if the specimen is rather thick and vanishes completely in thin samples. Based on the data and phenomenological martensite theory the shape of the martensite nuclei might resemble slightly deformed octaeders, which appear as squares in a cross section. No clear relation between the position of this nuclei and the position of intercalation or active layer can be derived. Consequently, the arrangement of the martensite cores in the austenite matrix is probably governed by local elastic stray fields of the primary nuclei in the intercalations, which facilitate the growth of secondary nuclei. Thus, it is important for this microstructure to develop is a sufficiently large thickness of the intercalation layers such that primary nuclei can form in the multilayer sample. Likewise, the thickness of the active layers must not be too large because the induced elastic strain fields has to to influence almost the entire volume of the active layers. Further studies of the minimum intercalation thicknesses and distances at which this ordering occurs can provide insight into the energy barriers during the nucleation process of martensitic transformation. It would also be interesting to repeat this experiment with materials that do not undergo a cubic to tetragonal martensitic transformation, such as NiTi. One could expect to observe a different pattern in TEM cross sections.

Summary 8

In this work we investigated different mechanisms to influence the MT in Ni-Co-Mn-Al thin film system. Special emphasis is given to the improvement the thermal hysteresis occurring in this material to enhance their applicability. Three different approaches were investigated.

In the first method the MPE is investigated as an alternative to doping the compound with ferromagnetic material to enhance the magnetization in the austenite state. Because the investigation and quantification of the proximity effect in a material with MT cannot reliably done by XMCD and XRMR a proof-of-principle study with stoichiometric Ni_2MnAl is performed. The obtained results do indeed show a ferromagnetic alignment for the Mn and Ni magnetic moments at the interface. Due to many similarities found between these and the doping of the Mn-rich Ni-Mn-Al-system it can be concluded that the MPE can be utilized to improve magnetization in the austenite state. However, a major drawback is the small penetration depth of less than 1 nm, which makes this method the least effective for real applications.

Another way to change the transformation behavior is by utilizing structural defects in the crystal lattice, which might reduce the nucleation energy barrier and thus decreases hysteresis width. Point like defects can be generated in the sample by ion beam bombardment. Up to an ion fluence of 1×10^{14} ions/cm^2 impacts on the martensitic transformation can be detected. The main change is that with increasing fluence the transition shifts to higher temperatures, while no significant reduction in the hysteresis width could be measured. But a major impact on the magnetism in the Heusler material is detected as well. Upon increasing the defect concentration a great reduction in the magnetization in the austenite is measured, which can have a negative impact on desirable effects such as the cooling capacity for magnetocalorics. However, the ability to tune the transformation temperature by ion beam irradiation in these materials can be utilized to tailor them for specific applications.

As a last method, investigated in this work, we prepared multilayer systems consisting of two different Ni-Co-Mn-Al compositions with one having a MT above and one having a MT below room temperature. The trans-

formation behavior of the layers with MT below RT were investigated. We find that the hysteresis width almost steadily decreases if more intercalations are present, thus these can facilitate the growth of martensite in the AL's. Two different transformation ranges can be distinguished. If the AL's are significantly thicker than the MI's the transformation temperature for the martensitic transformation shifts to higher temperature while the reverse transformation is unaffected. However, the intercalations might also serve as barriers, which limit the maximum size of the martensite nuclei in the AL's. Thus, with increasing numbers of intercalations more residual austenite remains present at low temperatures. If the thicknesses become comparable elastic coupling between the layers dominates the transformation process, which results in an ordered distribution of martensite and austenite regions.

Outlook: Magnetic shape memory nanoparticles 9

In this work so far only defects and interactions between the MSMA and additional layers were investigated and utilized in order to influence the MT behavior in those alloys. Another possible way of changing the transformation in small volume systems is by controlling the size and shape of the sample. Therefore, the transformation behavior in low dimensional systems, such as nanoparticles (NPs) and nanowires, could be particularly interesting to investigate. Especially Heusler compound nanoparticles in general are relatively uninvestigated [114]. This is due to their difficult production as Heusler compounds get their unique properties not only from their chemical composition, which involves at lest three elements, but also from their crystal structure.

Synthesis by conventional chemical means is often not possible, because suitable precursor molecules and suitable crystallization conditions are not available. To this authors knowledge, chemically synthesized Heusler NPs with a MT were not produced yet. Another production method, which was utilized in the last years, is ball milling bulk material into powders of fine NPs. The harsh preparation conditions of this method induce large elastic stress in the material and the milling balls or chamber walls can introduce chemical impurities. It was shown that by this method NPs around 10 nm with martensitic transformation could be obtained after a subsequent annealing step [115].

Another method to produce small amounts of NPs for research purposes is by employing modern lithography methods on thin films. Unlike ball milling, the gentler approach of this method allows the production of sensitive materials while retaining the crystallographic properties of the thin film, which can be determined prior to the lithography steps. Although spherical NPs cannot be produced almost any other arbitrary shape of the NPs, such as cylinders, cubes or flat stars, can be manufactured with very small size distributions. The e-beam lithography process used in this chapter is illustrated in Figure 9.1 a)-e).

To begin with, a Heusler thin film sample is spin coated with a positive

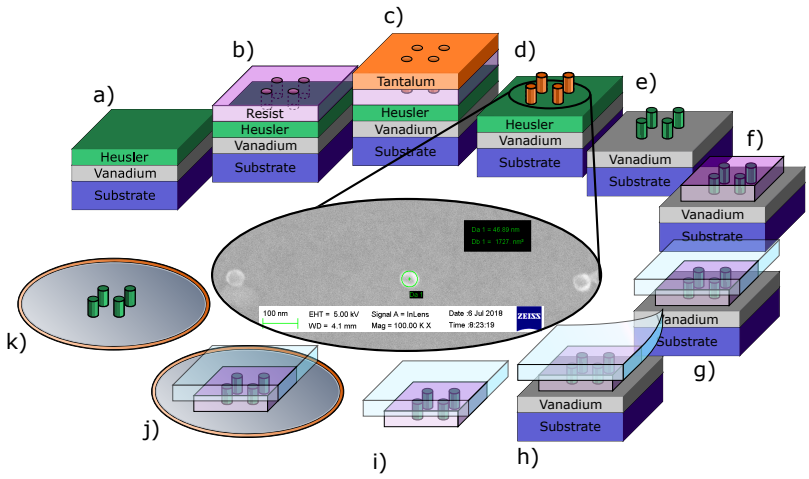

Figure 9.1: Schematic illustration of the fabrication and transfer of nanoparticles by e-beam lithography. a) Heusler alloy thin film is deposited on a V sacrificial layer. b) A PMMA positive e-beam resist is spin coated on the sample and irradiated by an electron beam. c) After developing a thin metallic layer is deposited on the sample. d) Solid masks remain after the lift-off process. e) Ar^+-ion beam milling removes the majority of the Heusler thin film except the regions covered by the mask. f) A PMMA film is spin coated on the sample and 1 mm wide stripes are scratched of the edges to expose the V sacrificial layer. g) A thick PDMS sheet is placed on the PMMA film as a support. h) The nanoparticles are released by adding a few drops of Chrome Etch solution and the PDMS support peeled off from the substrate. i) The support and the nanoparticles are brought in contact with a TEM grid or another substrate j) and dried. k) Finally the PDMS support is removed and the PMMA film is dissolved in warm NMP-remover, followed by subsequent rinsing in ethanol.

e-beam resist layer. After exposure and development small holes in the resist are obtained, which are filled by deposition of a Ta hard mask layer. The final mask is created by stripping the resist layer. Finally the NPs are obtained in a Ar^+-beam milling process under normal incidence until the Heusler layer is etched away. Only the areas covered by the mask are unaffected by the ion beam irradiation. The thickness of the Ta hard mask should be chosen such that it is removed at the same time as the Heusler layer.

Test samples, consisting of a 50 nm Ni-Co-Mn-Al layer and a 30 nm V seed layer ontop of an MgO-substrate were produced to find optimal parameters for the lithography process. Two samples were coated with a single layer and a double layer of Allresist AR-P 617.03 e-beam resist. The first sample was coated at 6000 rpm for 60 s followed by 20 min softbake at 210 °C on a hot-plate and the second sample was coated with the parameters, 6000 rpm for 60 s 20 min softbake at 210 °C for the first layer and 6000 rpm for 60 s 20 min softbake at 150 °C for the second layer. Exposure of the samples were performed in a CARL ZEISS LEO 1530 scanning electron microscope (SEM) equipped with an Raith Elphy 5.0 lithography system at 20 kV. For efficient exposure of nanoparticle arrays rectangles are drawn in the center of each writefield with the width and height $w_{\mathrm{WF}} - d_0$, where w_{WF} is the size of the writefield and d_0 the particle spacing in the pattern generator. This avoids exposure artifacts at the borders. The particle spacing is then determined by the step size, which is set to 200 nm. The samples are then developed for 2 min and placed in for 30 s in a stopper solution. They are finally blown dry under a N_2-flow and placed for 1 min at 100 °C to remove any solvents. A 50 nm Ta film is deposited afterwards and the resist is removed in a 15 min NMP ultrasonic bath followed by 10 min cleaning in ethanol and blow dry under a N_2-stream. Due to the large difference in density between the Ta and the other layers of the sample a large contrast difference can be seen in SEM images. Thus the particle statistics are determined beforehand of the ion beam milling process, which is controlled by secondary ion mass spectroscopy.

The determined particle radii and their yields in dependence of their dose for the single layer and double layer are shown in Figure 9.2 a) and b) respectively. For the size determination, SEM images of 5 µm x 5 µm were analyzed, while for the yield particles were counted in a 25 µm x 25 µm to achieve proper statistics. For both samples rather large particles with radii ranging from 55 nm to 100 nm were obtained. The particle size can be fitted quite well with a linear function, which is shown as a red line. Critical is the measured particle yields. For the smaller particles only yields between 50 % to 75 % were obtained, which significantly drops down to 5 % for larger radii. It is most likely that due to the small spacing between the particles and the thickness of the Ta mask, areas on top of the e-beam resist and in

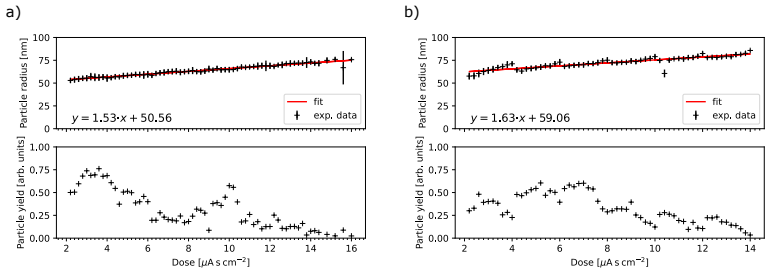

Figure 9.2: Measured particle radii (upper graph) and particle yield (bottom graph) in dependence of the dose for a) single layer of PMMA resist and b) double layer of PMMA resist.

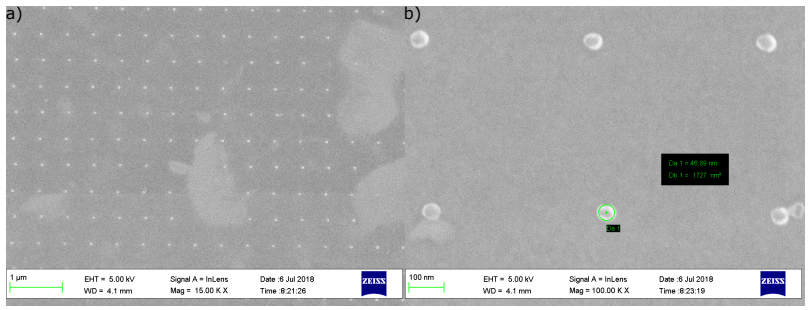

Figure 9.3: SEM image of a dose test sample with a single layer of PMMA resist, 30 nm Ta hard mask and 500 nm step size at a dose of 0.4 μA s cm^{-2}.

the holes stay in contact and are therefore dragged away in the removal step of the resist.

Smaller particles with almost 90 % yield could be prepared by a single layer of e-beam resist, increasing the step size to 500 nm and reducing the Ta thickness down to 30 nm. The smallest particles obtained so far were particles with a diameter of 47 nm at a dose of 0.4 μA s cm^{-2} as shown in Figure 9.3. They small particle loss is most likely caused in this case by surface contaminations, which can be identified by the brighter areas.

Although, very small particles can be produced by this method, the small volume of the samples is a major challenge for most analytical methods. Taking the case of the smallest particles with a 47 nm and a 500 nm distance at perfect yield of 100 % only 0.7 % of the film volume would remain. Combined with the small magnetization of the Ni-Co-Mn-Al shape memory alloy in comparison to other ferromagnetic elements, like Fe or Co, makes it

difficult to measure the characterize the martensitic phase transition even in modern magnetometers. This is further aggravated by the fact that they are bounded to the MgO-substrate, which has a large diamagnetic background at low temperatures.

One way to mitigate this is by the use of transfer processes for nanostructures. Such processes were developed in the past to successfully transfer graphene, other nanosheets and nanowires [116–118]. An example for such a process is illustrated in Figure 9.1 f)-k). The nanoparticles are first covered by a thin layer of PMMA or PLA. A rather thick PDMS sheet is then placed on top of it for further support. The structure is then released from the substrate by selectively etching the V seed layer in a chrome etchant. This was utilized in the past to produce freestanding Ni-Co-Mn-Al and Ni-Mn-Ga thin films [97, 119]. The particles on the support structure can be then placed on an arbitrary substrate or sample holder. In a last step the support structure can be released by gently dissolving the PMMA oder PLA layer in a warm bath of appropriate solvent. The benefit of this is that the nanoparticle array can be transferred without significant loss to low background substrates for magnetometry measurements, TEM-grids or special chips for thin film flash differential scanning calorimetry measurements [120–122]. All the mentioned techniques might be suitable to characterize the phase transformation in these unique NPs. Due to their large surface to volume ratio heat transfer between the surroundings and the particle is especially fast, which is an important factor to consider in solid state refrigerator prototypes. A large variety of effects, such as e.g. superconductivity, spinpolarization or topological effects [12] are found in Heusler compound thin films and bulk samples. Thus Heusler nanoparticles in general are exciting to investigate, which can lead to novel applications in other areas as well beside magnetocaloric refrigeration.

Bibliography

[1] W. J. Buehler, J. V. Gilfrich, and R. C. Wiley. Effect of Low-Temperature Phase Changes on the Mechanical Properties of Alloys near Composition TiNi. *Journal of Applied Physics*, 34(5):1475–1477, may 1963.

[2] T Duerig, A Pelton, and D Stöckel. An overview of nitinol medical applications. *Materials Science and Engineering: A*, 273-275:149–160, dec 1999.

[3] George F. Andreasen and Terry B. Hilleman. An Evaluation of 55 Cobalt Substituted Nitinol Wire for Use in Orthodontics. *The Journal of the American Dental Association*, 82(6):1373–1375, jun 1971.

[4] D J Hartl and D C Lagoudas. Aerospace applications of shape memory alloys. *Proceedings of the Institution of Mechanical Engineers, Part G: Journal of Aerospace Engineering*, 221(4):535–552, apr 2007.

[5] Reinventing the Wheel. URL: https://www.nasa.gov/specials/wheels/, Accessed: 2021-03-27.

[6] K. Ullakko, J. K. Huang, C. Kantner, R. C. O'Handley, and V. V. Kokorin. Large magnetic-field-induced strains in Ni2MnGa single crystals. *Applied Physics Letters*, 69(13):1966–1968, sep 1996.

[7] Antoni Planes, Lluís Mañosa, and Mehmet Acet. Magnetocaloric effect and its relation to shape-memory properties in ferromagnetic Heusler alloys. *Journal of Physics: Condensed Matter*, 21(23):233201, may 2009.

[8] N. Sarawate and M. Dapino. Experimental characterization of the sensor effect in ferromagnetic shape memory Ni-Mn-Ga. *Applied Physics Letters*, 88(12):121923, mar 2006.

[9] P.K. Kumar and D.C. Lagoudas. *Shape Memory Alloys*. Springer US, 2008.

[10] A. Sozinov, A. A. Likhachev, N. Lanska, and K. Ullakko. Giant magnetic-field-induced strain in NiMnGa seven-layered martensitic phase. *Applied Physics Letters*, 80(10):1746–1748, mar 2002.

[11] P. Müllner, V. A. Chernenko, and G. Kostorz. Large cyclic magnetic-field-induced deformation in orthorhombic (14m) Ni-Mn-Ga martensite. *Journal of Applied Physics*, 95(3):1531–1536, feb 2004.

[12] Tanja Graf, Claudia Felser, and Stuart S.P. Parkin. Simple rules for the understanding of Heusler compounds. *Progress in Solid State Chemistry*, 39(1):1–50, may 2011.

[13] Y. Sutou, Y. Imano, N. Koeda, T. Omori, R. Kainuma, K. Ishida, and K. Oikawa. Magnetic and martensitic transformations of NiMnX(X=In,Sn,Sb) ferromagnetic shape memory alloys. *Applied Physics Letters*, 85(19):4358, 2004.

[14] R. Kainuma, W. Ito, R. Y. Umetsu, K. Oikawa, and K. Ishida. Magnetic field-induced reverse transformation in B2-type NiCoMnAl shape memory alloys. *Applied Physics Letters*, 93(9):091906, sep 2008.

[15] I. Titov, M. Acet, M. Farle, D. González-Alonso, L. Mañosa, A. Planes, and T. Krenke. Hysteresis effects in the inverse magnetocaloric effect in martensitic Ni-Mn-In and Ni-Mn-Sn. *Journal of Applied Physics*, 112(7):073914, oct 2012.

[16] N. Teichert, D. Kucza, O. Yildirim, E. Yuzuak, I. Dincer, A. Behler, B. Weise, L. Helmich, A. Boehnke, S. Klimova, A. Waske, Y. Elerman, and A. Hütten. Structure and giant inverse magnetocaloric effect of epitaxial Ni-Co-Mn-Al films. *Phys. Rev. B*, 91:184405, May 2015.

[17] K A GschneidnerJr, V K Pecharsky, and A O Tsokol. Recent developments in magnetocaloric materials. *Reports on Progress in Physics*, 68(6):1479–1539, may 2005.

[18] Jian Liu, Tino Gottschall, Konstantin P. Skokov, James D. Moore, and Oliver Gutfleisch. Giant magnetocaloric effect driven by structural transitions. *Nature Materials*, 11(7):620–626, may 2012.

[19] A. Saren, A. R. Smith, and K. Ullakko. Integratable magnetic shape memory micropump for high-pressure, precision microfluidic applications. *Microfluidics and Nanofluidics*, 22(4), mar 2018.

[20] Bartosz Minorowicz, Giuseppe Leonetti, Frederik Stefanski, Giulio Binetti, and David Naso. Design, modelling and control of a micro-positioning actuator based on magnetic shape memory alloys. *Smart Materials and Structures*, 25(7):075005, may 2016.

[21] I. Karaman, B. Basaran, H. E. Karaca, A. I. Karsilayan, and Y. I. Chumlyakov. Energy harvesting using martensite variant reorientation mechanism in a NiMnGa magnetic shape memory alloy. *Applied Physics Letters*, 90(17):172505, apr 2007.

[22] Mohammad Amin Askari Farsangi, Francesco Cottone, Hassan Sayyaadi, Mohammad Reza Zakerzadeh, Francesco Orfei, and Luca Gammaitoni. Energy harvesting from structural vibrations of magnetic shape memory alloys. *Applied Physics Letters*, 110(10):103905, mar 2017.

[23] B. Schleicher, R. Niemann, A. Diestel, R. Hühne, L. Schultz, and S. Fähler. Epitaxial Ni-Mn-Ga-Co thin films on PMN-PT substrates for multicaloric applications. *Journal of Applied Physics*, 118(5):053906, aug 2015.

[24] Sanjay Singh, R. Rawat, and S. R. Barman. Existence of modulated structure and negative magnetoresistance in Ga excess Ni-Mn-Ga. *Applied Physics Letters*, 99(2):021902, jul 2011.

[25] Franziska Scheibel, Tino Gottschall, Andreas Taubel, Maximilian Fries, Konstantin P. Skokov, Alexandra Terwey, Werner Keune, Katharina Ollefs, Heiko Wende, Michael Farle, Mehmet Acet, Oliver Gutfleisch, and Markus E. Gruner. Hysteresis Design of Magnetocaloric Materials-From Basic Mechanisms to Applications. *Energy Technology*, 6(8):1397–1428, aug 2018.

[26] Tino Gottschall, Dimitri Benke, Maximilian Fries, Andreas Taubel, Iliya A. Radulov, Konstantin P. Skokov, and Oliver Gutfleisch. A Matter of Size and Stress: Understanding the First-Order Transition in Materials for Solid-State Refrigeration. *Advanced Functional Materials*, 27(32):1606735, jul 2017.

[27] Niclas Teichert. *Shape memory Heusler alloys for thin film applications*. PhD thesis, Universität Bielefeld, 2016.

[28] J. M. Ball and R. D. James. Fine phase mixtures as minimizers of energy. *Archive for Rational Mechanics and Analysis*, 100(1):13–52, 1987.

[29] N.H. Andersen, B. Lebech, and H.F. Poulsen. The structural phase diagram and oxygen equilibrium partial pressure of YBa2Cu3O6+x studied by neutron powder diffraction and gas volumetry. *Physica C: Superconductivity*, 172(1-2):31–42, dec 1990.

[30] R. Tickle, R.D. James, T. Shield, M. Wuttig, and V.V. Kokorin. Ferromagnetic shape memory in the NiMnGa system. *IEEE Transactions on Magnetics*, 35(5):4301–4310, 1999.

[31] K.M. Knowles and D.A. Smith. The crystallography of the martensitic transformation in equiatomic nickel-titanium. *Acta Metallurgica*, 29(1):101–110, jan 1981.

[32] Kaushik Bhattacharya. *Microstructure of martensite : why it forms and how it gives rise to the shape-memory effect*. Oxford University Press, Oxford, 2003.

[33] Stefan Schwabe. *Charakterisierung der Umwandlung von magnetokalorischen Heusler- und Antiperowskit-Dünnschichten*. PhD thesis, Technische Universität Dresden, 2020.

[34] S Kaufmann, R Niemann, T Thersleff, U K Rößler, O Heczko, J Buschbeck, B Holzapfel, L Schultz, and S Fähler. Modulated martensite: why it forms and why it deforms easily. *New Journal of Physics*, 13(5):053029, may 2011.

[35] Robert Ingo Niemann. *Nukleation und Wachstum des adaptiven Martensits in epitaktischen Schichten der Fromgedächtnislegierung Ni-Mn-Ga*. PhD thesis, Technische Universität Dresden, 2015.

[36] Anja Waske, Biswanath Dutta, Niclas Teichert, Bruno Weise, Navid Shayanfar, Andreas Becker, Andreas Hütten, and Tilmann Hickel. Coupling Phenomena in Magnetocaloric Materials. *Energy Technology*, 6(8):1429–1447, aug 2018.

[37] R. W. Cahn. *Physical metallurgy*. North-Holland, Amsterdam New York, 1996.

[38] A. I. Potekaev, A. A. Klopotov, V. V. Kulagina, and V. E. Gyunter. Influence of structural defects on the structural-phase transformations in relatively unstable states of functional materials. *Steel in Translation*, 40(10):881–887, oct 2010.

[39] G. A. Malygin. Heterogeneous nucleation of martensite at dislocations and the martensitic-transformation kinetics in shape memory alloys. *Physics of the Solid State*, 45(2):345–351, feb 2003.

[40] G. A. Malygin. Heterogeneous nucleation of martensite on precipitates and the martensitic-transformation kinetics in shape memory alloys. *Physics of the Solid State*, 45(8):1566–1571, aug 2003.

[41] Anett Diestel, Paul Chekhonin, Robert Niemann, Werner Skrotzki, Kornelius Nielsch, and Sebastian Fähler. Reducing Thermal Hysteresis in Epitaxial Ni-Mn-Ga-Co Films by Transformation Cycling. *physica status solidi (b)*, 255(2):1700330, nov 2017.

[42] Anett Diestel, Robert Niemann, Benjamin Schleicher, Kornelius Nielsch, and Sebastian Fähler. Reducing Hysteresis Losses by Heating Minor Loops in Magnetocaloric Ni-Mn-Ga-Co Films. *Energy Technology*, 6(8):1463–1469, jun 2018.

[43] Gennadii A Malygin. Diffuse martensitic transitions and the plasticity of crystals with a shape memory effect. *Physics-Uspekhi*, 44(2):173–197, feb 2001.

[44] R. J. D. Tilley. *Crystals and crystal structures*. John Wiley & Sons, Chichester, England Hoboken, NJ, 2006.

[45] Biswanath Dutta, Fritz Körmann, Tilmann Hickel, and Jörg Neugebauer. Impact of Co and Fe Doping on the Martensitic Transformation and the Magnetic Properties in Ni-Mn-Based Heusler Alloys. *physica status solidi (b)*, 255(2):1700455, nov 2017.

[46] Ryosuke Kainuma, Fumihiko Gejima, Yuji Sutou, Ikuo Ohnuma, and Kiyohito Ishida. Ordering, Martensitic and Ferromagnetic Transformations in Ni–Al–Mn Heusler Shape Memory Alloys. *Materials Transactions, JIM*, 41(8):943–949, 2000.

[47] A. Okubo, X. Xu, R. Y. Umetsu, T. Kanomata, K. Ishida, and R. Kainuma. Magnetic properties of Co50-xNixMn25Al25 alloys with B2 structure. *Journal of Applied Physics*, 109(7):07B114, apr 2011.

[48] Xiao Xu, Wataru Ito, Masashi Tokunaga, Takumi Kihara, Kengo Oka, Rie Umetsu, Takeshi Kanomata, and Ryosuke Kainuma. The Thermal Transformation Arrest Phenomenon in NiCoMnAl Heusler Alloys. *Metals*, 3(3):298–311, aug 2013.

[49] Xiao Xu, Wataru Ito, Takeshi Kanomata, and Ryosuke Kainuma. Entropy Change during Martensitic Transformation in Ni50-xCoxMn50-yAly Metamagnetic Shape Memory Alloys. *Entropy*, 16(3):1808–1818, mar 2014.

[50] Xiao Xu, Wataru Ito, Masashi Tokunaga, Rie Y. Umetsu, Ryosuke Kainuma, and Kiyohito Ishida. Kinetic Arrest of Martensitic Transformation in NiCoMnAl Metamagnetic Shape Memory Alloy. *MATERIALS TRANSACTIONS*, 51(7):1357–1360, 2010.

[51] Lothar Spieß, Gerd Teichert, Robert Schwarzer, Herfried Behnken, and Christoph Genzel. *Moderne Röntgenbeugung*. Springer Fachmedien Wiesbaden, 2019.

[52] Kiyotaka Wasa. *Handbook of Sputtering Technology*. Elsevier, 2012.

[53] D. L. Smith. *Thin-Film Deposition: Principles and Practice*. McGraw-Hill, 1st edition, 1995.

[54] D. P. Oxley, R. S. Tebble, and K. C. Williams. Heusler Alloys. *Journal of Applied Physics*, 34(4):1362–1364, apr 1963.

[55] E. Simon, J. Gy. Vida, S. Khmelevskyi, and L. Szunyogh. Magnetism of ordered and disordered Ni_2MnAl full Heusler compounds. *Physical Review B*, 92(5), aug 2015.

[56] I. Galanakis and E. Şaşıoğlu. Structural-induced antiferromagnetism in Mn-based full Heusler alloys: The case of Ni_2MnAl. *Applied Physics Letters*, 98(10):102514, mar 2011.

[57] F. Gejima, Y. Sutou, R. Kainuma, and K. Ishida. Magnetic transformation of Ni_2AlMn Heusler-type shape memory alloys. *Metallurgical and Materials Transactions A*, 30(10):2721–2723, oct 1999.

[58] K R A Ziebeck and P J Webster. Helical magnetic order in Ni_2MnAl. *Journal of Physics F: Metal Physics*, 5(9):1756–1766, sep 1975.

[59] Mehmet Acet, Eyup Duman, Eberhard F. Wassermann, Lluis Mañosa, and Antoni Planes. Coexisting ferro- and antiferromagnetism in Ni_2MnAl Heusler alloys. *Journal of Applied Physics*, 92(7):3867–3871, oct 2002.

[60] S Macke and E Goering. Magnetic reflectometry of heterostructures. *Journal of Physics: Condensed Matter*, 26(36):363201, aug 2014.

[61] C. Klewe, T. Kuschel, J.-M. Schmalhorst, F. Bertram, O. Kuschel, J. Wollschläger, J. Strempfer, M. Meinert, and G. Reiss. Static magnetic proximity effect in $Pt/Ni_{1-x}Fe_x$ bilayers investigated by x-ray resonant magnetic reflectivity. *Physical Review B*, 93(21), jun 2016.

[62] Sebastian Macke, Abdullah Radi, Jorge E. Hamann-Borrero, Adriano Verna, Martin Bluschke, Sebastian Brück, Eberhard Goering, Ronny Sutarto, Feizhou He, Georg Cristiani, Meng Wu, Eva Benckiser, Hanns-Ulrich Habermeier, Gennady Logvenov, Nicolas Gauquelin, Gianluigi A. Botton, Adam P. Kajdos, Susanne Stemmer, Georg A. Sawatzky, Maurits W. Haverkort, Bernhard Keimer, and Vladimir Hinkov. Element Specific Monolayer Depth Profiling. *Advanced Materials*, 26:6554–6559, 2014.

[63] L. G. Parratt. Surface Studies of Solids by Total Reflection of X-Rays. *Physical Review*, 95(2):359–369, jul 1954.

[64] J. Zak, E.R. Moog, C. Liu, and S.D. Bader. Universal approach to magneto-optics. *Journal of Magnetism and Magnetic Materials*, 89(1-2):107–123, sep 1990.

[65] B.L. Henke, E.M. Gullikson, and J.C. Davis. X-Ray Interactions: Photoabsorption, Scattering, Transmission, and Reflection at E = 50-30,000 eV, Z = 1-92. *Atomic Data and Nuclear Data Tables*, 54(2):181–342, jul 1993.

[66] Jan Krieft, Dominik Graulich, Anastasiia Moskaltsova, Laurence Bouchenoire, Sonia Francoual, and Timo Kuschel. Advanced data analysis procedure for hard x-ray resonant magnetic reflectivity discussed for Pt thin film samples of various complexity. *Journal of Physics D: Applied Physics*, 53(375004), may 2020.

[67] Yukio Suezaki and Hazime Mori. Dynamic critical phenomena in magnetic systems. II. *Progress of Theoretical Physics*, 41(5):1177–1189, may 1969.

[68] R. Y. Umetsu, M. Miyakawa, K. Fukamichi, and A. Sakuma. Pseudogap in the density of states and the highest néel temperature of the $L1_0$-type MnIr alloy system. *Physical Review B*, 69(10), mar 2004.

[69] Rie Y. Umetsu, Kazuaki Fukamichi, and Akimasa Sakuma. Electrical and Magnetic Properties, and Electronic Structures of Pseudo-Gap-Type Antiferromagnetic $L1_0$-Type MnPt Alloys. *MATERIALS TRANSACTIONS*, 47(1):2–10, 2006.

[70] Tomoki Tsuchiya, Takahide Kubota, Tomoko Sugiyama, Teodor Huminiuc, Atsufumi Hirohata, and Koki Takanashi. Exchange bias effects in heusler alloy ni2mnal/fe bilayers. *Journal of Physics D: Applied Physics*, 49(23):235001, may 2016.

[71] C. Paduani, A. Migliavacca, M.L. Sebben, J.D. Ardisson, M.I. Yoshida, S. Soriano, and M. Kalisz. Ferromagnetism and antiferromagnetism in $Ni_{2+x+y}Mn_{1-x}Al_{1-y}$ alloys. *Solid State Communications*, 141(3):145–149, jan 2007.

[72] Bruce Billings. *American Institute of Physics handbook*. McGraw-Hill, New York, 1972.

[73] Lawrence E. Davis. *Handbook of Auger Electron Spectroscopy: A Reference Book of Standard Data for Identification and Interpretation of Auger Electron Spectroscopy Data*. Physical Electronics, 1996.

[74] S. Andrieu, E. Foy, H. Fischer, M. Alnot, F. Chevrier, G. Krill, and M. Piecuch. Effect of O contamination on magnetic properties of ultrathin Mn films grown on (001) Fe. *Physical Review B*, 58(13):8210–8213, oct 1998.

[75] H J Lee, G Kim, D H Kim, J-S Kang, C L Zhang, S-W Cheong, J H Shim, Soonchil Lee, Hangil Lee, J-Y Kim, B H Kim, and B I Min. Valence states and occupation sites in $(Fe,Mn)_3O_4$ spinel oxides investigated by soft x-ray absorption spectroscopy and magnetic circular dichroism. *Journal of Physics: Condensed Matter*, 20(29):295203, jun 2008.

[76] J. Fujii, F. Borgatti, G. Panaccione, M. Hochstrasser, F. Maccherozzi, G. Rossi, and G. van der Laan. Evidence for in-plane spin-flop orientation at the MnPt/Fe(100) interface revealed by x-ray magnetic linear dichroism. *Physical Review B*, 73(21), jun 2006.

[77] W. L. O'Brien and B. P. Tonner. Surface-enhanced magnetic moment and ferromagnetic ordering of Mn ultrathin films on fcc Co(001). *Physical Review B*, 50(5):2963–2969, aug 1994.

[78] B. T. Thole, R. D. Cowan, G. A. Sawatzky, J. Fink, and J. C. Fuggle. New probe for the ground-state electronic structure of narrow-band and impurity systems. *Physical Review B*, 31(10):6856–6858, may 1985.

[79] T. Büsgen, J. Feydt, R. Hassdorf, S. Thienhaus, M. Moske, M. Boese, A. Zayak, and P. Entel. Ab initio calculations of structure and lattice dynamics in Ni-Mn-Al shape memory alloys. *Physical Review B*, 70(1), jul 2004.

[80] T. Kuschel, C. Klewe, J.-M. Schmalhorst, F. Bertram, O. Kuschel, T. Schemme, J. Wollschläger, S. Francoual, J. Strempfer, A. Gupta,

M. Meinert, G. Götz, D. Meier, and G. Reiss. Static Magnetic Proximity Effect in Pt/$NiFe_2O_4$ and Pt/Fe Bilayers Investigated by X-Ray Resonant Magnetic Reflectivity. *Physical Review Letters*, 115(9), aug 2015.

[81] Timo Kuschel, Christoph Klewe, Panagiota Bougiatioti, Olga Kuschel, Joachim Wollschlager, Laurence Bouchenoire, Simon D. Brown, Jan-Michael Schmalhorst, Daniel Meier, and Gunter Reiss. Static Magnetic Proximity Effect in Pt Layers on Sputter-Deposited $NiFe_2O_4$ and on Fe of Various Thicknesses Investigated by XRMR. *IEEE Transactions on Magnetics*, 52(7):1–4, jul 2016.

[82] Anastasiia Moskaltsova, Jan Krieft, Dominik Graulich, Tristan Matalla-Wagner, and Timo Kuschel. Impact of the magnetic proximity effect in Pt on the total magnetic moment of Pt/Co/Ta trilayers studied by x-ray resonant magnetic reflectivity. *AIP Advances*, 10(1):015154, 2020.

[83] Sebastian Brück, Sebastian Macke, Eberhard Goering, Xiaosong Ji, Qingfeng Zhan, and Kannan M. Krishnan. Coupling of Fe and uncompensated Mn moments in exchange-biased Fe/MnPd. *Physical Review B*, 81(13), apr 2010.

[84] A. Hoffmann, J. W. Seo, M. R. Fitzsimmons, H. Siegwart, J. Fompeyrine, J.-P. Locquet, J. A. Dura, and C. F. Majkrzak. Induced magnetic moments at a ferromagnet-antiferromagnet interface. *Physical Review B*, 66(22), dec 2002.

[85] P. Kappenberger, S. Martin, Y. Pellmont, H. J. Hug, J. B. Kortright, O. Hellwig, and Eric E. Fullerton. Direct imaging and determination of the uncompensated spin density in exchange-biased CoO/(CoPt) multilayers. *Physical Review Letters*, 91(26), dec 2003.

[86] F. Offi, W. Kuch, L. I. Chelaru, K. Fukumoto, M. Kotsugi, and J. Kirschner. Induced Fe and Mn magnetic moments in Co-FeMn bilayers on Cu(001). *Physical Review B*, 67(9), mar 2003.

[87] S. Roy, M. R. Fitzsimmons, S. Park, M. Dorn, O. Petracic, Igor V. Roshchin, Zhi-Pan Li, X. Batlle, R. Morales, A. Misra, X. Zhang, K. Chesnel, J. B. Kortright, S. K. Sinha, and Ivan K. Schuller. Depth profile of uncompensated spins in an exchange bias system. *Physical Review Letters*, 95(4), jul 2005.

[88] G. Jakob, T. Eichhorn, M. Kallmayer, and H. J. Elmers. Correlation of electronic structure and martensitic transition in epitaxial Ni_2MnGa films. *Physical Review B*, 76(17), nov 2007.

[89] K. R. Priolkar, P. A. Bhobe, D. N. Lobo, S. W. D'Souza, S. R. Barman, Aparna Chakrabarti, and S. Emura. Antiferromagnetic exchange interactions in the $Ni_2Mn_{1.4}In_{0.6}$ ferromagnetic Heusler alloy. *Physical Review B*, 87(14), apr 2013.

[90] Marius Wodniok, Niclas Teichert, Lars Helmich, and Andreas Hütten. How to enable bulk-like martensitic transformation in epitaxial films. *AIP Advances*, 7(5):056428, may 2017.

[91] R. Niemann, S. Hahn, A. Diestel, A. Backen, L. Schultz, K. Nielsch, M. F.-X. Wagner, and S. Fähler. Reducing the nucleation barrier in magnetocaloric Heusler alloys by nanoindentation. *APL Materials*, 4(6):064101, jun 2016.

[92] D. Allan Bromley, editor. *Treatise on Heavy-Ion Science*. Springer US, 2012.

[93] S. Cervera, M Trassinelli, M Marangolo, C Carrétéro, V Garcia, S Hidki, E Jacquet, E Lamour, A Lévy, S Macé, C Prigent, J Rozet, S Steydli, and D Vernhet. Modulating the phase transition temperature of giant magnetocaloric thin films by ion irradiation.

[94] Benedikt Eggert, Alexander Schmeink, Johanna Lill, Maciej Oskar Liedke, Ulrich Kentsch, Maik Butterling, Andreas Wagner, Sakura Pascarelli, Kay Potzger, Jürgen Lindner, Thomas Thomson, Jürgen Fassbender, Katharina Ollefs, Werner Keune, Rantej Bali, and Heiko Wende. Magnetic response of FeRh to static and dynamic disorder. *RSC Advances*, 10(24):14386–14395, 2020.

[95] S. Rios, D. Bufford, I. Karaman, H. Wang, and X. Zhang. Magnetic field induced phase transformation in polycrystalline NiCoMnAl thin films. *Applied Physics Letters*, 103(13):132404, sep 2013.

[96] B. Weise, B. Dutta, N. Teichert, A. Hütten, T. Hickel, and A. Waske. Role of disorder when upscaling magnetocaloric Ni-Co-Mn-Al Heusler alloys from thin films to ribbons. *Scientific Reports*, 8(1), jun 2018.

[97] Lars Helmich, Niclas Teichert, Walid Hetaba, Anna Behler, Anja Waske, Svetlana Klimova, and Andreas Huetten. Vanadium sacrificial layers as a novel approach for the fabrication of freestanding Heusler Shape Memory Alloys.

[98] P. Klaer, E. Arbelo Jorge, M. Jourdan, W. H. Wang, H. Sukegawa, K. Inomata, and H. J. Elmers. Temperature dependence of x-ray

absorption spectra in the ferromagnetic Heusler alloys Mn2VAl and Co2FeAl. *Physical Review B*, 82(2), jul 2010.

[99] Tomoki Tsuchiya, Ryota Kobayashi, Takahide Kubota, Kotaro Saito, Kanta Ono, Takashi Ohhara, Akiko Nakao, and Koki Takanashi. Mn2VAl Heusler alloy thin films: appearance of antiferromagnetism and exchange bias in a layered structure with Fe. *Journal of Physics D: Applied Physics*, 51(6):065001, jan 2018.

[100] Jonathan Ehrler, Biplab Sanyal, Jörg Grenzer, Shengqiang Zhou, Roman Böttger, Benedikt Eggert, Heiko Wende, Jürgen Lindner, Jürgen Fassbender, Christoph Leyens, Kay Potzger, and Rantej Bali. Magneto-structural correlations in a systematically disordered B2 lattice. *New Journal of Physics*, 22(7):073004, jul 2020.

[101] M. O. Liedke, W. Anwand, R. Bali, S. Cornelius, M. Butterling, T. T. Trinh, A. Wagner, S. Salamon, D. Walecki, A. Smekhova, H. Wende, and K. Potzger. Open volume defects and magnetic phase transition in Fe60Al40 transition metal aluminide. *Journal of Applied Physics*, 117(16):163908, apr 2015.

[102] Jonathan Ehrler, Maciej Oskar Liedke, Jakub Čížek, Richard Boucher, Maik Butterling, Shengqiang Zhou, Roman Böttger, Eric Hirschmann, Thu Trang Trinh, Andreas Wagner, Jürgen Lindner, Jürgen Fassbender, Christoph Leyens, Kay Potzger, and Rantej Bali. The role of open-volume defects in the annihilation of antisites in a B2-ordered alloy. *Acta Materialia*, 176:167–176, sep 2019.

[103] B Schleicher, D Klar, K Ollefs, A Diestel, D Walecki, E Weschke, L Schultz, K Nielsch, S Fähler, H Wende, and M E Gruner. Electronic structure and magnetism of epitaxial Ni-Mn-Ga(-Co) thin films with partial disorder: a view across the phase transition. *Journal of Physics D: Applied Physics*, 50(46):465005, oct 2017.

[104] C. Seguí and E. Cesari. Effect of ageing on the structural and magnetic transformations and the related entropy change in a Ni-Co-Mn-Ga ferromagnetic shape memory alloy. *Intermetallics*, 19(5):721–725, may 2011.

[105] V Sánchez-Alarcos, J I Pérez-Landazábal, V Recarte, J A Rodríguez-Velamazán, and V A Chernenko. Effect of atomic order on the martensitic and magnetic transformations in Ni-Mn-Ga ferromagnetic shape memory alloys. *Journal of Physics: Condensed Matter*, 22(16):166001, apr 2010.

[106] M.F. Qian, X.X. Zhang, L.S. Wei, L. Geng, and H.X. Peng. Effect of chemical ordering annealing on martensitic transformation and superelasticity in polycrystalline Ni-Mn-Ga microwires. *Journal of Alloys and Compounds*, 645:335–343, oct 2015.

[107] Andreas Taubel, Tino Gottschall, Maximilian Fries, Stefan Riegg, Christopher Soon, Konstantin P. Skokov, and Oliver Gutfleisch. A Comparative Study on the Magnetocaloric Properties of Ni-Mn-X(-Co) Heusler Alloys. *physica status solidi (b)*, 255(2):1700331, nov 2017.

[108] P. Devi, C. Salazar Mejía, L. Caron, Sanjay Singh, M. Nicklas, and C. Felser. Effect of chemical and hydrostatic pressure on the coupled magnetostructural transition of Ni-Mn-In Heusler alloys. *Physical Review Materials*, 3(12), dec 2019.

[109] S. Kaufmann, U. K. Rößler, O. Heczko, M. Wuttig, J. Buschbeck, L. Schultz, and S. Fähler. Adaptive Modulations of Martensites. *Physical Review Letters*, 104(14), apr 2010.

[110] Daniela Ramermann. *Magnetic investigations in the TEM: EMCD and DPC measurements on Heusler alloys towards interfacial properties and magnetic characterization of thin film systems.* PhD thesis, Universität Bielefeld, 2021.

[111] C. Barry Carter David B. Williams. *Transmission Electron Microscopy*. Springer-Verlag GmbH, 2009.

[112] R. F. Egerton. *Electron Energy-Loss Spectroscopy in the Electron Microscope*. Springer-Verlag GmbH, 2011.

[113] Sebastian Fähler. Interfaces in Multiferroic Magnetic Shape Memory Alloys. Habilitationsschrift, Technische Universität Dresden, 2013.

[114] Changhai Wang, Judith Meyer, Niclas Teichert, Alexander Auge, Elisabeth Rausch, Benjamin Balke, Andreas Hütten, Gerhard H. Fecher, and Claudia Felser. Heusler nanoparticles for spintronics and ferromagnetic shape memory alloys. *Journal of Vacuum Science & Technology B, Nanotechnology and Microelectronics: Materials, Processing, Measurement, and Phenomena*, 32(2):020802, mar 2014.

[115] D.M. Liu, Z.H. Nie, Y.D. Wang, Y.D. Liu, G. Wang, Y. Ren, and L. Zuo. New Sequences of Phase Transition in Ni-Mn-Ga Ferromagnetic Shape Memory Nanoparticles. *Metallurgical and Materials Transactions A*, 39(2):466–469, dec 2007.

[116] L. G. P. Martins, Y. Song, T. Zeng, M. S. Dresselhaus, J. Kong, and P. T. Araujo. Direct transfer of graphene onto flexible substrates. *Proceedings of the National Academy of Sciences*, 110(44):17762–17767, oct 2013.

[117] Hai Li, Jumiati Wu, Xiao Huang, Zongyou Yin, Juqing Liu, and Hua Zhang. A Universal, Rapid Method for Clean Transfer of Nanostructures onto Various Substrates. *ACS Nano*, 8(7):6563–6570, jun 2014.

[118] P. Sveshtarov J. Leclercq. The Transfer of Graphene: A Review. *Bulg. J. Phys.*, 43:121–147, 2016.

[119] Niclas Teichert. *Shape memory Heusler alloys for thin film applications*. PhD thesis, Universität Bielefeld, 2016.

[120] Mikhail Yu. Efremov, Eric A. Olson, Ming Zhang, François Schiettekatte, Zishu Zhang, and Leslie H. Allen. Ultrasensitive, fast, thin-film differential scanning calorimeter. *Review of Scientific Instruments*, 75(1):179–191, jan 2004.

[121] M.Yu. Efremov, E.A. Olson, M. Zhang, S.L. Lai, F. Schiettekatte, Z.S. Zhang, and L.H. Allen. Thin-film differential scanning nanocalorimetry: heat capacity analysis. *Thermochimica Acta*, 412(1-2):13–23, mar 2004.

[122] A.A. Minakov, S.A. Adamovsky, and C. Schick. Non-adiabatic thin-film (chip) nanocalorimetry. *Thermochimica Acta*, 432(2):177–185, jul 2005.

List of Figures

List of Tables

Publications

[1] Andreas Becker, Daniela Ramermann, Inga Ennen, Björn Büker, Tristan Matalla-Wagner, Martin Gottschalk, and Andreas Hütten. The Influence of Martensitic Intercalations in Magnetic Shape Memory NiCoMnAl Multilayered Films. *Entropy*, 23(4):462, apr 2021.

[2] Daniela Ramermann, Andreas Becker, Björn Büker, Trevor Almeida, Robert Webster, Stephen McVitie, Inga Ennen, and Andreas Hütten. Imaging Microstructural Impact on Magnetic Behavior. *Imaging & Microscopy*, 23:30–33, mar 2021.

[3] Denis Dyck, Andreas Becker, Jungwoo Koo, Tristan Matalla-Wagner, Jan Krieft, and Günter Reiss. Anomalous Hall Effect and Magnetoresistance in Sputter-Deposited Magnetic Weyl Semimetal Co2TiGe Thin Films. *physica status solidi (b)*, 258(1):2000067, jul 2020.

[4] Thomas Vordemvenne, Dirk Wähnert, Julian Koettnitz, Madlen Merten, Nadine Fokin, Andreas Becker, Björn Büker, Asaria Vogel, Daniel Kronenberg, Richard Stange, Günther Wittenberg, Johannes FW Greiner, Andreas Hütten, Christian Kaltschmidt, and Barbara Kaltschmidt. Bone Regeneration: A Novel Osteoinductive Function of Spongostan by the Interplay between Its Nano- and Microtopography. *Cells*, 9(3):654, mar 2020.

[5] Daniel Kappe, Laila Bondzio, Joris Swager, Andreas Becker, Björn Büker, Inga Ennen, Christian Schröder, and Andreas Hütten. Reviewing Magnetic Particle Preparation: Exploring the Viability in Biosensing. *Sensors*, 20(16):4596, aug 2020.

[6] Anja Waske, Biswanath Dutta, Niclas Teichert, Bruno Weise, Navid Shayanfar, Andreas Becker, Andreas Hütten, and Tilmann Hickel. Coupling Phenomena in Magnetocaloric Materials. *Energy Technology*, 6(8):1429–1447, aug 2018.

[7] Robin Klett, Joachim Schönle, Andreas Becker, Denis Dyck, Kiril Borisov, Karsten Rott, Daniela Ramermann, Björn Büker, Jan Haskenhoff, Jan Krieft, Torsten Hübner, Oliver Reimer, Chandra Shekhar, Jan-Michael Schmalhorst, Andreas Hütten, Claudia Felser, Wolfgang Wernsdorfer, and Günter Reiss. Proximity-Induced Superconductivity and Quantum Interference in Topological Crystalline Insulator SnTe Thin-Film Devices. *Nano Letters*, 18(2):1264–1268, jan 2018.

Conferences

- ”Magnetic and magnetoelastic properties of NiCoMnAl shape memory Heusler alloys”, DPG-Frühjahrstagung, Regensburg, 2016
- ”NiCoMnAl-Shape Memory Alloys in Hybrid Spintronic Devices” Spin Mechanics 4, Lake Louise (Kanada), 2017
- ”Shape Memory Alloys in Hybrid Spintronic Devices ”, DPG-Frühjahrstagung, Dresden, 2017
- ”Influence of martensite intercalations on the thermal hysteresis in NiMn-based magnetic shape memory alloys”, DPG-Frühjahrstagung, Berlin, 2018
- ”3D check board pattern formation of martensite/austenite domains in NiCoMnAl shape memory alloys”, Thermag VIII, Darmstadt, 2018
- ”3D check board pattern formation of martensite/austenite domains in NiCoMnAl shape memory alloys”, DPG-Frühjahrstagung, Regensburg, 2019
- ”3D check board pattern formation of martensite/austenite domains in NiCoMnAl shape memory alloys”, MMM Conference Las Vegas (Nevada, USA), 2019